Mass Transfer Stability, Lagrangian Ejection, and Gas Fall-back in Common Envelope Binaries

By

Jack Nibbs

A thesis submitted to Macquarie University

for the degree of Master of Research

Department of Mathematical & Physical Sciences

February 2023

MACQUARIE
University
SYDNEY·AUSTRALIA

Examiner's Copy

Typeset in LaTeX 2_ε.

Except where acknowledged in the customary manner, the material presented in this thesis is, to the best of my knowledge, original and has not been submitted in whole or part for a degree in any university.

Jack Nibbs

Acknowledgements

I would like to begin by thanking my family. They have always been extremely supportive of absolutely everything I have ever done, and have consistently provided me the privilege to pursue my passions without fear or hesitation. You taught me all the most important things I know (except math): to be open minded, to challenge myself, to think critically, and most importantly, to find joy in absolutely everything (even math). I owe everything I was, everything I am, and everything I will become to you. For that, I am eternally grateful. Never will I take such love for granted, and I hope you all know how much I love you too (to infinity and beyond).

I would next like to thank my supervisor, Professor Orsola DeMarco. I cannot express how much of a privilege it has been getting to undertake this project with you. I chose you as my supervisor because beyond just the field that you work in, your enthusiasm and charisma are infectious, your knowledge and insight beyond reproach, and I knew, I absolutely knew, you would help bring out the best in what I have to offer, and to make me feel valued and useful. It has been a pleasure to work in the presence of your optimism, and I hope, come what may, to continue this friendship well into the future.

Finally I would like to take this opportunity to give thanks to the people that helped me make this thesis a reality. To Gabby, Jimmy, and Elizabeth, it was a pleasure getting to hang out with you, talk with you, and vent with you. It could've been the only reprieve from work I had, and it would've been enough with just you three. To Miguel, Lachlan, Amy, and the rest of the PhD students in the department, thank you for putting up with my obnoxious jokes and loud mouth. Your smiles have (at times) been broad and your advice sage. To my dear friends Carmen, Josh, and Joel, thank you for letting me forget all about the world that exists outside late night karaoke to old Misfits songs. I cherish every second I get to spend with

you all. To Harry, Mel, Locky, and Mister Thunder, from watching absolutely awful movies, to games nights, to all the music and experiences I've gotten to share with you, it has brought me a literally infinite amount of joy (trust me, I do math). Thank you so much. To the team, and everyone else associated with the Winston Hills Bears, you're all champions to me and it has been an honour playing another season with you all, lets hope my knees last long enough for another. To the family at Shred Fitness in Blacktown, you let me scream and cheer until my voice dies, and cheer and scream right back at me, you are enthusiasm incarnate, thank you. Last but certainly not least, to my dear Sally, my sunshine, I will say only this: I love you most.

Abstract

In this thesis we carry out a number of common envelope (CE) binary interaction simulations with the 3D, smooth particle hydrodynamics code PHANTOM, to study the dependence of the early, pre-CE mass transfer phase on the mass ratio between the two stars in a binary. We found that for larger mass ratios ($q \equiv \frac{M_2}{M_1}$) the pre-CE Roche lobe overflow phase is more stable, and the mass transfer is longer lasting to the point that, should the mass ratio become such that the companion is more massive than the primary, the CE in-spiral is prevented (at least in the timescales accessible by the simulations). In studying this pre-CE phase, we have also found that binaries with large q values eject more mass early, but unbind less of it when compared to lower q counterparts. In both cases, any material that is likely to fall-back onto the system comes from the material which is ejected later on during the CE, and not beforehand, as much of the earlier ejecta's behaviour is characteristic of homologous expansion, reaching velocities that render the material unbound by the CE's conclusion. This also shows us that the pre-CE mass loss has a very small contribution, if any at all, to shaping the final CE ejection. We have also analysed the role of this gas fall-back on the properties of the post-CE objects, resolving that the final tightening of the orbit is unlikely to be possible solely at the hand of envelope return, given the amount of mass expected.

Contents

1

Introduction

1.1 Binary System Phenomena and the Common Envelope Interaction

Multiple star systems are a common phenomenon throughout the galaxy, covering a large range of configurations in terms of mass ratio, and evolutionary phase (Duchêne & Kraus, 2013). Binary separations also vary widely with a wide spectrum of distances from below 5 $R_\odot$, to well over 100 $R_\odot$ in some cases (Iaconi et al., 2017a; Deacon & Kraus, 2020). The characteristics and morphology of these binary systems can also shift dramatically during the common envelope (CE) phase of binary stellar evolution (Ivanova et al., 2013; Paczynski, 1976). Investigating the nature of this CE interaction has been a process spanning decades, and there is still much that is unclear as to the physics of this process.

The CE phase is marked by the engulfment of a companion star into the envelope of its host. It is most commonly preceded by a period of semi-stable mass transfer between the stars due to Roche lobe overflow (RLOF). RLOF is caused by the natural growth of the host star

as it moves through the main sequence to the red giant branch (and, later to the asymptotic giant branch). The CE was originally invoked by Paczynski (1976) as a way to shrink binary orbital separations to explain the formation of cataclysmic variables, X-ray binaries, and a host of other binary classes and phenomena. This interaction has been observed in the case of the eclipsing binary system V1309 Sco by Tylenda et al. (2011), where the orbital period was observed to reduce, leading to an outburst after-which no binary could be observed. This provides some observable evidence for a CE interaction that resulted in a merger. We expect, however that some CE interactions would result in a surviving binary, forming the close evolved binaries mentioned previously.

Type Ia supernovae are a relevant example of a well documented transient phenomenon, with origins in binary stellar systems. In this case, there is at least one white dwarf in the system, that accretes mass from another star or merges with another white dwarf, to exceed the Chandrasekhar mass limit of 1.44 $M_\odot$. This results in a detonation with a universally similar (or scalable) luminosity peak, making Type Ia supernovae excellent standard candles for measuring distances (Schmidt & High-Z Sn Search Team, 1998). There are two main ways in which these objects can be generated. The single degenerate path involves a main sequence star transferring mass onto a white dwarf companion, causing a thermonuclear explosion due to a breach of the Chandrasekhar mass (Han & Podsiadlowski, 2004). Similarly, the mass of the resulting star can become too high in double degenerate progenitors that require the merging of two white dwarf stars (Webbink, 1984). In both these scenarios at least a CE interaction is needed to reduce the orbital separation and allow mass transfer or merging to take place.

The nature of any CE interaction heavily depends on the stability of the early mass transfer stage. It is important then to investigate what systems undergo a CE phase, and what becomes of the binary once said phase is either completed, or avoided. The mass ratio, q, of the binary is perhaps the most crucial parameter in understanding the behaviour of the system. Tout & Hall (1991) found analytically that for a non rotating star, approximated with a polytropic index of 1.5, stable mass transfer would take place for a value of $q \equiv M_2/M_1 \gtrsim 1.43$ (M_2 is noted as the accretor, and M_1 is the donor). It is likely that this value itself is further parameter-dependent.

It is possible that most, if not all closely orbiting, evolved binaries have undergone some type of CE phase. However, there are some evolved binaries with separations that are

small enough to necessitate a CE interactions, yet larger than many types of post-CE compact binaries, and larger than can be reproduced by typical CE simulations (e.g., Passy et al., 2012). It is difficult to determine how they would have avoided more dramatic orbital shrinkage. Phases of more stable mass transfer can grant the binary system the energy and momentum to widen their separation and cease the mass transfer without having ever undergone a full CE. The class of binaries with separations of the order of $\gtrsim 100$ $R_\odot$ often have a post-AGB primary with a main sequence companion (van Winckel et al., 2009). It was shown by Oomen et al. (2018) that at the time of interaction these binary systems had q values of order unity, indicating that the mass ratio likely has a significant impact on the rate of mass transfer, and thus also greatly impacts any CE interaction that might follow. Finally, it is crucial to note that in order for these close orbiting binaries to have survived the CE interaction, there must have been a substantial, if not total unbinding of the envelope. The presence of a significant amount of bound envelope gas by the conclusion of the CE interaction will lead to envelope fall-back and further interaction, possibly culminating in a stellar merger, as we will discuss in detail later.

1.2 Theoretical Background

We can think of the CE interaction as a reduced three body problem. There are two main bodies in the binary system to consider, but once enough mass transfer has occurred during RLOF, the impact of the gas populating the space between and around the two stars becomes non-negligible. Once the CE has begun the Roche lobe geometry no longer holds, however, up until that point, the approximation for the Roche geometry generated by Eggleton (1983) holds remarkably well. The essence of this geometry come from contours of equipotential, the lowest of which define the point of mass transfer between the stars, L_1. To properly consider this geometry we are required to look at the system from the perspective of the rotating frame, where the size and shape of the Roche lobes are then influenced primarily by the mass of the two stars, with parameters such as orbital velocity altering the nature of their tear drop shape. The approximation used here works by considering spheres generated from the effective Roche radius, r_L in 1.1, and depends only on the mass ratio, q, of the system. In recent years more attempts have been made to approximate the Roche geometry, namely by Leahy & Leahy (2015), however the approximation given by Eggleton (1983) has remained

relevant.

$$r_{\rm L} = \frac{0.49q^{2/3}}{0.6q^{2/3} + \ln(1 + q^{1/3})}. \tag{1.1}$$

There are a few ways in which stars can enter Roche lobe contact and begin the process of mass transfer. The most common is by growing due to regular stellar evolution towards and along the red giant branch, or the asymptotic giant branch. The first phase of a CE interaction is the initial mass transfer through the innermost Lagrange point, L_1, where much of the material will then be accreted by the companion or gather into a circum-companion disk. If the companion star is a low mass main sequence star, and hence fully convective, it will expand upon accretion and fill its own Roche lobe (Paczynski, 1976). Gas in the companion's Roche lobe has the potential to escape the system though the outer Lagrange point, L_2 on the side of the companion, and even through L_3 on the side of the primary. This lost mass carries angular momentum with it, thus causing the binary to compensate by shrinking the orbital separation.

Orbital decay is also possible due to the Darwin instability (Darwin, 1879), which arises due to tidal interactions between the two orbiting bodies. In many of the cases we will consider, the donor star is significantly larger, and more diffuse than its typically compact companion. We consider that the tidal bulge generated on the primary by the companion is larger than that of the primary's on the companion, such that $I_1\Omega_1 \gg I_2\Omega_2$, where I is the moment of inertia of the star, and Ω is its respective spin angular velocity. We can then write that the total angular momentum of said system is given by:

$$J = I_1\Omega_1 + \mu a^2\Omega_{\rm orb}, \tag{1.2}$$

where μ is the reduced mass of the binary, a is the orbital separation, and $\Omega_{\rm orb}$ is the spin angular velocity of the orbit. There are three scenarios that can arise from this. The first is that the orbital and stellar spins are synchronised, and the axis of this tidal bulge aligns with the stellar separation axis. In this case, the orbit remains stable, and will neither shrink nor grow. In the other two circumstances however, either the tidal bulge of the primary can lag behind the orbit of the companion ($\Omega_1 < \Omega_{\rm orb}$), or it can lead the orbit of the companion ($\Omega_1 > \Omega_{\rm orb}$). Here we will only consider the case when the spin of the primary and the tidal bulge lag the orbit of the companion. Tidal torques will transfer angular momentum from the orbit to the primary, shrinking the orbit and increasing the spin of the primary. However at

this new orbital distance, the companion's orbital velocity is larger. The system can then only obtain synchronicity and stability if the rate of spin of the primary increases to match the orbital frequency, such that $\dot{\Omega_1} > \dot{\Omega_{\rm orb}}$, otherwise the tidal bulge will lag more and decrease the orbital distance further and drive the stars to merge ($\dot{\Omega_1} < \dot{\Omega_{\rm orb}}$) (Darwin, 1879; Hut, 1980). By conservation of angular momentum of this system we have:

$$\dot{J} = I_1\dot{\Omega_1} + 2\mu a\dot{a}\Omega_{\rm orb} + \mu a^2\dot{\Omega_{\rm orb}} = 0. \tag{1.3}$$

By noticing that we can write $\dot{\Omega_{\rm orb}}/\Omega_{\rm orb} = -(3/2)(\dot{a}/a)$, we the arrive at Equation 1.4:

$$J_{\rm spin} > \frac{1}{3}J_{\rm orb}, \tag{1.4}$$

which states that the system is Darwin unstable if the angular momentum of the primary is greater than a third of the orbital angular momentum.

Chronologically the next stage of the CE interaction is the dynamic in-spiral, characterised by the rapid reduction in orbital separation. As the companion begins to in-spiral inside the host, the resulting torques result in an increase in the envelope gas' angular momentum. If the companion is massive enough, the dragging of the envelope's gas tends to establish co-rotation of gas and orbit, and a reduction in the gravitational drag forces by approximately three orders of magnitude compared to the on-set of in-spiral (Passy et al., 2012). An approximation of this gravitational drag is given by Iben & Livio (1993) in Equation 1.5:

$$F_{\rm drag} = \xi\pi R_a^2\rho(v - v_e)^3, \tag{1.5}$$

where ξ is a scaling factor depending on Mach number (Ostriker, 1999), ρ is the density of the envelope gas, $v - v_{\rm e}$ is the difference in velocity between the cores and the gas, and $\rm R_a$ is the accretion radius as defined in Equation 1.6, with $\rm c_s$ defining the local sound speed:

$$R_{\rm a} = \frac{2GM}{(v - v_{\rm e})^2 + c_{\rm s}^2}. \tag{1.6}$$

The final stage of the CE following the dynamic in-spiral phase is the self-regulated in-spiral phase, wherein much of the original system's gas has exited the orbit of the binary and formed an extended envelope. At this point the binary system's mass ratio has also moved closer to unity (Meyer & Meyer-Hofmeister, 1979). The two outcomes of this final phase of the CE depend on the nature of the extended envelope. In order for many of the close orbiting binaries we observe to exist, the envelope needs to be ejected. If the envelope is

not ejected, the orbiting stellar cores will continue transferring angular momentum into the extended envelope, eventually creating such a decay in separation that the two cores merge. This is believed to be the case for V1309 Sco (Tylenda et al., 2011). It is unclear at this point just how much initial conditions can influence the final separation distances observed.

In order to predict what may become of a system's CE phase, we introduce an energy formalism (Webbink, 1984; Iben & Livio, 1993; Ivanova et al., 2013), where we equate the difference in orbital energies between the initial and final configurations of the binary, to the energy required to unbind the envelope entirely, shown in Equation 1.7:

$$E_{\rm bind} = \Delta E_{\rm orb} \equiv E_{\rm orb,f} - E_{\rm orb,i}. \tag{1.7}$$

The binding energy of the envelope is given in Equation 1.8:

$$E_{\rm bind} = G\frac{M_1 M_{1,\rm env}}{\lambda R_1}, \tag{1.8}$$

where λ is a characteristic of the internal structure of the host star, M_1 is core mass of the star, $M_{1,\rm env}$ is the envelope mass, and R_1 is the star's radius. We also have that the change in orbital energy is typically defined by:

$$\Delta E_{\rm orb} = G\frac{M_1 M_2}{2\mathrm{a_i}} - G\frac{M_{1,\rm c} M_2}{2\mathrm{a_f}}, \tag{1.9}$$

where the parameter a denotes the initial and final separation of the system, M_1 is the total mass of the primary, M_2 is the mass of the companion, and $M_{1,\rm c}$ denotes the core mass of the primary.

Finally we introduce the efficiency parameter α, which describes the efficiency with which the orbital energy unbinds the envelope. Equation 1.10 is referred to as the "alpha formalism" equation:

$$G\frac{M_1 M_{1,\rm env}}{\lambda R_1} = \alpha\left(G\frac{M_1 M_2}{2a_{\rm i}} - G\frac{M_{1,\rm c} M_2}{2a_{\rm f}}\right). \tag{1.10}$$

It is worthwhile to note, however, that the parameter α has caused much confusion depending on its definition, and inclusion of specific energies such as stellar internal energies, and gravitational binding energies (De Marco et al., 2011; Ivanova et al., 2013).

1.3 Past Simulations of the Common Envelope Interaction

Binary and common envelope interactions are rarely observed outside of a few candidate objects such as the aforementioned V1309 Sco. These interactions are either very fast and hard to catch or slow and drawn out, making observations of these events equally challenging. Fortunately today the increase in time-resolved astronomical surveys, aimed at detecting fast events known as transients, has increased the number of interactions that we believe to be common envelopes (e.g., MacLeod et al., 2017).

Utilising computer simulation codes and visualisations we are able to generate models of these systems, with the aim to recreate and interpret the variables we are able to observe. There are a number of ways to model binary interactions and common envelopes. Detailed hydrodynamic models target the details of the physics and the generation of outputs such as ejection speeds or light properties which may be observed in any one given transient event. Additionally models can also make assumptions (based on known physics) and attempt to model a whole population of events statistically. The latter approach is carried out with population synthesis codes. They use statistical descriptions of stellar initial conditions, and from that generate predictions as to the nature of the systems' evolution (Ivanova et al., 2013). A non-exhaustive summary of some past simulation work mentioned in this thesis is detailed in Table 1.1, wherein simulations were chosen to demonstrate the variety of codes, mass ratios, and other such variables available in simulating the CE interaction.

Hydrodynamic approaches suffer in that the pre-CE phase unfolds on a thermal timescale, which then transitions to the dynamical timescale in-spiral, and then back to a thermal timescale for the self-regulated in-spiral, making numerical treatment of binary evolution difficult. Generally hydrodynamic codes can be separated into smoothed particle hydrodynamics (SPH) and Eulerian grid-based codes. The latter works by discretising space into a computational grid. Each cell is then assigned the average of hydrodynamic quantities. Another, more recent method for example however, is the use of moving-mesh codes such as AREPO (Springel, 2010), which effectively combine the advantages from both grid-based and particle-based codes. As the name suggests, such codes work on a moving, unstructured mesh, defined by the Voronoi tessellation of a set of discrete points. If the mesh were to stay stationary, it would resemble a more typical Eulerian grid-based code, and similarly, if the mesh cells were to move at the same speed at the fluid, they would share many of the characteristics of a Lagrangian particle-based code. By occupying this middle ground, moving-mesh

codes are able to adjust spatial resolution automatically and continuously, while maintaining and excellent reproduction of properties such as shock fronts and other discontinuities.

Lagrangian SPH codes in contrast rely on a particle based discretisation of the mass distribution, although these particles are best thought of not as physical particles, but as smoothed interpolation points of hydrodynamic quantities. There are many advantages to SPH codes in this manner, as they run very similarly to evolving collisionless N-body problems under the influence of gravity. One such advantage is that SPH is able to exploit this with the efficient methods developed to calculate self-gravity, a component that is fundamental to the CE interaction. Shocks too, which would otherwise be poorly reproduced in discretised codes due to the extreme gradients, can in fact be dealt with very effectively in SPH with artificial viscosity terms. These such dissipation terms in SPH are added explicitly, and can thus be directly translated into their physical meaning Price (2012b). Much like their grid-based counterparts though, they too become computationally expensive when higher resolution is needed to resolve phenomena such as instabilities and fluid flows. As Passy et al. (2012) demonstrated there are not clear cut advantages in using either of the two techniques for the CE interaction. Grid techniques help in regions of low density, where SPH techniques fail because the resolution is adaptive on density, while the clear advantage of SPH is the lack of a bounding box.

As we have described above, Tout & Hall (1991) determined that stable mass transfer would occur for mass ratios approximately larger than $q = 1.4$, which suggests stable mass transfer may only occur in systems with an an accretor that is already more massive than the donor. As such many simulations since have primarily focused on binary systems with q ratios less than unity, where the unstable mass transfer that leads to the formation of a CE interaction should be most prominent. Reichardt et al. (2019), for instance, simulated a giant star (equivalent to a polytropic system of $n = 1.5$), with a mass ratio of $q \equiv M_2/M_1 = 0.68$. Their simulations featured a primary RGB star of 0.88 $M_\odot$, and 90 $R_\odot$, with a compact companion of mass 0.6 $M_\odot$. This setup itself followed on directly from simulations done by Passy et al. (2012) and Iaconi et al. (2017a), but with the intention to extend the simulations to the new SPH code, PHANTOM (Price et al., 2018) and also to extend the simulation in time to the pre-in-spiral and post-in-spiral phases. By comparing the same simulation setup across 3 separate resolutions Reichardt et al. (2019) was able to conclude that the mass transfer rate is heavily resolution dependent, demonstrating that with higher resolution comes a longer

Simulation	M_1 ($M_\odot$)	M_2 ($M_\odot$)	$q \equiv \frac{M_2}{M_1}$	R_1 ($R_\odot$)	a_i ($R_\odot$)	a_f ($R_\odot$)	Code type	Magnetic field
Passy et al. (2012)	0.88	0.6	0.68	90	83	26.8	SPH	No
Nandez & Ivanova (2016)	1.195	0.4	0.335	29.48*	61.93	1.419	SPH	No
Iaconi et al. (2017a)	0.88	0.6	0.68	83	83	21	SPH	No
MacLeod et al. (2018a)	1	0.3	0.3	10	20.6	6	Grid	No
Reichardt et al. (2019)	0.88	0.6	0.68	90	218	30	SPH	No
Lau et al. (2022)	12	3	0.25	619	988	33.1	SPH	No

*Roche lobe radius of the donor

Table 1.1: A summary of relevant parameters from past simulation work. Variables are as follows: M_1 is the mass of the donor/primary, M_2 is the mass of the accretor/secondary, R_1 is the inital radius of the donor, a_i is the initial core separation, and a_f if the final core separation. Note that there are multiple simulations with many varied parameters in these past works, such as the use of multiple q values in Passy et al. (2012), what is presented here is a small sample of the total. Also note that MacLeod et al. (2018a) simulated only the pre-CE mass transfer phase, and not the full interaction.

period of initially stable mass transfer during RLOF. This study partly motivates the current project.

Prior to the study done by Reichardt et al. (2019), MacLeod et al. (2018a) investigated exclusively the early stages of mass transfer up to the onset of the CE phase in an attempt to understand the role that mass transfer might play in the creation of red nova transients. Much like the work done by Reichardt et al. (2019), the simulation was initiated at the onset of Roche lobe contact in order to best trace the mass flow rate from its earliest point. MacLeod et al. (2018a), however, used a 0.3 $M_\odot$companion with a 1 $M_\odot$RGB donor ($q = 0.3$ by design). They found that simulated models of RLOF mass transfer and mass loss through the outer Lagrange points could be well approximated by analytical expressions such as Equation 1.11:

$$\frac{\dot{a}}{a} = -2\frac{\dot{M}_d}{M_d}\left[1 - \left(\gamma_{\rm loss} + \frac{1}{2}\right)\frac{M_d}{M_d + M_a}\right]. \tag{1.11}$$

Where M_d and M_a are the donor and accretor stars respectively, and $\gamma_{\rm loss}$ parameterises the specific angular momentum of the lost mass.

Many past simulations have investigated the CE interaction by means of placing the

accretor on the surface of the donor and evolving the system from this close separation. Iaconi et al. (2017a) was among the first to investigate the early stages of RLOF, and the subsequent final separation, when the simulation is started with the companion placed farther away, at the onset of Roche lobe contact. These marginally wider separations generally involve a more prolonged period of RLOF and early mass transfer before beginning the in-spiral phase, compared to their surface counterparts. They found that in this regime, final separations are slightly larger, and the amount of unbound mass from the binary is somewhat greater. Through doing this type of simulation they came to the conclusion that it was the expansion of the donor, and not the spinning up of the star that causes a larger final separation.

Reichardt et al. (2019) found that during the rapid in-spiral phase of the CE, when the rate of binary separation is decreasing at its maximum rate is when the largest portion of envelope material becomes unbound, while material leaving the outer Lagrangian points before the in-spiral remains mostly bound. Past work by Pejcha et al. (2016) believed all of this pre-in-spiral material to become completely unbound from the system, however, it was shown by Reichardt et al. (2019) that the pre-in-spiral mass loss, for an adiabatic equation of state moves to much larger radii, but remains bound. This idea was also explored in MacLeod et al. (2018b) and MacLeod & Loeb (2020). There it was found that this bound material forms a toroidal distribution around the binary.

Similarly, the material that is ejected during the in-spiral, moves out from the centre of mass but remains mostly bound (as also found by all simulations using an ideal gas equation of state). This implies that bound gas must then either exist in equilibrium as a circum-binary disk, or eventually fall-back onto the binary.

With the inclusion of a tabulated equation of state, that includes the contributions of recombination energy, Reichardt et al. (2020) did find that a significantly larger portion of the envelope became unbound. The ratio of hydrogen to helium recombination energy depends on the mass of the host star, however, they generally found around 50% of the hydrogen recombination energy should be available to do work on the envelope, while all the helium recombination energy can be used to do work and help with unbinding. Recombination energy also seems to evacuate a substantial amount of the envelope during the self-regulated in-spiral phase, driving the expansion into conditions that may be ideal for dust formation (Reichardt et al., 2020). Considering the impact of this tabulated equation of state, and the presence of recombination energy are then crucial to accurately modelling the process of

mass transfer during RLOF and the rapid in-spiral phase.

Recombination energy had been previously investigated in the work of Ivanova & Nandez (2016); Nandez & Ivanova (2016) who had looked at systems with low-mass giant donors. Their models had recombination energies of approximately 4×10^{46} erg, which were then typically an order of magnitude less than that of their calculated binding energies. They found the radius at which recombination could take place and power the outflow of mass were smaller than the radii of typical giant stars, assuming the material had cooled enough. However, although the envelopes of evolved stars are too hot to allow for this recombination, the removal of matter due to RLOF can cause an expansion of the donor. Subsequently the inner shells move to the new equilibrium whereas this recombination radius, which depends on the gravitating core, shrinks. In certain cases they found this relation can lead to recombination runaway, capable of completely unbinding the envelope. Ivanova & Nandez (2016) also found this is exacerbated by larger companion masses, which bring more energy into the envelope, causing a larger expansion to such a radius as to allow for recombination to occur.

Similarly Lau et al. (2022) performed simulations featuring a significantly more massive red supergiant donor due to the inherent differences in envelope construction between low and high-mass giants. The radiation pressure present in these simulations was subsequently responsible for a larger final separation, as well as a higher fraction of ejected mass during the rapid in-spiral. The inclusion of recombination energy follows similarly from Ivanova & Nandez (2016) and Reichardt et al. (2020), in that a significantly larger fraction of the envelope's mas becomes unbound, potentially leading to a total unbinding. This inclusion of recombination energy also resulted in a larger final separation. Interestingly though, Lau et al. (2022) attributed much of the unbinding to helium recombination, noting that hydrogen recombination mainly occurs in gas that had already become unbound in their simulations.

MacLeod & Loeb (2020) notably also varied the polytropic index of their donor star across their simulations of early mass transfer and RLOF. In this way they modelled low mass, gas-pressure dominated systems with both convective and radiative envelopes. They found for more centrally condensed and radiative envelopes with polytropic indexes of $\Gamma = 1.35$, the orbital evolution occurred much more slowly than the stars with $\Gamma = 1.5$ simulated previously. This is a similar conclusion to that found by Hjellming & Webbink (1987), who also considered the adiabatic response to mass loss of both radiative and convective

envelopes. A donor with a more centrally condensed core has less mass at larger radii, and tends to contract when exposed to mass loss. As such the accretor in this case remains further from the donor for longer, resulting in a prolonged phase of early mass transfer, lasting an order of magnitude longer than in the case of $\Gamma = 1.5$ (MacLeod & Loeb, 2020).

1.4 Motivation of the Current Work

The study of the CE interaction with numerical simulations has spanned decades, and despite the large amount of knowledge that has now been obtained, much remains to be understood about this phase of binary stellar evolution. This thesis attempts to address, and offer further insight into a select few of these gaps.

The driving question, and the motivation for this thesis, is what happens to the CE phase when the q ratio approaches, and potentially exceeds unity. As the companion moves closer in mass to the primary star, and the phase of semi-stable mass transfer before the CE interaction becomes longer, how is the expulsion of mass prior to the dynamic in-spiral impacted. Would a CE simulation with better-reproduced pre-CE mass transfer lead to a systematically different CE in-spiral interaction? Would it lead to larger separations (such as those we observe in some post-AGB binaries; van Winckel (2003)). At the moment there is an analytical criterion for when systems should enter the CE interaction. As Tout & Hall (1991) found, unstable mass transfer, and thus a CE interaction and in-spiral should occur for systems with $q = M_2/M_1 < 1.43$. This has held true so far of many of the works cited previously, all of which have used q values less than unity. So can we explain why certain systems enter the CE phase? How critical is this mass ratio criterion, and could it be that given enough time, even stable mass transfer still result in a CE interactions. In this case, would the CE interaction be systematically different from one that happens in a classically unstable regime? To answer these questions we will be undertaking a study using multiple simulations featuring different values of $q \equiv M_2/M_1$.

Part of this study must then include an analysis of the early mass transfer in these binary systems, as the mass and angular momentum lost through the outer Lagrange points is what drives the initial orbital decay. As mentioned by Reichardt et al. (2019), material ejected from the binary early on does not necessarily become altogether unbound, but instead remains bound to the binary at a much larger radius. The question is then what becomes of this ejected

material? By studying the properties and kinematics of this gas, we wish to find whether or not the material has sufficient angular momentum to form a circum-binary disk, and at what radius it will come to equilibrium. Should a disk be formed, or indeed any other large scale structure, how much of it will have reached escape speed, and by extension, how much is likely to fall back onto the binary at a later point.

We also wish to know at what point in the CE interaction this material was ejected. Is any potential structure formed later on composed of the early mass lost through L_2, or is the majority of this marginally bound material ejected during the dynamic in-spiral? Furthermore, we can also ask if there is a kinematic distinction to be made between this early and later stage mass loss. Does the mass lost early through L_2 and later L_3 form a mold which comes to shape the material later ejected during the dynamic in-spiral, or does the latter overwhelm and overtake the former.

Assuming a binary system does experience the formation of a fall-back disk, we may come to find that the binary undergoes a secondary, albeit different CE interaction, due to the already mass reduced donor. As previous simulations have almost routinely produced final separations larger than the observations (Iaconi et al., 2017b), particularly with the more realistic inclusion of recombination energy, we also ask if it is possible for this fall-back mass to do enough work on the binary to further shrink its orbit, and how much of this fall-back mass would be needed to potentially reproduce observations. Work done previously by Kuruwita et al. (2016) has already shown that this orbital shrinkage by way of fall-back material is feasible, and lends credence to this concept, although in their case the fall-back would likely lead to a full merger.

Additionally we would like to further investigate the role recombination energy plays with a more robust equation of state, and will include a simulation as such for comparison. By doing so we hope to find meaningful distinctions or similarities between the characteristics of each simulation, particularly with reference to the role of early mass-loss.

Finally, previous simulations on early mass transfer have used diverse criteria to define the beginning of the in-spiral phase, each of which in turn have differing levels of consistency when used on other relevant simulations. As such, we also want to develop a more objective, and easily repeatable way to define the beginning of the rapid in-spiral phase, and thus the beginning of the CE interaction itself; this definition will be core to the work presented in this thesis.

2

Simulating the Common Envelope Interaction

We have previously discussed the importance of the CE interaction in binary stellar evolution, along with some of the areas we intend to address throughout this thesis. In this chapter we will introduce the methods by which we will investigate these CE interactions, including the code and its governing equations and physics, as well as the specifics of our particular simulation work. We begin foremost with a brief introduction to fluid dynamics, and a short elaboration on the differences between Eulerian grid-based codes, and Lagrangian SPH codes.

2.1 A Brief Introduction to Fluid Dynamics

Consider a physical scalar or vector quantity relevant to a fluid flow, such as temperature or velocity, being both a function of position, and time. Taking the multivariate derivative of

this quantity yields Equation 2.1, an operator known as the material derivative.

$$\frac{D}{Dt} \equiv \frac{\partial}{\partial t} + \mathbf{v} \cdot \nabla. \tag{2.1}$$

The material derivative, also known as the Lagrangian derivative, depends on how the material is being viewed, and as such is a useful tool for linking Eulerian and Lagrangian descriptions of fluid flows. Equation 2.1 holds true for the Eulerian view, which is to say, as a vector field sampled at a fixed point in space, where $\mathbf{v}$ is the velocity of the fluid in the reference frame of coordinate system $\mathbf{x}$.

From the Lagrangian perspective, that is, from the view of a particle in the fluid flow, its own frame of reference dictates that $\mathbf{v} = 0$. The vector field in this regard then only becomes a function of time concerning the state variables of the fluid particles themselves. Thus Equation 2.1 reduces to Equation 2.2:

$$\frac{D}{Dt} = \frac{\partial}{\partial t}. \tag{2.2}$$

As we will elaborate on in Section 2.2, it is this Lagrangian perspective that SPH codes operate on.

Using this Lagrangian view we can describe the acceleration of a compressible fluid in the absence of any viscosity with Equation 2.3, where ρ is the density of the fluid, P the fluid pressure, and $\mathbf{a}_{\text{ext}}$ is inclusive of any external forces present such as gravity (Price et al., 2018).

$$\frac{D\mathbf{v}}{Dt} = -\frac{\nabla P}{\rho} + \mathbf{a}_{\text{ext}}. \tag{2.3}$$

To solve the hydrodynamics of this compressible fluid flow, Equation 2.3 is paired with Equation 2.4, where u is the internal energy of the fluid, and Λ is inclusive of any dissipation and cooling terms that deviate from the otherwise adiabatic process (Price et al., 2018). This equation calculates the exchange between internal energy and any work done on the fluid through compression and expansion processes.

$$\frac{du}{dt} = -\frac{P}{\rho}(\nabla \cdot \mathbf{v}) + \Lambda_{\text{diss}}. \tag{2.4}$$

Another case of the Lagrangian derivative which we include for completion is the continuity equation (Equation 2.5), which enforces the conservation of mass within a system.

Here ρ is the density, and $\mathbf{v}$ is the velocity.

$$\frac{d\rho}{dt} + \nabla\rho \cdot \mathbf{v} = 0. \tag{2.5}$$

To obtain a relationship between pressure, density, and the internal energy to close this system of equations, we then require the introduction of an equation of state (EOS). For an ideal gas this takes the form (Price et al., 2018):

$$P = (\gamma - 1)\rho u, \tag{2.6}$$

where γ is the adiabatic index given by $\left(\frac{c_\mathrm{p}}{c_\mathrm{v}}\right)$, wherein $c_\mathrm{p} = \frac{\partial u}{\partial T}\big|_\mathrm{p}$, and $c_\mathrm{v} = \frac{\partial u}{\partial T}\big|_\mathrm{v}$, are the specific heat capacities at constant pressure and volume respectively. For a monatomic gas $\gamma = 5/3$. We may then also define the sound speed of the fluid, c_s, as:

$$c_\mathrm{s} = \sqrt{\frac{\gamma P}{\rho}}. \tag{2.7}$$

We can also use the ideal gas law, Equation 2.8, to relate the internal energy to the gas temperature, where k_B is Boltzmann's constant, μ is the mean molecular weight, and m_H is mass of a hydrogen atom (Price et al., 2018). We can also include a second term here for radiation pressure (a is the radiation constant), though typically this term only becomes significant for high-mass stars.

$$P = P_\mathrm{gas} + P_\mathrm{rad} = \frac{\rho k_\mathrm{B} T}{\mu m_\mathrm{H}} + \frac{1}{3} a T^4. \tag{2.8}$$

In doing so we can close the system of equations used for solving compressible hydrodynamics given by equations 2.3 and 2.4.

If the fluid cannot be considered an ideal gas, $\gamma = 5/3$ will not be true, and we cannot continue to use the EOS form in Equation 2.6. In this case we require a tabulated EOS which is more robust in its considerations for areas in which ionization and recombination is important. There is no singular form for such an EOS. They can instead be constructed from other equations of state using stellar astrophysics codes such as MESA.

2.2 Smoothed Particle Hydrodynamics

Smoothed particle hydrodynamics (SPH), is one of many computational techniques useful in the simulation of fluid flows. It uses a meshfree Lagragian method whereby the coordinate system moves with a discrete parcel of the fluid. The fluid itself is comprised of discrete particles whose resolution can be adjusted according to smoothing lengths based off variables such as density. These particles are strictly non-physical however, and are better thought of as a series of interpolation points for state variables like pressure.

Each particle in an SPH simulation has constant mass, but the volume of each particle has a unique scaling; each volume is inversely proportional to the number of neighbouring particles. This is a core feature of SPH codes and is what is responsible for the 'smoothed' nature of the particles. The density of the the gas is then given by the sum of these nearby masses, weighted by the smoothing kernel (Price et al., 2018):

$$\rho_{\mathrm{a}} = \sum_{b} m_{\mathrm{b}} W(|\mathbf{r}_{\mathrm{a}} - \mathbf{r}_{\mathrm{b}}|, h_{\mathrm{a}}), \tag{2.9}$$

where W is the smoothing kernel, and h denotes the smoothing length, a characteristic that describes how 'spread out' each particle is, with less dense particles having a larger smoothing length. Generally any scalar function that operates with respect to space can be written in the form:

$$f(\mathbf{r}) = \int_V f(\mathbf{r}')\delta(\mathbf{r} - \mathbf{r}')d\mathbf{r}'. \tag{2.10}$$

We may then generalise the Dirac delta function, in this case to the smoothing kernel, with the characteristic width of the smoothing length, h, such that the following property and normalisation hold (Cossins, 2010):

$$\lim_{h\to 0} W(\mathbf{r}, h) = \delta(\mathbf{r}), \tag{2.11}$$

$$\int_V W(\mathbf{r}, h)d\mathbf{r}' = 1. \tag{2.12}$$

This ensures our smoothing kernel is here analogous the Dirac delta function. Then for a density $\rho(\mathbf{r}')$ we can write $dV' = \frac{dm'}{\rho(\mathbf{r}')}$, such that from Equation 2.10 we obtain:

$$f(\mathbf{r}) = \int_V \frac{f(\mathbf{r}')}{\rho(\mathbf{r}')} W(\mathbf{r} - \mathbf{r}', h)\rho(\mathbf{r}')d\mathbf{r}'. \tag{2.13}$$

Which can then be discretised from a continuous field onto a series of particles by taking mass, $m = \rho(\mathbf{r}')d\mathbf{r}'$ such that Equation 2.13 now becomes:

$$f(\mathbf{r}) \approx \sum_i \frac{m_i}{\rho_i} f(\mathbf{r}_i) W(\mathbf{r} - \mathbf{r}_i, h), \tag{2.14}$$

where m_i and ρ_i are the mass and density of the ith particle and $f(\mathbf{r})$ is similarly the scalar value of said particle. Note that Equation 2.9 is recovered when the function $f(\mathbf{r}) = \rho$. The sum here would usually be over all particles in the simulation, but the smoothing kernel acts in such a way as to tend to zero beyond a radius of twice the smoothing length. In this way the sum only includes particles within $2h$ of the particle being considered. A common representation of such a smoothing kernel is given by the piece-wise M_4 cubic spline function (note that r is a scalar distance here) (Price et al., 2018):

$$W(r,h) = \frac{1}{\pi h^3} \begin{cases} 1 - \frac{3r^2}{2h^2} + \frac{3r^3}{4h^3} & \text{for } 0 \leq r < h, \\ \frac{1}{4}(2 - \frac{r}{h})^3 & \text{for } h \leq r < 2h, \\ 0 & \text{for } r \geq 2h. \end{cases} \tag{2.15}$$

An example of a more generic smoothing kernel example is the Gaussian defined by:

$$W(r,h) = \frac{1}{\pi\sqrt{\pi}h^3} e^{-\frac{r^2}{h^2}}. \tag{2.16}$$

The problem with such a kernel, however, is that it needs to be integrated over the entire simulation to obtain the correct result. The choice to cut it off at $2h$ would result in a discontinuity at $r = 2h$, whereas the M_4 cubic spline for comparison smoothly goes to 0 at the same point (Figure 2.1).

Finally, to describe the discrete particles in SPH codes, we require discretised forms for many of our continuous field equations from section 2.1. As we have already discretised our density in Equation 2.9, we now need to do the same for Equations 2.3, 2.4, and 2.6, that is, particle acceleration, internal energy, and pressure respectively.

Trivially we may discretise our particle pressure in Equation 2.6 such that it becomes:

$$P_a = (\gamma - 1)\rho_a u_a. \tag{2.17}$$

For the gradient of a scalar field we can continue from Equation 2.10 in a similar manner as before, noting that $\nabla \equiv \frac{\partial}{\partial \mathbf{r}}$. As the smoothing kernel W is the only part to depend on $\mathbf{r}$, we may again write that for a density $\rho(\mathbf{r}')$ we obtain (Cossins, 2010):

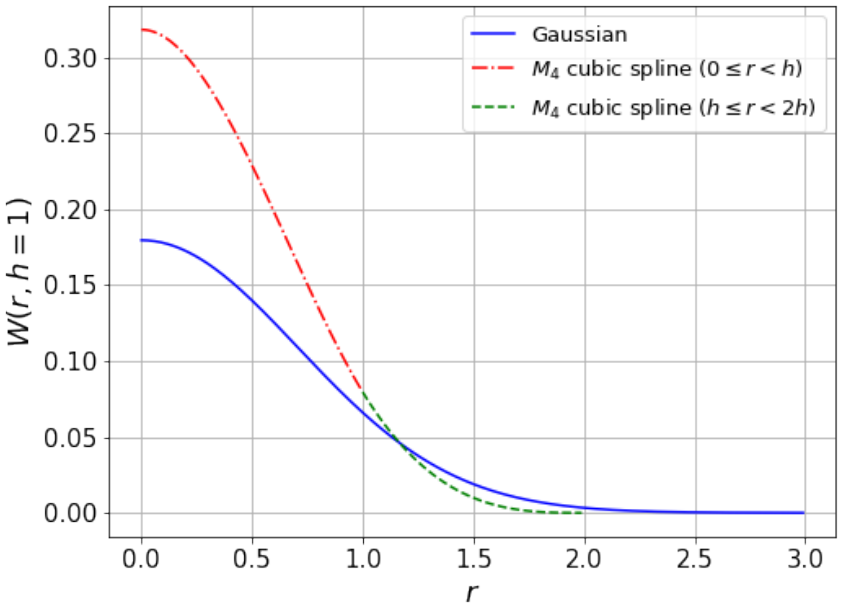

Figure 2.1: A comparison of the M_4 cubic spline and the Gaussian smoothing kernels' behaviour for a smoothing length, $h = 1$.

$$\nabla f(\mathbf{r}) = \int_V \frac{f(\mathbf{r}')}{\rho(\mathbf{r}')} \frac{\partial}{\partial \mathbf{r}} W(\mathbf{r} - \mathbf{r}', h) \rho(\mathbf{r}') d\mathbf{r}'. \tag{2.18}$$

Which when discretised similarly to Equation 2.14, becomes:

$$\nabla f(\mathbf{r}) \approx \sum_i \frac{m_i}{\rho_i} f(\mathbf{r}_i) \nabla W(\mathbf{r} - \mathbf{r}_i, h). \tag{2.19}$$

Thus taking $f(\mathbf{r}) = P_a$ we obtain a discretised expression for our ∇P term:

$$\nabla P_a = \sum_b \frac{m_b}{\rho_b} P_b \nabla W(\mathbf{r}_a - \mathbf{r}_b, h). \tag{2.20}$$

Whereas this is a valid discretisation, it is not the most accurate obtainable, and poorly conserves momentum (Price, 2012a). To improve our discretisation we use the Hamiltonian SPH formulation which more accurately respects local conservation of momentum between particles. As such we can use the identity in Equation 2.21 to modify Equation 2.20 (Cossins, 2010) (Note we desire the case in which $n = -1$, where n is either 1, or -1, as in the case of the reciprocal).

$$\nabla f \equiv \frac{1}{\rho^n} [\nabla (f \rho^n) - n f \rho^{n-1} \nabla \rho]. \tag{2.21}$$

This yields the following formulation that no longer accurately represents constant quantities, but is particularly useful in the case of the pressure gradient due to having the conservation of momentum present as desired for our case. Again taking $f(\mathbf{r}) = P_a$ yields:

$$\nabla P_a = \rho_a \sum_b m_b \left(\frac{P_a}{\rho_a^2} + \frac{P_b}{\rho_b^2} \right) \nabla W(\mathbf{r}_a - \mathbf{r}_b, h). \tag{2.22}$$

A similar argument to discretising the gradient of a scalar field can be made for the divergence of a scalar field, this time using the identity:

$$\nabla \cdot (\rho^n \mathbf{F}) \equiv \rho^n \nabla \cdot \mathbf{F} + n\rho^{n-1} \mathbf{F} \cdot \nabla \rho, \tag{2.23}$$

where again $n = -1$. We can then obtain the momentum conserved formulation for particle acceleration through the divergence of the velocity field (Cossins, 2010):

$$\nabla \cdot \mathbf{v} = \rho_a \sum_b \left(m_b \left(\frac{\mathbf{v}_a}{\rho_a^2} + \frac{\mathbf{v}_b}{\rho_b^2} \right) \right) \cdot \nabla W(\mathbf{r}_a - \mathbf{r}_b, h). \tag{2.24}$$

By substituting Equation 2.22 into Equation 2.3, and Equation 2.24 into Equation 2.4 respectively, we obtain:

$$\begin{aligned} \frac{d\mathbf{v}_a}{dt} &= -\sum_b m_b \left(\frac{P_a}{\rho_a^2} + \frac{P_b}{\rho_b^2} \right) \nabla W(\mathbf{r}_a - \mathbf{r}_b, h) + \mathbf{a}_{\text{ext},a}, \\ \frac{du_a}{dt} &= -P_a \sum_b \left(m_b \left(\frac{\mathbf{v}_a}{\rho_a^2} + \frac{\mathbf{v}_b}{\rho_b^2} \right) \right) \cdot \nabla W(\mathbf{r}_a - \mathbf{r}_b, h) + \Lambda_{\text{diss},a}. \end{aligned} \tag{2.25}$$

Thus together with Equation 2.9 and Equation 2.17, we have a complete set of discretised equations capable of describing the basic evolution of an SPH particle.

2.3 PHANTOM

PHANTOM (Price et al., 2018) is an SPH code designed to work with a number of astrophysical applications from planet and star formation to binary interactions, and includes a range of physics modules such as magneto-hydrodynamics, self-gravity, chemistry, dust formation, and more. Magnetic fields and chemistry are not important to this project, and as such we will only here consider the modules and equations that deal with self-gravity, as it is this gravity that is most integral to our CE simulations.

PHANTOM discretises the relevant fluid equations from the previous part in a similar though different form. Here the equations in 2.25 are written as:

$$\begin{aligned}\frac{d\mathbf{v}_a}{dt} = &-\sum_b m_b \left[\frac{P_a + q^a_{ab}}{\rho_a^2 \Omega_a}\nabla_a W(\mathbf{r}_a - \mathbf{r}_b, h_a) + \frac{P_b + q^b_{ab}}{\rho_b^2 \Omega_b}\nabla_a W(\mathbf{r}_a - \mathbf{r}_b, h_b)\right] \\ &+ \mathbf{a}_{\rm ext}(\mathbf{r}_a, t) + \mathbf{a}^a_{\rm sink-gas} + \mathbf{a}^a_{\rm selfgrav}, \\ \frac{du_a}{dt} = &\frac{P_a}{\rho_a^2 \Omega_a}\sum_b m_b(\mathbf{v}_a - \mathbf{v}_b)\cdot\nabla_a W(\mathbf{r}_a - \mathbf{r}_b, h_a) + \Lambda_{\rm shock} - \frac{\Lambda_{\rm cool}}{\rho}.\end{aligned} \tag{2.26}$$

For the fluid acceleration equation, the term q^a_{ab} is added to correctly model shock waves. The additional **a** terms are also expanded specifically into external forces, the sink and gas particle interactions, and the inclusion of self-gravity respectively. For the internal energy equation we also expand upon the λ terms by including specifically dissipation terms from shock waves with thermal conduction, and cooling from chemical interactions. Importantly the term Ω_a is included in both equations as a means of accounting for SPH particles with differing smoothing lengths, as is the case for PHANTOM, where:

$$\Omega_a \equiv 1 - \frac{\partial h_a}{\partial \rho_a}\sum_v m_b \frac{\partial W(\mathbf{r}_a - \mathbf{r}_b, h_a)}{\partial h_a}. \tag{2.27}$$

The derivative leading the expression can then also be expressed as (Price et al., 2018):

$$\frac{\partial h_a}{\partial \rho_a} = -\frac{3h_a}{\rho_a}. \tag{2.28}$$

In order to expedite the process of finding neighbouring particles much like other SPH codes, PHANTOM employs a *k*d-tree data structure. This process works by partitioning particles into cells by splitting the simulation through the centre of mass along a plane in one axis. This partitioning is then continued, each time along a plane that is perpendicular to the longest axis until a limit of $N_{\rm particles}$ is reached within that cell, called a 'leaf node'. Thus much of the simulation can be disregarded during a search for neighbouring particles based on these nodes and which particles are contained within.

Self-gravity in PHANTOM is given as a solution to Poisson's equation:

$$\nabla^2\Phi = 4\pi G\rho(\mathbf{r}), \tag{2.29}$$

where Φ is the gravitational potential. As this equation implies instant action, the global solution here is broken up into short and long range contributions. Short range contributions

are computed by direct summation over neighbouring particles, whereas the long range contributions are computed using the *k*d-tree to determine a hierarchical grouping of particles.

A key feature of SPH codes like PHANTOM is the ability to alter the length of the time step. This allows the simulation to ensure quantities such as velocity and acceleration are calculated in sufficiently small increments, while also minimising the computational cost. A common restriction to the timestep used in PHANTOM is the Courant condition (Price et al., 2018):

$$\Delta t_C = C_{\rm Cour}\frac{h}{v_{\rm sig}}, \tag{2.30}$$

where $C_{\rm Cour} = 0.3$ is the Courant factor criterion for stability found by Lattanzio et al. (1986), and $v_{\rm sig}$ is the maximum signal speed difference between neighbouring particles. This condition ensures that features such as shock and compression waves will cover an adequate number of time steps thus correctly resolving them in time. An example of two more conditions for the time step are given by (Price et al., 2018):

$$\Delta t_f^a = C_{\rm force}\sqrt{\frac{h_a}{|\mathbf{a}_a|}} \text{and} \tag{2.31}$$

$$\Delta t^a_{\rm sink-gas} = C_{\rm force}\sqrt{\frac{h_a}{|\mathbf{a}_{\rm sink-gas}|}}. \tag{2.32}$$

These are the 'force-condition' for the acceleration of particles, and a separate condition for accelerations due to/from sink particles respectively. What is chosen as the real time step for the simulation comes from the minimum of each of these conditions, such that:

$$\Delta t_a = \min(\Delta t_C, \Delta t_f^a, \Delta t^a_{\rm sink-gas}). \tag{2.33}$$

There is, however, an issue with using these conditions by themselves. For example, as the two sink particle cores of our stars in-spiral during the simulation, the gravitational acceleration will grow, causing the time step to shrink. With an endlessly shrinking time step due to the growing gravitational acceleration and potential, the simulation will grind to a halt. To solve this issue we need to introduce gravitational softening, and a softened potential.

Sink particles are important to our CE simulations. For the purposes of our work they are used to approximate the core of our RGB primary star and the core of our compact companion. These sink particles accrete no matter in our work, however, and act more

simply as point mass particles that interact with the gas exclusively through gravitation due to the negligible rate of interaction via collisions. This gravitational interaction between sink and gas particles is a 'softened' interaction. At large radii this is functions like the true potential, however at closer distances, on the order of the softening length, the interaction is significantly weakened. Here we will consider two ways to soften the true potential and low radii: the Plummer potential, and the cubic spline softened potential.

The gravitational potential at any given point in space due to a sink is given by:

$$\Phi(r, h) = -GM\phi(r, h_{\text{soft}}), \tag{2.34}$$

where $\phi(r, h_{soft}$ is the softening kernel. The Plummer softening kernel for example is given by:

$$\phi(r, h_{\text{soft}}) = (r^2 + h_{\text{soft}}^2)^{-1/2}. \tag{2.35}$$

That is to say, we can write the Plummer potential as:

$$\Phi(r, h_{\text{soft}}) = -\frac{GM}{\sqrt{r^2 + h_{\text{soft}}^2}}, \tag{2.36}$$

where M and h_{soft} are the mass and softening length of the sink particle respectively.

The density kernel and softening potential kernel are related to Poisson's equation with:

$$W(r, h_{\text{soft}}) = \frac{1}{4\pi r^2}\frac{\partial}{\partial r}\left(r^2\frac{\partial \phi}{\partial r}\right). \tag{2.37}$$

Integrating this equation allows us to solve for the softening kernel, which in our case is the M_4 cubic spline as before. Thus we obtain:

$$\phi(r, h_{\text{soft}}) = \begin{cases} \frac{r^5}{10h^6} - \frac{3r^4}{10h^6} + \frac{2r^2}{3h^3} - \frac{7}{5h} & \text{for } 0 \le r < 1, \\ -\frac{r^5}{30h^6} + \frac{3r^4}{10h^5} - \frac{r^3}{h^4} + \frac{4r^2}{3h^3} - \frac{8}{5h} + \frac{1}{15r} & \text{for } h \le r < 2h, \\ -\frac{1}{r} & \text{for } r \ge 2h. \end{cases} \tag{2.38}$$

Thus using this softening kernel allows us to find an appropriate function for Φ as before. The M_4 cubic spline potential is preferable to the Plummer potential due to its convergence to the true potential outside of $r = 2h_{\text{soft}}$, whereas the Plummer potential only converges to the true potential for $r \gg h_{\text{soft}}$. To demonstrate this, we plot these potentials in Figure 2.2.

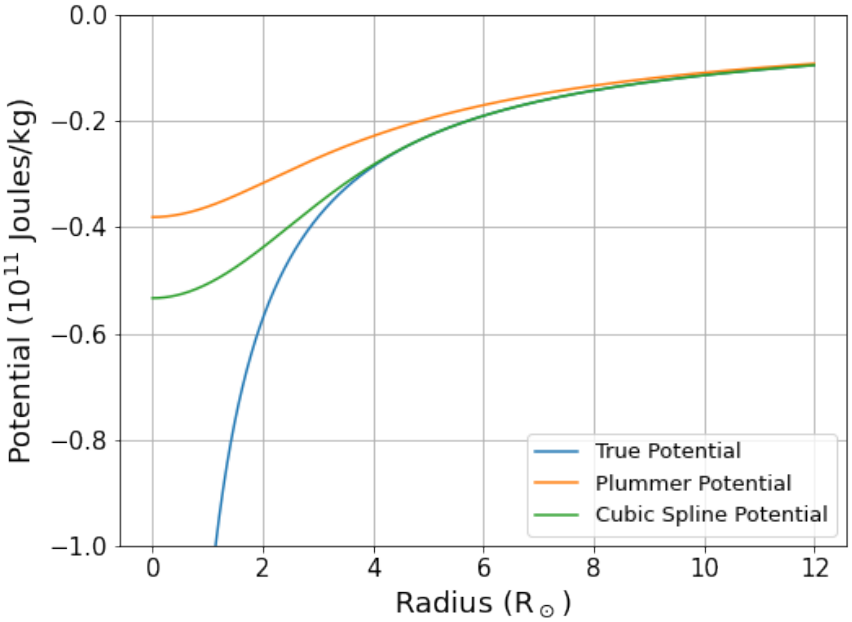

Figure 2.2: Comparison between the true potential, the Plummer softened potential, and the potential softened with the cubic spline. These were each calculated with a mass of 0.6 $M_\odot$, and a softening length of 3 $R_\odot$.

2.4 SPLASH

SPLASH (Price, 2007) is the tool used in this thesis to visualise the data provided by PHANTOM for each simulation. It is capable of providing both 2D plots and 3D renderings for a variety of useful quantities by default, as well as the ability to accommodate any needed additional quantities that can be calculated.

SPLASH also has the useful ability to colour and plot only specific particles. This is crucial in a number of ways to this thesis. For example we use it to count and visualise how much mass has left the radius of L_2 and at what time, as well as what is this material's long term behaviour, though we will revisit the specifics of that in Chapters 3 and 4.

2.5 A Note on the Definition of q

In this thesis we define $q \equiv M_2/M_1$, where M_2 is the companion, or accretor, and M_1 is the primary, or donor. Note however that q can also be defined by its reciprocal, $q \equiv M_1/M_2$, where M_1 and M_2 still reference the donor and accretor respectively. This definition has

been used in many previous works, notably that of Tout & Hall (1991), where for red giants it was expressly stated that by stable mass transfer would take place for $q < 0.7$, which by the definition used here is equivalent to $q > 1.43$. This had previously caused confusion in Reichardt et al. (2019) who mistakenly believed their simulations of $q = 0.68$ were coincidentally investigating the boundary of stability (despite the error in interpretation, this minor mistake did not affect their results or conclusions). A similar conclusion to Tout & Hall (1991) for the critical value of q was found by both Dan et al. (2011) and Frank et al. (2002). Both found that unstable mass transfer should occur for $q > 5/6 = 0.83$, but again there is confusion, as although their definition, like ours, is $q \equiv M_2/M_1$, the roles of M_1 and M_2 are switched such that they are the accretor and donor respectively. It is important to note here that Frank et al. (2002) uses M_1 for their compact primary, such as a white dwarf (WD), which is actually the accretor, while Dan et al. (2011) consider a case in which M_2 is a WD donor. In any case, rearranging their findings to fit our definition of q yields that stable mass transfer should occur for $q > 1.2$, which as expected from Tout & Hall (1991), is above unity.

To clarify this concept for the purposes of this thesis, there have been a number of ways to define q, and a number of system configurations determining what is the accretor and what is the donor. Ideally perhaps a definition of q that uses subscripts a and d, for accretor and donor respectively would be more prudent. Regardless, henceforth for this thesis, the parameter will be defined as $q \equiv M_2/M_1$, that is: compact, (generally) less massive accretor over the more massive donor.

2.6 The Simulations

In order to explore the early pre-CE phase of mass transfer and the resulting characteristics of the post-CE ejecta, we have generated eight unique PHANTOM simulations. Across these simulations we have varied three main parameters, $q \equiv M_2/M_1$, the resolution (number of SPH particles), and the simulation's EOS. Each of these parameters have a unique effect on the way the pre and post-CE phases occur, and by varying all of them we are able to perform a more comprehensive comparison, of both the differences and similarities in these evolutionary phases. See Table 2.1 for a brief summary of each simulation.

This project focuses on the boundary between mass loss stability and instability, so we have considered, as the lowest mass ratio the simulation, the $q = 0.68$ simulation from

Sim. q(Res)	$n_{\rm part}$ (1000)	M_2 ($M_\odot$)	a_0 ($R_\odot$)	$h_{\rm smooth}$ ($R_\odot$)	Total time (yr)
0.68(L)	76	0.6	218	0.53	10.1
0.68(H)	1070	0.6	218	0.19	20.1
0.85(L)	76	0.75	230	0.46	28.2
0.85(M)	138	0.75	230	0.41	15.2
0.85(H)	531	0.75	230	0.27	38.7
1.00(L)	76	0.88	235	0.46	35.4
1.00(H)	531	0.88	235	0.27	45.5
1.50(L)	76	1.32	255	0.46	40.4

(L) and (H) denote low and high resolution respectively.
(M) denotes the tabulated MESA EOS.

Table 2.1: Summary of the simulations used in this thesis, with some relevant initial conditions such as the companion mass M_2, and initial separation, a_0. $n_{\rm part}$ denotes the number of SPH particles in each simulation in multiples of 1000. Total time is the point at which it was decided to end the simulation. The radius of the donor star in all of our simulations is 90 $R_\odot$. We have also included the radius for the smallest particle smoothing length at time $t = 0$, $h_{\rm smooth}$. Note that $h_{\rm soft}$, the gravitational softening radius for both the primary, and secondary is 3 $R_\odot$ for all simulations.

Reichardt et al. (2019) and carried out additional simulations with larger values of q ranging to above unity. Much of the past work has been interested specifically in the unstable mass transfer that leads to the CE in low q systems. Whereas this is still of interest to us, we also wish to investigate systems with larger final separations; separations that are unlikely to have undergone a full CE, but have undoubtedly interacted in some manner before then. By increasing our mass ratios to unity and beyond, we would like to see just how stable the early mass transfer phase becomes, and how this might influence final separation.

Part of investigating the system's stability must also include a resolution study as Reichardt et al. (2019) has already shown that higher resolution leads to more stability. The issue of convergence is therefore an important one and variable resolutions must be used. Besides mass transfer stability it is already known (Reichardt et al., 2019) that a secondary period of mass unbinding occurs after the CE in-spiral has evacuated the orbit. The higher resolution

simulations experience virtually none of this, while the lower resolution simulations have a significant amount of mass unbound during the self regulated in-spiral. As such this phenomenon is artificial, but only through a resolution study can we come to this conclusion. In short, comparing resolutions assists in determining what characteristics are reflective of reality, and what are artifacts of the simulations themselves.

The final parameter we alter is the EOS, though only for one simulation at this time. For seven out of eight of our simulations we assume an ideal EOS. This is a relatively good approximation for our systems which is efficient and cheap to compute. Ideal gas, however, cannot simulate the release of recombination energy. Such energy release is responsible for an increase in the amount of envelope mass unbound, for example. We have included one simulation here with a tabulated EOS from MESA for $q = 0.85$. By including this we aim to extend our analysis one step further, while admitting a larger suite of simulations with a tabulated EOS still need to be carried out.

3

Pre-CE Mass Transfer Through The Inner Lagrange Point

In this chapter we analyse our eight simulations, starting with a new definition for the beginning of the CE in-spiral that we will use for the rest of this thesis. The stability and rate of mass transfer from the donor onto the accretor before the onset of the CE might have a significant impact on the CE outcome. In this chapter we will look at this early mass transfer through L_1 and investigate how it differs depending on the mass ratio, q, as well as on the resolution. From this we will begin to infer the impact this early phase has on the CE in-spiral experienced by the binary. Here we will also look at how analytical theory is reflected in our simulations regarding this early mass transfer during RLOF, and finally we will also confirm that our simulations are conserving quantities that must be conserved such as angular momentum and energy.

3.1 Defining the Beginning of the Common Envelope

Defining the beginning of the CE phase of a binary system is critical to understanding what separates systems that experience stable mass transfer, from systems that enter a CE (unstable, dynamic). Typically we observe this phase to be marked by a rapid in-spiral of the compact companion into the larger, more massive primary. The Roche lobe of the larger, typically more evolved star fills and begins to overflow mass onto its companion through the inner Lagrange point L_1. Eventually the system will begin losing mass and angular momentum through the outer Lagrange points, L_2 behind the companion, and L_3 behind the primary, causing a shrinkage in the orbital separation. Should this shrinkage progress to the point the companion enters the envelope of the primary, gravitational drag forces will lead to a runaway effect in which there is a period of rapid, dynamical in-spiral.

The length of the pre-in-spiral as well as the speed of the in-spiral, depend greatly on the simulation's resolution (Reichardt et al., 2019) and possibly on the mass ratio, q. This early phase of mass transfer before the in-spiral is generally well understood to be significantly longer in reality, compared to what is produced through simulations (MacLeod et al., 2018a). This is due to the effect of limited resolution. In SPH the minimum amount of mass transfer is set by the mass of the SPH particle. The very early mass transfer rate is expected to be very low, but in simulations this rate, set by resolution will be higher and invariably speeds up the entire process. The point at which this period of mass transfer gives way to the rapid in-spiral has been difficult to define in a way that is consistently reproducible and reasonably satisfactory.

One method of defining the beginning, and by extension, the end of the in-spiral, is using a multiple of the maximum in-spiral time scale. Reichardt et al. (2019) used $|\frac{\dot{a}}{a}| \geq \frac{1}{15}\max|\frac{\dot{a}}{a}|$ as a criterion for both the beginning and end of the CE in-spiral phase. In many circumstances this method produces a satisfactory result, but first relies on choosing a multiple, here $1/15$, of the timescale. Any one chosen number will work better in some cases than in others. This is a somewhat arbitrary process we would like to potentially avoid in the search for something more universal.

Before continuing, we clarify what it means for a definition to be 'satisfactory'. Generally we would like to choose a point on the plot of separation versus time that separates the pre-CE mass transfer phase from the start of the CE rapid in-spiral. However, as the descent into the in-spiral becomes more gradual for larger values of q, this transition point becomes less

obvious. Visually we expect this point to be somewhere toward the end of the longer lasting mass transfer phase, but before the separation starts to rapidly decrease. So in this way the method used by Reichardt et al. (2019) generates two points (magenta points in Figure 3.1) that are 'satisfactory' for 0.68L and H, 0.85L and H, but begin to fail to detect the start of the in-spiral for 1.00L.

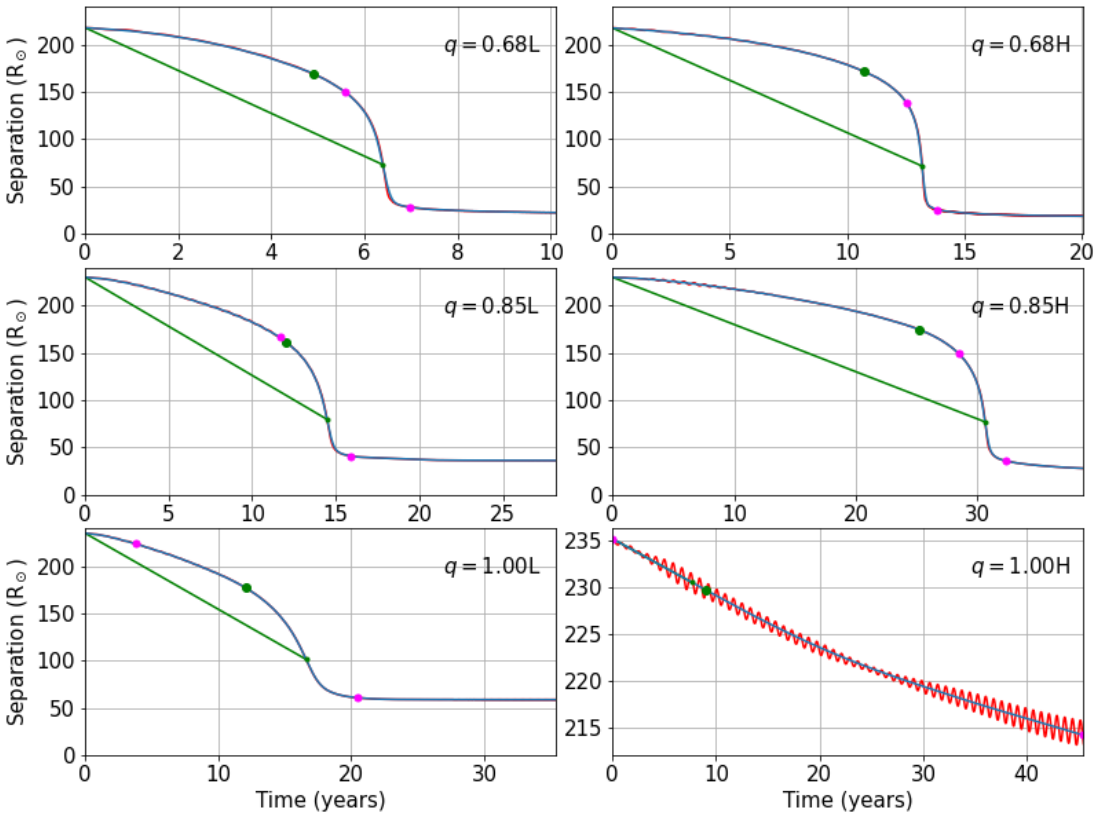

Figure 3.1: Separation as a function of time for the three simulations that have both low and high resolutions. The curve has been smoothed to make the location of certain points easier in the absence of eccentricity related oscillations. For reference, the original curves are included in red. The green line is drawn from the start of the simulation at Roche lobe contact to the point at which $\dot{a}$ is maximally negative. The green dots are the points at which the slope of this line is tangential to the curve. The magenta dots are the start and end of the in-spiral as determined by the criterion $|\frac{\dot{a}}{a}| \geq \frac{1}{15}\max|\frac{\dot{a}}{a}|$ (Reichardt et al., 2019). Note that neither criteria hold of the high resolution $q = 1.00$ simulation, as it has yet to in-spiral.

Another way to approach this problem is to take a more physical approach. For example, we might simply define the beginning of the CE to be the point at which the companion enters the envelope of the primary, which is to say, the point at which the separation is less than the

original radius of the donor. This definition is quite common and was suggested originally by Paczynski (1976). However, the nature of RLOF complicates this method. As gas is transferred from one star to its companion, the primary's envelope expands and is warped by tidal forces, making it difficult to determine when the companion has truly entered the envelope of the primary. In addition to this, the point at which the separation is equal to that of the primary's radius is 'unsatisfactory' in that much of the in-spiral has already occurred before this time. This criterion would be more suitable for simulations that begin with the companion on the surface of the primary in that they omit much of the in-spiral that occurs after the stars enter Roche lobe contact.

What we next suggest is a geometric criterion for defining the CE in-spiral start. On a plot of separation versus time we can draw a straight line from the beginning of the simulation to the point at which the rate of in-spiral is maximum. There is little to no ambiguity about the location of these points, and they completely encompass the early phase of mass transfer. The line segment between them then represents an average of the rate of change of the binary's separation. We then shift the line up and find the point at which it is tangential to the curve of the separation versus time. We call this the onset of the in-spiral. Limitations of this method, however, are that the best approximations are made when the graphical 'length' of the early mass transfer phase is approximately equal to that of the in-spiral. Fortunately this is true of the simulations presented in this thesis, however, should a significantly longer RLOF phase take place, this could result in a start of the CE that is visually too early in the evolution. The line and the point that derive from this method are depicted in green in Figure 3.1.

For the purposes of this thesis, we will be using the tangential line method to define the beginning of the CE dynamical in-spiral. These can be seen as the green dots in Figure 3.1. For each simulation these points, as well as a number of other relevant parameters relating to the in-spiral are summarised in Table 3.1.

3.2 Early Mass Loss and Transfer

The L_1, inner Lagrange point is the point of lowest potential outside of the two stars themselves, existing at the point of intersection of the Roche lobes of the stars. Thus as the donor fills its Roche lobe, the first instance of mass transfer occurs through L_1. At this point there is no energy input required for mass to flow from the Roche lobe of the donor into that of the

Sim.	$t_{\mathrm{i,T}}$	$a_{\mathrm{i,T}}$	$t_{\mathrm{i,R}}$	$a_{\mathrm{i,R}}$	$t_{\mathrm{f,R}}$	$a_{\mathrm{f,R}}$	t_{max}	a_{max}	τ_{max}
q(Res.)	(yr)	($R_\odot$)	(yr)	($R_\odot$)	(yr)	($R_\odot$)	(yr)	($R_\odot$)	(yr)
0.68(L)	4.9	170	5.6	150	7	28.1	6.4	73.3	0.3
0.68(H)	10.7	172	12.6	138	13.8	25.5	13.2	71.7	0.3
0.85(L)	12.1	161	11.7	167	15.9	40.8	14.5	79.5	0.9
0.85(M)	4.6	190	4.6	190	7.5	41.1	6.4	84.8	0.6
0.85(H)	25.1	175	28.4	150	32.3	35.5	30.6	76.9	0.9
1.00(L)	12.1	177	3.8	224	20.5	60.8	16.6	101.4	3.3
1.00(H)	-	-	-	-	-	-	7.6	231	360
1.50(L)	-	-	-	-	-	-	4.4	249	207

Table 3.1: Summary of parameters relevant to the CE. Here the subscripts i, f, and max, denote the beginning, end, and point of fastest in-spiral of the CE. The subscript T refers to the method of the tangential line (green dot in Figure 3.1). The subscript R denotes the criterion from Reichardt et al. (2019) (magenta dots in Figure 3.1). The time, separation, and timescale of the steepest point of the in-spiral are also provided here (where the right end of the green line meets the separation vs. time curve in Figure 3.1).

accretor. Mass will flow freely from one to the other, driven by the pressure gradient across L_1. Note that L_1 is a point in three-dimensional space, and it functions like a funnel for the mass to flow through. This funnel through L_1 can also vary in cross-section depending on the mass ratio, q and the separation between the bodies, leading to differing rates of transfer depending on the system. A decreased rate of mass transfer would generally be an indicator of stable mass transfer, for instance. By limiting the interaction with mass transfer there is also less transfer of angular momentum which ultimately drives the system into the instability that defines the CE. For a more in-depth discussion of the Lagrange points of a reduced three body system such as ours, please refer to Chapter 4; here, we will focus more on the properties of the mass transfer through L_1 itself.

Another factor that is crucial to studying the mass transfer of a system during these early stages of RLOF, is the margin by which is the star is overfilling its Roche lobe radius. We measure this quantity with $\Delta R/R_1$, as featured in Equation 3.1 and in Equation 3.3, where ΔR is the difference between the donor's radius and the donor's Roche lobe. Mass transfer is entirely contingent on the donor's radius being greater than that of its Roche lobe, but the

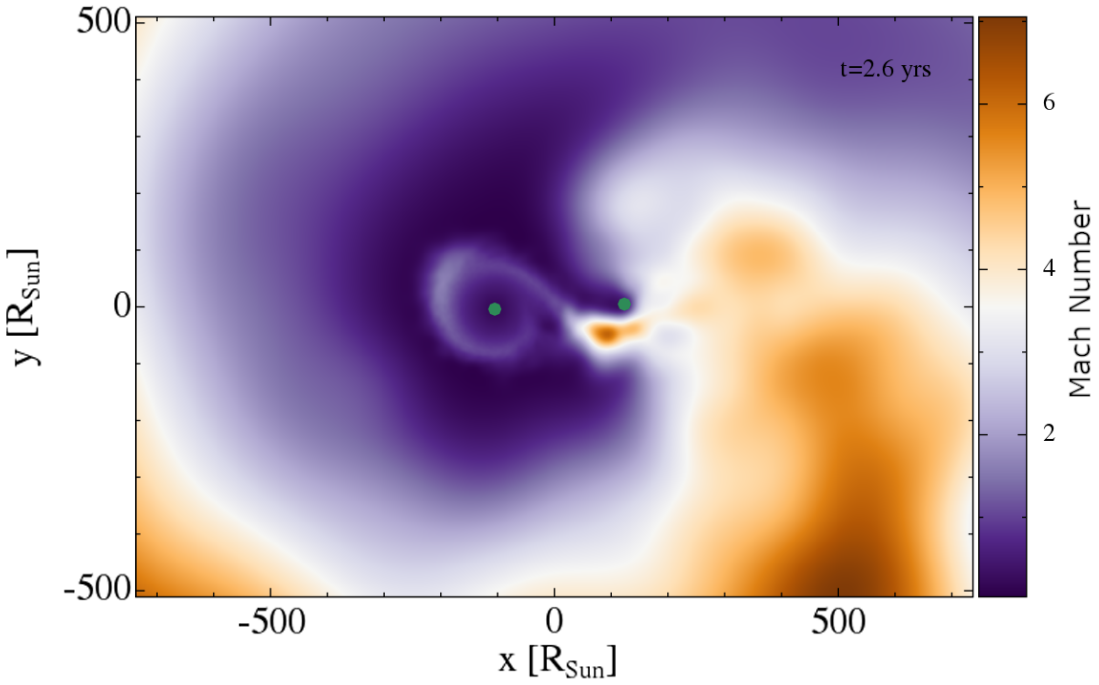

Figure 3.2: Orbital plane slice of the $q = 0.85$ high resolution simulation. The colour bar represents Mach number, thus demonstrating the subsonic to supersonic nature of the transition across L_1, and the two green dots represent the cores of the donor and accretor from left to right, respectively. Time was taken at an arbitrarily early point during RLOF to showcase this occurrence.

rate at which this transfer occurs is also heavily dependent on how large this difference is. This is perhaps most apparent in Equation 3.3.

Equation 3.1 assumes stable and conservative mass transfer, and was used by Reichardt et al. (2019) for their system (our $q = 0.68$ high resolution simulation). This is a reasonable assumption to make, because as we will see in Chapter 4, although some mass is lost early on during RLOF, the amount, particularly for high resolution simulations, is very small. This equation was originally derived by Paczyński & Sienkiewicz (1972), to describe the mass transfer through L_1:

$$\dot{M}_1 = -S_1 \left(\frac{\mu m_{\rm H}}{k_{\rm B} T}\right)^{1.5} W(M_{1,\rm rel}) \rho G^2 M_1^2 \left(\frac{\Delta R}{R_1}\right)^3, \tag{3.1}$$

where $S_1 \approx 0.215$ is a constant factor related to the polytropic index, μ is the mean molecular weight, m_H is the mass of a hydrogen atom, $k_{\rm B}$ is Boltzmann's constant, T is the temperature at the photosphere of the donor, ρ is its photospheric density, G is the gravitational constant, M_1 is the mass of the donor, calculated as the sum of each SPH particle within the radius of

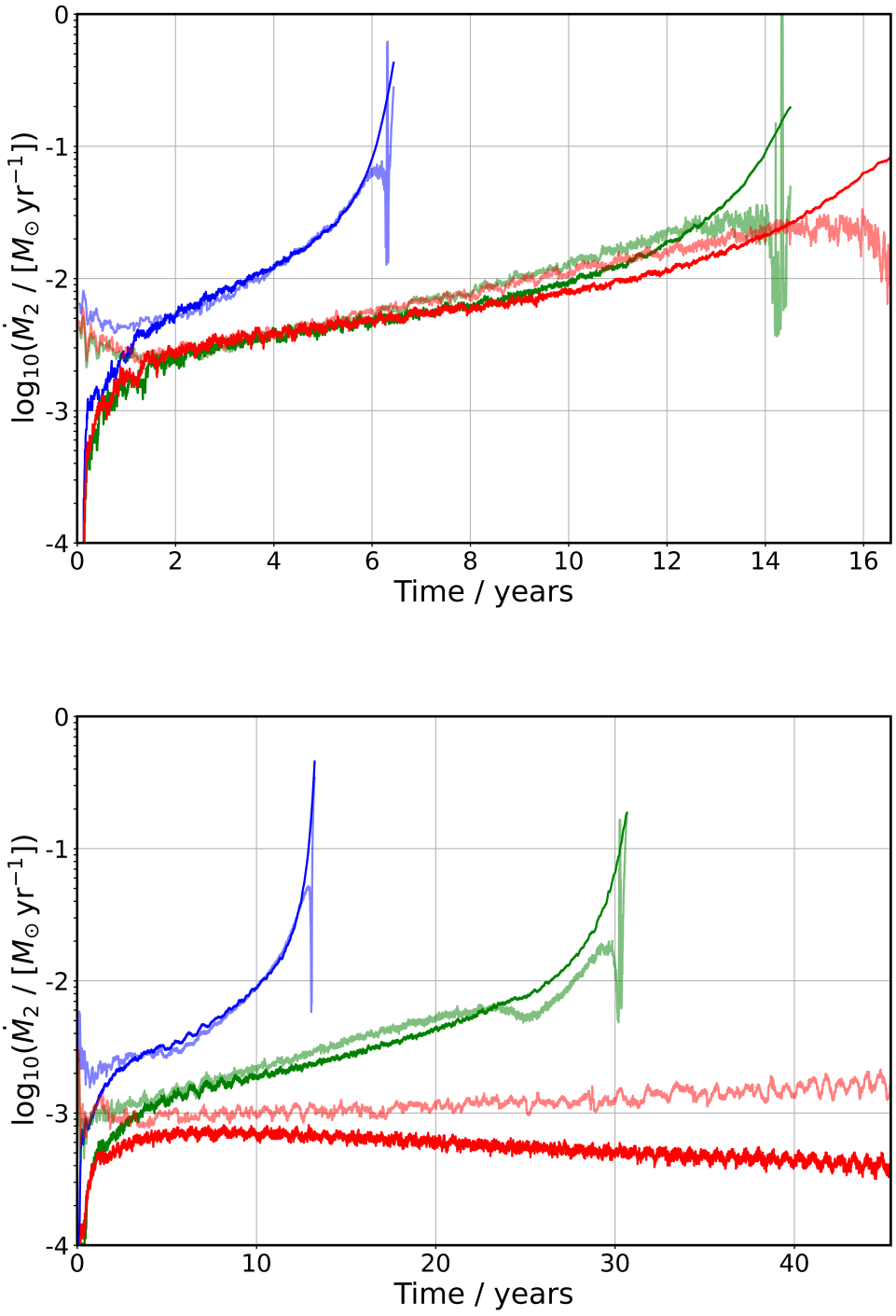

Figure 3.3: $\dot{M}_1$ for the low (top) and high (bottom) resolution simulations. As we have assumed conservative mass transfer, that which is lost by the donor is gained by the accretor. Here $q = 0.68$ is blue, $q = 0.85$ is green, and $q = 1.00$ is red. The darker lines are numerically calculated from the simulation, while the lighter lines are calculated with Equation 3.1.

the donor's Roche lobe, and $\Delta R = R_1 - R_{\mathrm{L},1}$, as mentioned previously, is a measure of how much the donor has exceeded its Roche lobe, R_1 being the radius of the donor and $R_{\mathrm{L},1}$ its Roche lobe radius. The quantity $W(M_{1,\mathrm{rel}})$ is a function of $M_{1,\mathrm{rel}} = M_1/(M_1 + M_2)$, defined as:

$$W(M_{1,\mathrm{rel}}) = \frac{\sqrt{M_{1,\mathrm{rel}}}\sqrt{1 - M_{1,\mathrm{rel}}}}{(\sqrt{M_{1,\mathrm{rel}}} + \sqrt{1 - M_{1,\mathrm{rel}}})^4} \left(\frac{aM_{1,\mathrm{rel}}}{R_{\mathrm{L},1}}\right)^{n+1.5}. \tag{3.2}$$

Here a is the orbital separation, and n is the polytropic index, taken to be 1.5 for a red giant such as ours. This equation does however also assume a co-rotating donor, as well as a transition from subsonic to supersonic speeds through the L_1 point. Reichardt et al. (2019) had only one co-rotating simulation, so similarly to that work, only the latter condition here is met by our work, as seen in Figure 3.2. Since our simulations generally use an ideal gas equation of state, we can make the substitution: $\frac{\mu m_{\mathrm{H}}}{k_{\mathrm{B}}T} = \frac{\rho}{P}$. Here ρ and P are the density and pressure respectively, at the surface of the star, which are obtained from the simulation. The radius of the donor is difficult to define due to the nature of the CE interaction, and both density and pressure, as well as the ΔR quantity rely on it. Here we define the initial radius of the donor using a volume equivalent, that is: $R_1 = \sqrt[3]{3V/4\pi}$. The total volume of the star is calculated by summing the volumes occupied by each SPH particle. The latter is calculated by dividing the (constant) SPH particle mass by its density. Note that this assumes that SPH particles are effectively spherical, so by nature there will be some gaps as well as overlapping of these volumes in the simulation. This means R_1 is perhaps the most contentious variable calculated here, and we would like to stress that both Equation 3.1 and Equation 3.3 include this quantity ($\Delta R = R_1 - R_{\mathrm{L}}$) to the third power.

In Figure 3.3 we compare the rate of mass transfer from M_1 onto M_2 as given by Equation 3.1 with the rate measured directly from the simulation. We calculate this latter quantity from the simulation by counting the SPH particles that move from the Roche lobe of the donor star into that of the companion and summing their mass. Once the CE has begun, however, the Roche geometry breaks down, and it no longer makes sense to count the mass transfer in this way. As such we cease the calculation for each simulation at $t = t_{\mathrm{i,T}}$ as defined in Table 3.1. Here we have also smoothed these mass transfer curves with a Savistky-Golay filter over a window of 35 data points, as the curves can be particularly noisy at low transfer rates. Since the method for calculating the mass transfer involves counting the SPH

particles that have changed Roche lobes between each time step (approximately 22 days), we have a minimum measurable mass transfer rate for each simulation. This minimum rate is approximately 1.0×10^{-4} $M_{\odot}yr^{-1}$ for the higher resolution simulations, and approximately 3.0×10^{-3} $M_{\odot}yr^{-1}$ for the lower resolution simulations. Thus particularly for early times in the simulation, rates below these values cannot be measured and the shape of the corresponding curves in Figure 3.3 are strictly due to the smoothing filter. It is only after approximately 1 year that the rates can be properly measured. Regarding the assumption of a co-rotating donor in Equation 3.1, we note that when comparing the simulated mass transfer to that given by the equation, the co-rotating primary in Reichardt et al. (2019) was arguably the worst approximated by this equation (their Figure 7). From Figure 3.3 it is clear we do have a good match between Equation 3.1 and our simulations, just as was the case in the comparison carried out by Reichardt et al. (2019), in all cases except for our high resolution $q = 1.00$ simulation.

There is clearly room for improvement however, when comparing this method of calculating mass loss rates and the numerical methods from the simulations. This is most evident in the behaviour of the mass loss rates at the start of each simulation as well as during the ascent towards the CE for which the analytical approximation displays a very different behaviour, not reflected in the simulations. Given how closely the equation matches the simulation it is unlikely that the equation does not wholly apply here. It might be possible that the uncertainty associated with our calculation of the donor's radius and ΔR are the cause, however as we will see, these same issues are not present in Figure 3.4. What is more likely is that these differences arise due to the $W(M_{1,\mathrm{rel}})$ term, and its heavy dependence on M_1 and $R_{\mathrm{L},1}$. Recall that $R_{\mathrm{L},1}$ is calculated using the approximation given in Eggleton (1983) (Equation 1.1), which itself is dependent on only q. However, because of the mass transfer process, the value of q is not constant, altering $R_{\mathrm{L},1}$ with time. Since an SPH particle leaving $R_{\mathrm{L},1}$ is part of how we measure this transfer, it is likely this is contributing to the discrepancies, particularly in the part of the curve that approaches the CE in-spiral, when the Roche geometry begins to break down. The percentage error in the two methods for the body of the curve were measured to be 2.4%, 12.4%, and 50.9% for the $q = 0.68, 0.85$ and 1.00 high resolution simulations respectively. The low resolution fits performed similarly with corresponding errors of 3.7%, 15.4%, and 3.4%, wherein the fit to the $q = 1.00$ simulation is clearly significantly better for the low resolution simulation. The reason for the distinct mismatch between our analytical

Simulation, q(Res.)	α
0.3†	1
0.68(L)	0.5
0.68(H)	0.4
0.85(L)	0.2
0.85(M)	0.15
0.85(H)	0.15
1.00(L)	0.2
1.00(H)	0.1

Table 3.2: A summary of the α values used to fit Equation 3.3 to what was measured numerically in Figure 3.4. We have included the simulation from MacLeod et al. (2018a) for comparison, denoted by †.

expression and what we measure numerically in the case of the $q = 1.00$ simulation is not immediately clear to us, but likely involves the behaviour of a resolution dependent parameter such as the density, ρ, or the pressure, P.

Another, simpler analytical equation for the mass transfer rates is given by MacLeod et al. (2018a):

$$\dot{M} \propto -\alpha \frac{M_{\rm d}}{P_{\rm orb}} \left(\frac{R_{\rm d} - R_{\rm L}}{R_{\rm d}} \right)^{n+\frac{3}{2}} . \tag{3.3}$$

This equation was similarly derived from Paczyński & Sienkiewicz (1972). Here $M_{\rm d}$ is the mass of the donor, which for us is M_1, $P_{\rm orb}$ is the orbital period, and similarly to the previous expression we have the difference between the radii of the donor and its Roche lobe, with an exponent featuring the polytopic index which is again, $n = 1.5$, resulting in the same dependence of the mass transfer on the $\Delta R/R_1$. Leading the expression is the factor α, which generally functions as a fitting parameter for this equation, and should not be confused with the efficiency parameter mentioned in Chapter 1. MacLeod et al. (2018a) found $\alpha \approx 1$ for their $q = 0.3$ simulation. Interestingly for larger q values, the value of α tends to decrease, as shown in Table 3.2.

In comparison to the expression given in Equation 3.1, this simpler expression predicts the mass transfer rates of our simulations exceptionally well. This is likely due to the diminished

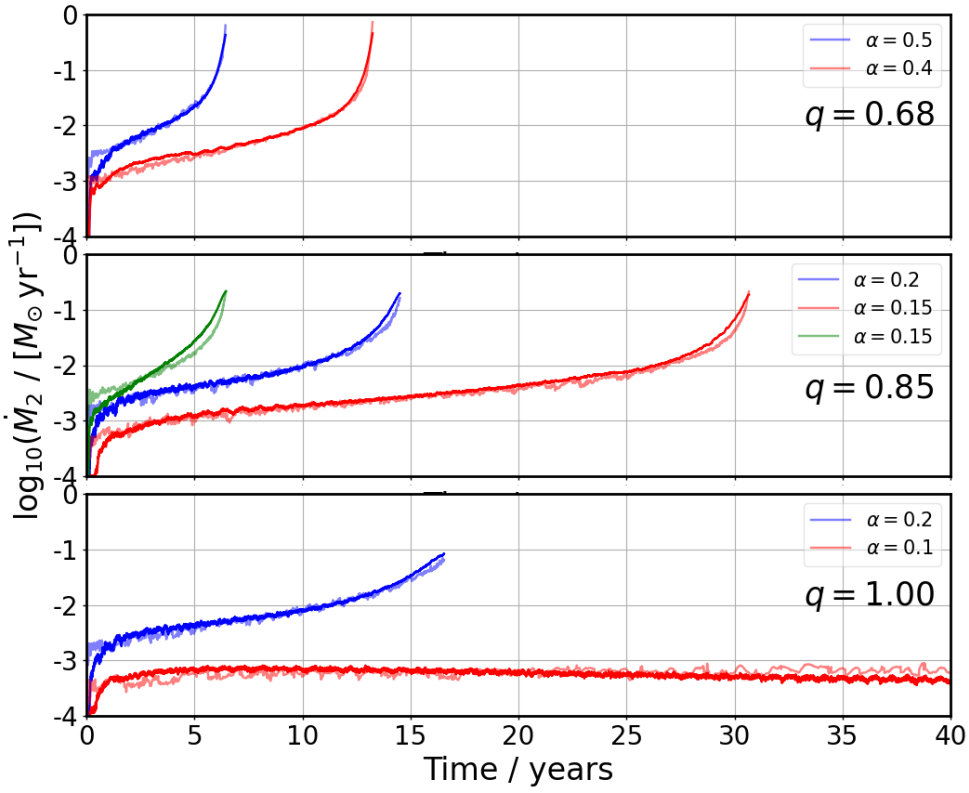

Figure 3.4: Mass loss rates for each low (blue) and high (red) simulation. The centre panel also features the mass loss rate for the MESA EOS simulation in green. The darker lines are calculated numerically from the simulation while the lighter lines are calculated analytically from Equation 3.3, where the parameter α in that equation is chosen for a best fit.

dependence on $R_{\mathrm{L},1}$ compared to Equation 3.1 with its additional $W(M_{1,\mathrm{rel}})$ term, as well as the inclusion of the orbital period, which may assist in tracking the mass transfer as said period shortens with the closing orbital separation.

More than any other simulations, our high resolution $q = 1.00$ and $q = 0.85$ MESA EOS simulations seems to be the most poorly modeled. The latter of which shows that Equation 3.3 does not fully capture the behaviour of a tabulated EOS as well as it does an ideal EOS. Figure 3.1 shows that for the high resolution $q = 1.00$ simulation there is no CE and no in-spiral present over the span of the simulation. There are two possibilities here. One is that the simulation has not run for long enough, and will eventually reach the point of entering the CE as the others have done. The second is that this system's mass transfer is stable, and will experience a different type of CE, if it indeed does experience one at all.

Whereas the former will be difficult to comment on without completing a longer run of the simulation, we can remark upon the latter. We can see that the separation in in Figure 3.1 (bottom right panel) appears to be beginning to level off (this is even more apparent for the $q = 1.50$ simulation - see Figure A.1 in the appendix). Whereas the separation still has room to shrink, the difference in inflection between this plot and the other five present in Figure 3.1 implies that the latter possibility: stability of some kind is possible, and that indeed the system may not enter a phase of rapid in-spiral. This is further evidenced by Figures 3.3 and 3.4, which show that the numerical rate of mass lost from the donor is plateauing, if not slightly decreasing over the span of the simulation. The analytical mass loss rates here show an important difference to the declining rates of the simulation. Equation 3.1 predicts the mass transfer increases, albeit much more slowly than the lower q counterparts, whereas Equation 3.3 predicts an approximately constant mass transfer rate.

The high resolution $q = 1.00$ simulation seems to imply that the boundary between unstable and stable mass transfer does lay at a mass ratio of approximately unity if not slightly higher, confirming that Dan et al. (2011); Frank et al. (2002) and Tout & Hall (1991) were correct in calculating that stability would occur for these mass ratios. The mass transfer rates are however resolution dependent as is clear from Figures 3.3 and 3.4, though the higher resolution simulations appear to reinforce this argument, as increasing resolution leads to greater stability, and a longer lasting phase of RLOF. Increasing resolution further is impractical, so the question of the actual length of the stable phase cannot be fully answered. We also need to know the impact of a MESA EOS on a high q and high resolution simulation, though unfortunately this will be an issue for future work as such a simulation is currently unfeasible for the length of this project.

Another way to compare numerical and analytical work in our simulation, is to compare the rate of in-spiral to an analytical expression based solely on angular momentum distribution. The total angular momentum budget for a binary system (excluding the spin of the stars, as is the case for our simulations) is given by Equation 3.4:

$$J = M_1 M_2 \sqrt{\frac{Ga}{M_1 + M_2}}. \tag{3.4}$$

In Table 3.3 we show that this generates the correct value for each binary system, comparing it with the results calculated directly from the simulation. Taking the derivative of this expression results in an expression for the in-spiral:

$$\frac{\dot{a}}{a} = \frac{2\dot{J}}{J} - \frac{2\dot{M}_1}{M_1} - \frac{2\dot{M}_2}{M_2} + \frac{\dot{M}_1 + \dot{M}_2}{M_1 + M_2}. \tag{3.5}$$

Angular momentum conservation in these simulations is excellent (within a fraction of a percent in all cases - see the left panel of Figure 3.6). Using the simulation we can measure individual quantities on this equation's right-hand-side and calculate the rate of in-spiral which can then be compared with that measured directly from the simulation. Here we again consider the mass of each star to be that within their respective Roche lobes, as well as summing the angular momentum, J, of both the point mass cores and the envelope gas within said Roche lobe. This is all done with respect to the centre of mass of the system. Notice that if we conserve angular momentum within these Roche lobes such that $\dot{J} = 0$ and also assume conservative mass transfer such that $\dot{M}_2 = -\dot{M}_1$ then we will have orbital shrinkage with $\dot{a} < 0$ regardless, so long as $M_1 > M_2$.

If $M_1 = M_2$ as is the case for our $q = 1$ simulation, then under the same circumstances $\dot{a} = 0$. Similarly if $M_1 < M_2$, like in our $q = 1.5$ simulation, then $\dot{a} > 0$, implying for these cases no orbital movement, and an increasing separation respectively. Since we know this to not be the case, $\dot{J}$ cannot be zero, and thus necessitates that mass and angular momentum must be lost through L_2, which we will explore in more depth in Chapter 4.

In Figure 3.5 we compare the low and high resolution $q = 0.68$ simulation for each iteration of Equation 3.5, as done by Reichardt et al. (2019). We plot the full expression, assuming $\dot{J} = 0$, or assuming fully conservative mass transfer, i.e., $\dot{M}_2 = -\dot{M}_1$. We also plot $\dot{a}/a$ as calculated directly from the simulation. There is no significant difference present here between the resolutions. The best match between the purely numerical curve and that constructed using individual quantities is by using the full equation. Unsurprisingly assuming $\dot{J} = 0$, with a mass losing M_1 we have a positive value for $\dot{a}/a$. The other two analytical curves then remain mainly negative, and are very similar to that measured by the simulation directly. Through this comparison we have separated the effects of angular momentum loss from that of mass transfer and thus confirmed that it is primarily angular momentum loss through L_2 and later L_3, that drives the decay of the orbital separation. After the trough in the plot, the system has undergone the rapid in-spiral of the CE, and as such the Roche geometry has broken down. This means that Equation 3.5 is no longer technically valid as $\dot{M}_1$ and $\dot{M}_2$ are calculated using the radius of their respective Roche lobes. The large oscillation in the blue line calculated from the simulation are due to orbital eccentricity and also partly the

Sim. q(Res.)	$J_{\rm tot,eq}$ (10^{52} erg s)	$J_{\rm tot,sim}$ (10^{52} erg s)	$J_{\rm u,i}$ (10^{52} erg s)	$J_{\rm u,f}$ (10^{52} erg s)
0.68(L)	3.87	3.87	0.37	1.56
0.68(H)	3.87	3.87	0.01	0.57
0.85(L)	4.73	4.72	0.89	1.12
0.85(M)	4.73	4.72	0.53	3.62
0.85(H)	4.73	4.72	0.22	0.31
1.00(L)	5.40	5.36	0.91	1.47
1.00(H)	5.40	5.38	-	-
1.50(L)	7.55	7.44	-	-

Table 3.3: In the first two columns we compare the binary's angular momentum given by 3.4, with that calculated directly from the simulation. We also track the amount of angular momentum that is unbound by the start of the CE (fourth column), and the amount that is unbound by the end of the CE (fifth column). This is reflected in Figure 3.6, and the similar plots in the appendix.

break down of the Roche geometry. The bulk behaviour remains the same, however there is a clear disparity between the numerical and analytic calculations at this point when compared to the time before the CE. See the appendix for the associated plots of the other simulations in this thesis.

Finally we check the conservation of both angular momentum as well as the energy of the system in Figure 3.6. In these simulations the cores of our stars interact with the gas only through gravity, and thus have no internal energy of their own. The total internal energy $U_{\rm tot}$ in Figure 3.6 thus exclusively belongs to the envelope gas. The energy of the envelope $E_{\rm env}$ comes close to 0 during and after the CE interaction, implying that it is only marginally bound. Indeed the envelope energy comes even closer to 0 in the high resolution $q = 0.68$ simulation (see A.3 in the appendix). It is possible then that should these simulations be redone with a MESA EOS, recombination energy could inject enough energy into the envelope so as to unbind it completely. Indeed, Table 3.3 shows that for the MESA EOS simulation, a much larger percentage of the total angular momentum is unbound during the CE compared to both the higher and lower resolution simulations. The bottom panels of Figure 3.6 also show that the MESA EOS simulation has a unique behaviour in that the angular momentum of

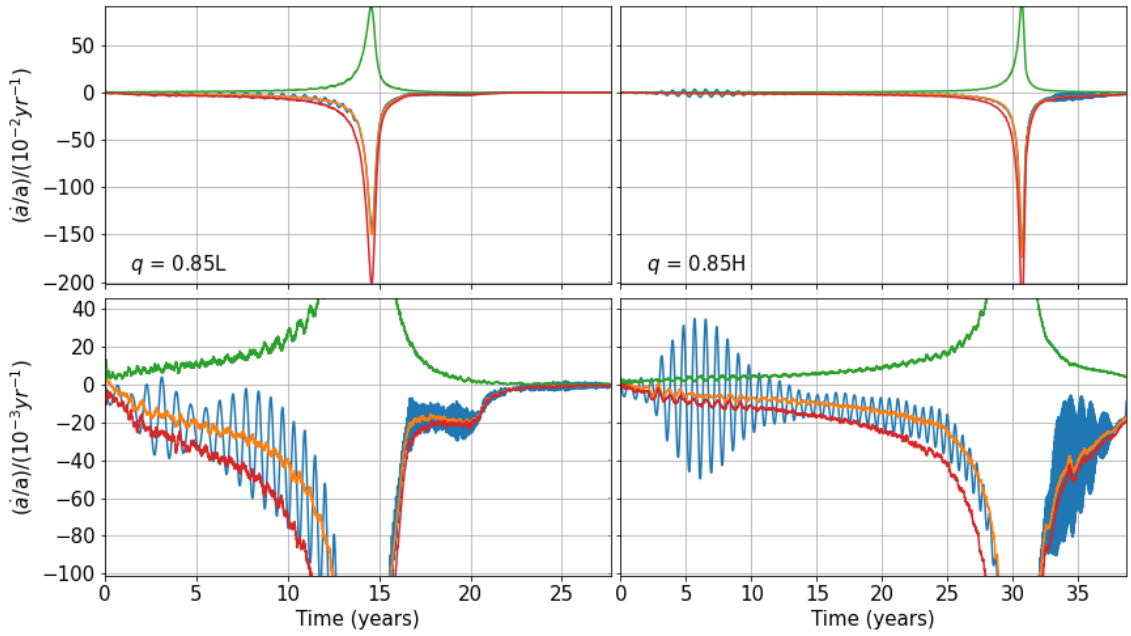

Figure 3.5: Comparison of the simulated orbital timescale (blue line) with the analytic timescale as computed by Equation 3.5 (orange line) for the low and high resolution $q = 0.85$ simulation (left and right panels, respectively). Here the green and red lines correspond to $\dot{J} = 0$ and $\dot{M}_2 = -\dot{M}_1$ respectively. The bottom panels are zoomed-in versions of the top panels.

the cores is not exchanged into the envelope as evenly, and in fact begins unbinding almost instantly. By the end of the simulation, virtually the entire envelope's angular momentum has become unbound, leaving the only that angular momentum associated with the cores bound to the system. We can also see in the bottom right plot of Figure 3.6 that with the inclusion of recombination energy, the envelope's energy ($E_{\rm env}$, purple dashed line) moves beyond zero. Interestingly this relatively low resolution MESA simulation does not exhibit the artificial unbinding of angular momentum present in the other low resolution simulations (see A.4 in the appendix), despite sharing the artificial unbinding of mass (which we will elaborate on in Chapter 4). As mentioned previously, our simulations conserve angular momentum (and energy) excellently to within less than a percent across all simulations. In the Left Panel of Figure 3.6 we plot the bound and unbound angular momentum of the envelope, as well as the orbital angular momentum of the cores. Note that we plot the z-component due to the bulk of the orbital motion occurring in the x-y plane.

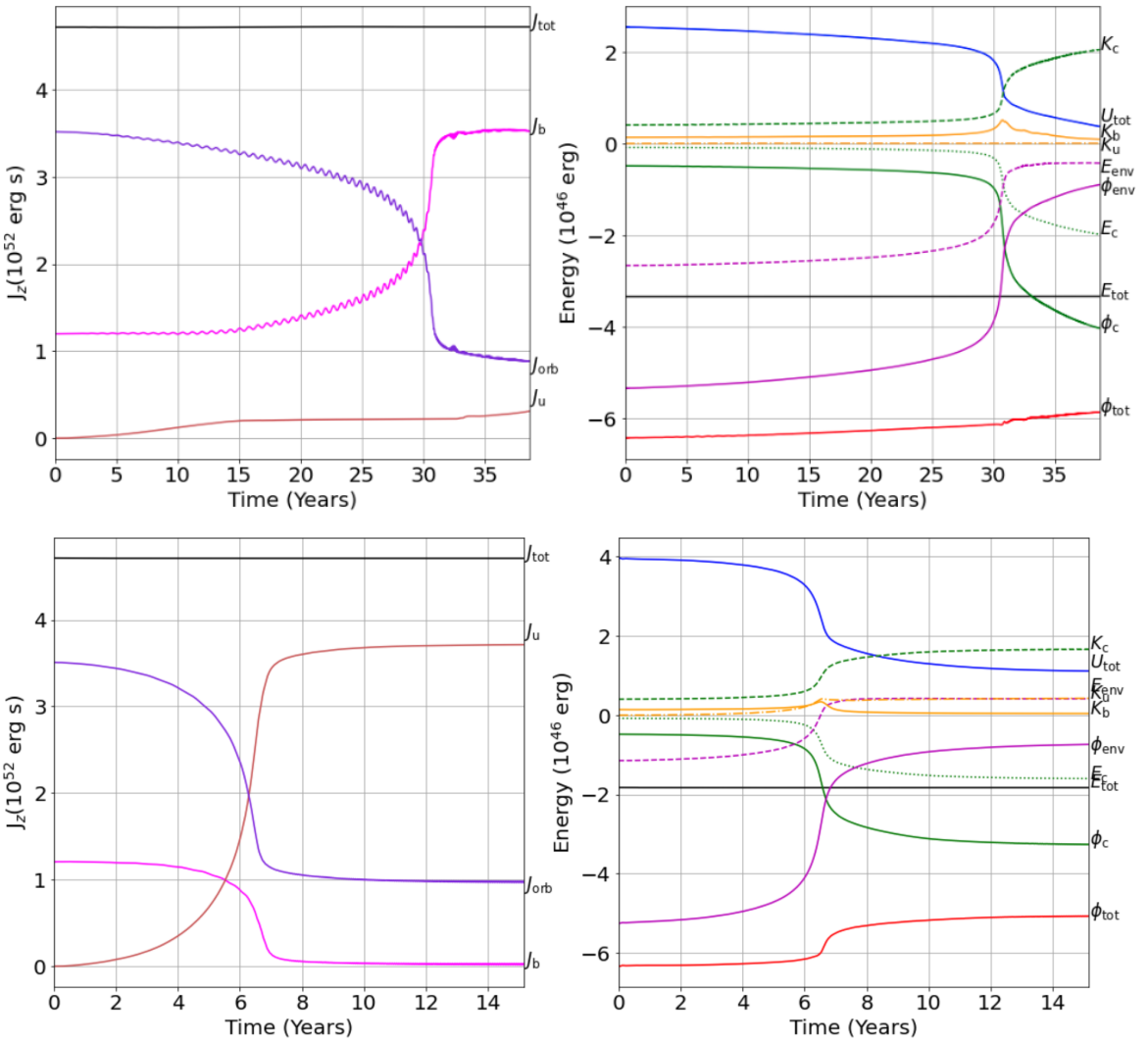

Figure 3.6: Angular momentum (left) and energy (right) components for the high resolution (top) and MESA EOS (bottom) $q = 0.85$ simulations. For the angular momentum plot, J_b (magenta) and J_u (brown) are angular momenta for the bound and unbound gas, respectively, while J_{orb} (purple) is the angular momentum of the point mass cores. Solid black lines in both plots are the total angular momentum and total energy of the system. In the energy plot we have in green: the total kinetic energy of the point mass cores (K_c, dashed), the orbital energy of said cores (E_c, dotted), and the potential energy between the cores (ϕ_c, solid). In yellow we have: K_b (solid) and K_u (dot-dashed), which are the bound and unbound kinetic energy of the envelope respectively. We also have in purple: E_{env} (dashed) and ϕ_{env}(solid), the total and potential energy of the envelope respectively. The total potential energy, ϕ_{tot} and the total internal energy U_{tot} are given by the red and blue lines respectively.

4

Mass Loss Characteristics of the Outer Lagrange Point

In the previous chapter we looked at the early stages of RLOF and the mass lost from the donor through L_1. We found that mass ratios closer to unity generally have a more stable, and longer lasting phase of mass transfer. In this chapter we will investigate the properties of the material that overfills the accretor's Roche lobe and is subsequently lost through the outer Lagrange point, L_2. The properties of this early outflow can then be compared to those of the material lost during the rapid in-spiral, allowing us to see whether or not this earlier mass is kinematically distinct, and what that may mean for any post-CE structure formation.

The Roche lobe mass transfer and mass loss phase may play a role in the outcome of the CE interaction. A central question of this work is whether this phase is dependent on the mass ratio q and whether these larger q ratios lead to a longer phase of RLOF (stable mass transfer). We have now have evidence to suggest this is the case, so the next question we ask is whether this results in more mass lost via L_2 and L_3 and, thus possibly, a weaker CE. In

other words, we wonder how much mass passed through L_1 and how much mass left L_2 prior to the CE in-spiral, what happens to the excreted mass (does it aggregate into a disk or does it leave the system), and how does this mass interact with the bulk of the CE ejection that follows.

It is worth noting at this point that for higher q values, the difference in potential between L_2 and its sibling on the opposite side of the system, L_3, becomes less and less, until the two points are effectively identical at a mass ratio of $q = 1$, and swap when q transitions above 1. For the purposes of this thesis we will only be considering the mass lost through L_2, as L_2 will generally be the first location of mass loss, and thus L_3 mass loss is vicariously captured within that. The differences in mass loss between the two for our simulations is also not significant enough to warrant an independent analysis of them separately.

4.1 The Second Lagrange Point, L_2

The Lagrange points of a reduced three body system are defined as equipotential contours in a co-rotating frame for which $\nabla\Phi = 0$, that is to say, there is no net force at these locations in such a frame, and objects are capable of sitting at these locations without any further input. In addition to this condition of no net force we find that in order to remain collinear, these points must move with the same period as the binary itself. Within this configuration there are some key points where the motion of the gas will have particular characteristics. The most important of these points are L_1, which lies between the two bodies and defines the point of intersection of the two Roche lobes (as discussed in Chapter 3), and L_2 and L_3, which lie on the outside of the less massive and more massive bodies, respectively. These three points are the most significant locations to consider when looking at mass transfer and any subsequent mass loss from the system. Each of these three points are saddle points, and are thus fundamentally unstable in some directions. Indeed it is this instability that allows mass to move between bodies during RLOF, and to leave the system once the potential wells of the two bodies have been filled. The other two points, L_4, and L_5, despite being potential 'hills' are in fact stable points of potential for a sufficiently large mass ratio due to the Coriolis force. The mass ratios required for this stability are of the order of at most $q \equiv \frac{M_2}{M_1} \approx 0.04$ (Schwarz et al., 2012). Indeed within our own Sun-Jupiter system many Trojan asteroids exist stably at L_4 and L_5.

L_2, and to a lesser extent L_3, are the most important points to consider when analysing the mass lost from a binary system. L_2 has the second lowest potential after L_1, and thus any mass lost from within the orbit of the binary will first occur through L_2. Note that in the case of $q = 1$, where both M_2 and M_1 share the same mass, L_2 and L_3 are at the same potential, and so mass loss can occur from both at the same time. Unless otherwise stated, in this specific case we will still consider the mass loss point of interest to be that on the outside of the accretor, though we stress that both L_2 points here are equidistant from the centre of mass, and as such our calculations of mass lost through L_2 are independent of which outer Lagrange point we choose.

4.1.1 The Location of L_2

There are many methods by which the location of L_2, and by extension the other Lagrange points can be found; none of which have a simple analytic expression. Here we will document three of the methods used to calculate the location of L_2 for completeness and comparison. By definition a Lagrange point is a point in a two body system at which there is no net force in the rotating reference frame, $F_{\rm net} = 0$, experienced by a test mass at that location. The only forces acting are gravity and the centrifugal force, and as such these must balance out:

$$\begin{aligned} F_{\rm net} &= 0, \\ F_{{\rm g},M_1} + F_{{\rm g},M_2} + F_{\rm c} &= 0, \end{aligned} \tag{4.1}$$

where $F_{\rm g,M_1}$ and $F_{\rm g,M_2}$ are the gravitational force on the test mass due to the donor and accretor, respectively, and $F_{\rm c}$ is the centrifugal force felt by this test mass with respect to the centre of mass of the binary. In addition to this zero net force, as mentioned above, these test masses must share the same angular velocity, ω, as the two bodies themselves about the centre of mass:

$$\omega = \sqrt{\frac{G(M_1 + M_2)}{R^3}}, \tag{4.2}$$

where R here is the separation between the core of the donor and accretor. Noting that $F_{\rm c} = m\omega^2 d$ (where d is the distance from the centre of mass), we can then write Equation 4.1 as:

$$-\frac{GM_1 m}{(R+r)^2} - \frac{GM_2 m}{r^2} + \frac{G(M_1 + M_2)m}{R^3}\left(r + \frac{M_1 R}{M_1 + M_2}\right) = 0, \tag{4.3}$$

where the first two terms are the force of gravity, with contributions from both M_1 and M_2 opposing the direction of the centrifugal force (third term) on a point mass, m, sitting at the location of L_2. Here R is again the distance between M_1 and M_2, and r is the distance between M_2 and L_2, i.e, the distance we wish to solve for. We stress here that M_1 must explicitly be the larger of the two masses (calculating this for the $q = 1.50$ simulation requires a swap of M_1 and M_2). The third term is the centrifugal force as experienced by the mass, m, from the centre of mass, where the second term in the parentheses is the distance from the centre of mass to M_2. Cancelling out the G and m factors, and rearranging we derive Equation 4.4:

$$\frac{M_1}{(R+r)^2} + \frac{M_2}{r^2} = \frac{M_1 + M_2}{R^3}\left(r + \frac{M_1 R}{M_1 + M_2}\right). \tag{4.4}$$

When expanded this becomes a quintic equation for r, and there is no trivial way to rearrange the expression to solve for r. What we do instead is plot both the left and right hand sides of this equation as a function of r. The intersection will then be the solution we seek. Note that this solution for r will specifically be the distance from the secondary to L_2. Figure 4.1 shows this method works via the familiar system of Earth and Sun, for which the location of L_2 is known to be approximately $1.5{\times}10^6$ km behind Earth.

The second method we used to find the location of L_2 involves considering the potential energy of the Lagrange points. Again we can write that the net force experienced at these Lagrange points is 0 because $\nabla\Phi = 0$. We start by defining the dimensionless quantity:

$$\mu = \frac{M_2}{M}, \tag{4.5}$$

where $M = M_1 + M_2$, thus $M_1 = (1-\mu)M$ and $M_2 = \mu M$. This quantity is the reduced mass of the binary, and can effectively be used as the distance of M_1 from the centre of mass assuming the non-dimensional distance between M_1 and M_2 is unity. In a rotating frame of reference the total potential energy of a particle with mass m is given by the equation:

$$U = -\frac{GM_1 m}{r_1} - \frac{GM_2 m}{r_2} - \frac{1}{2}m(r\omega)^2, \tag{4.6}$$

where the first two terms are the gravitational potential energy due to the two stars, and the third term is the centrifugal potential energy from the rotation of the reference frame. Note that the centrifugal potential energy has the form $U_c = \frac{L^2}{2mr^2}$, where we can write L, the angular momentum, as $L = mvr$ (and $v = r\omega$). The variables r_1 and r_2 are the distances from m to the respective masses, and r is the distance of m from the centre of mass.

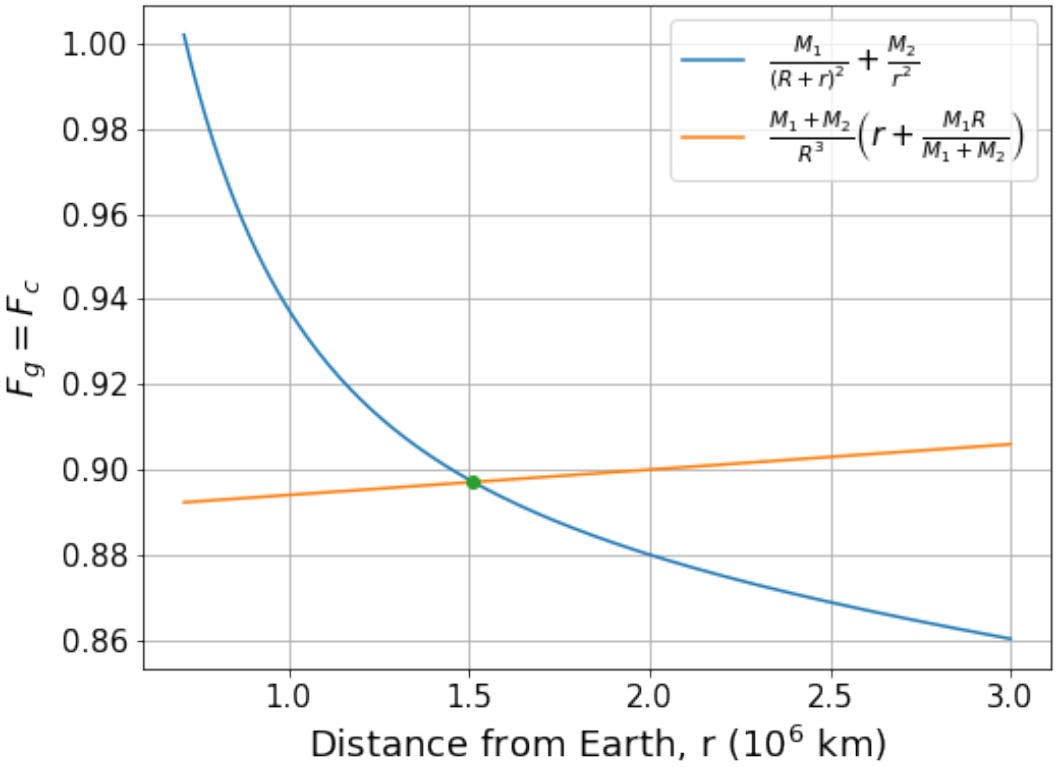

Figure 4.1: Comparing the gravitational forces due to M_1 and M_2 with the centripetal force experienced by a satellite point mass a distance r behind M_2. The intercept of these two forces gives the distance of L_2 from behind the secondary, in this case, Earth (here M_1 is the Sun).

Next we wish to make this equation dimensionless. We may rewrite M_1 and M_2 in terms of μ in Equation 4.6, as well as our distances r, r_1 and r_2 in the dimensionless form:

$$\alpha = \frac{r}{R}, \qquad \alpha_1 = \frac{r_1}{R}, \qquad \alpha_2 = \frac{r_2}{R}, \tag{4.7}$$

where R is the separation between our two bodies, and α is an arbitrary dimensionless variable. Doing so allows us to factor out the units in our expression such that we obtain:

$$U = \frac{GMm}{R}\left[-\frac{1-\mu}{\alpha_1} - \frac{\mu}{\alpha_2} - \frac{1}{2}\alpha^2\right]. \tag{4.8}$$

Now we consider only the terms inside the brackets, as the units outside function only as a scalar quantity. In order to make this expression more useful we need to rewrite these

Method=		$F_g = F_c$	$\nabla\Phi = 0$	Misra et al. (2020)
$q \equiv \frac{M_2}{M_1}$	a ($R_\odot$)	D_{L_2} ($R_\odot$)	D_{L_2} ($R_\odot$)	D_{L_2} ($R_\odot$)
0.5	200	316.5	316.5	315.3
1	200	340	339.8	339.7
1.5	200	126.5	126.2	125.1

Table 4.1: A comparison of the location of L_2 derived with three methods each of the three methods returns the same result for q values below, at, or above unity. Sample separation here is 200 $R_\odot$. The values calculated are distances in $R_\odot$ from M_1 (the donor star) to L_2, noting that L_2 switches sides for $q > 1$. For $q = 1$ we only consider the point on the outside of the accretor for brevity.

dimensionless α variables (recall these are functionally distances) in terms of an x-y co-ordinate system. We define this co-ordinate system as such:

$$\begin{aligned} \alpha^2 &= x^2 + y^2, \\ \alpha_1^2 &= (x+\mu)^2 + y^2, \\ \alpha_2^2 &= [x - (1-\mu)]^2 + y^2, \end{aligned} \tag{4.9}$$

then finally we arrive at a dimensionless, scalable expression for our systems potential given by:

$$\Phi = -\frac{1-\mu}{\sqrt{(x+\mu)^2 + y^2}} - \frac{\mu}{\sqrt{(x-(1-\mu))^2 + y^2}} - \frac{1}{2}(x^2 + y^2). \tag{4.10}$$

Thus when constructing contours of potential for our system we need only consider the three terms above.

For simplicity we assume $y = 0$, such that the Lagrange points L_1, L_2, and L_3 are collinear along the x-axis. To locate the points L_1, L_2, and L_3, we need only solve $\nabla\Phi = 0$, which has since reduced to $\frac{d\Phi}{dx} = 0$. Thus we obtain:

$$x - \frac{1-\mu}{(x+\mu)^2} - \frac{\mu}{(x-1+\mu)^2} = 0. \tag{4.11}$$

We can then solve this equation numerically for x, which will yield a dimensionless x coordinate for each Lagrange point. In order to find the distance of any point in the system

from any other point, we need only take the dimensionless distance between them, and multiply it by the original separation between the cores, R. Figure 4.2 shows two of our configurations generated through this method of potentials, based on our lowest and highest value for q. As a side note we have also included the points L_4 and L_5 in Figure 4.2. These are comparatively very easy to locate. They can be found with a simple application of geometry, in that if we consider an equilateral triangle for which M_1 and M_2 form two of the vertexes, then L_4 and L_5 will form the third, above and below the x-axis respectively. In other words they exist at the intersection of half the binary's separation, at an angle of 60° above and below the x-axis from M_1.

The final method for calculating the location of L_2 is numerical. Misra et al. (2020) derived a numerical approximation for the location of L_2 in terms of the Donor's Roche Lobe radius given by:

$$\frac{D_{L_2}}{R_{\mathrm{L}}} = \begin{cases} 3.334q^{0.514}e^{-0.052q} + 1.308 & \text{for } q \geq 1, \\ -0.040q^{0.866}e^{-0.040q} + 1.883 & \text{for } q < 1, \end{cases} \tag{4.12}$$

where D_{L_2} is is the distance from the donor, M_1, to L_2, and R_{L} is the Roche lobe radius of the donor. The donor's Roche lobe radius can be calculated using the form mentioned previously in Chapter 1 from Eggleton (1983) (Equation 1.1). A comparison of these three methods and the values they give for the location of L_2 is provided in Table 4.1. The differences between the values calculated is insignificant between methods, lending confidence to our understanding of where to find L_2.

In order to examine how the location of L_2 changes with time, we use the first method, equating gravitational and centrifugal forces, for each time step in the simulation; the result is plotted in Figure 4.3. Understanding where L_2 is at any given moment in time pre-CE is crucial to tracking the mass lost through L_2 as we will discuss in the next section. Worth noting is that we can see that the rate of decay for the L_2 separation differs between the point on the side of the companion and that of the primary for the $q = 1.00$ simulations, where L_2 and L_3 are interchangeable. This, however, does not mean the points move differently, in fact the two points remain equidistant from the centre of mass as well as maintaining the same distance behind their respective star.

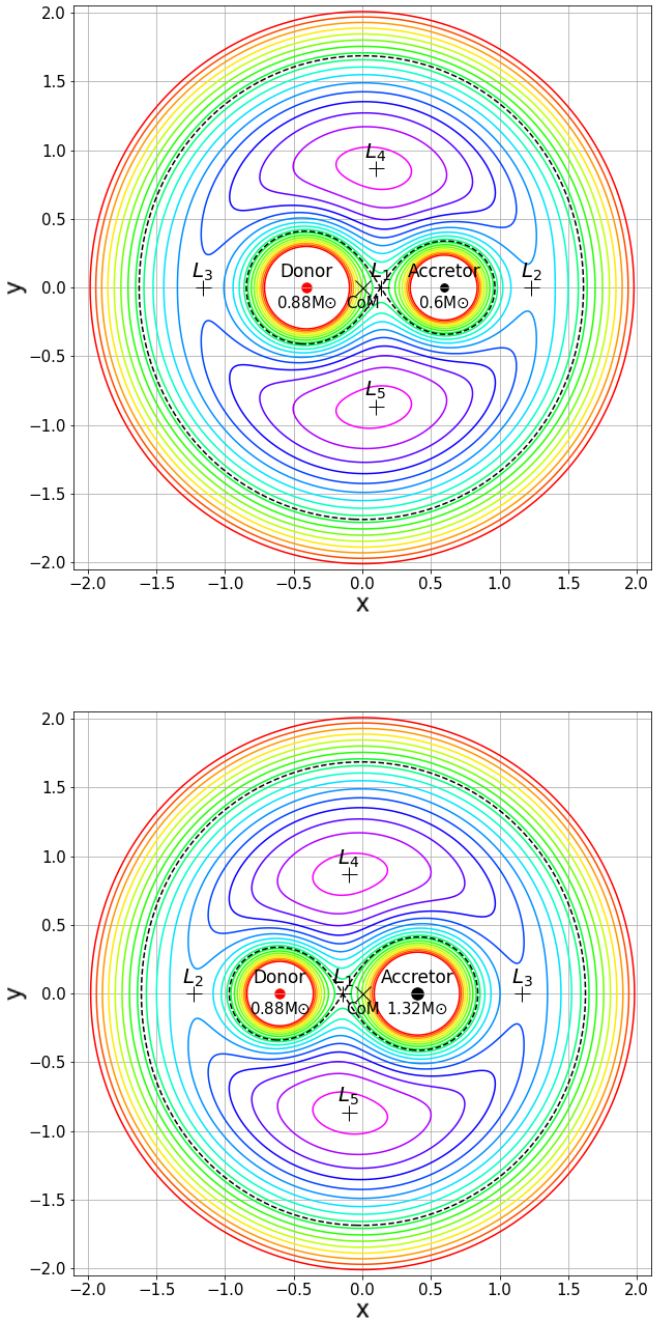

Figure 4.2: Contour plots for lines of potential, showing the locations of every Lagrange point, along with the centre of mass (CoM), and the masses of the donor and accretor. Configurations chosen for $q = 0.67$ (top panel) and $q = 1.50$ (bottom panel) the extremes of our range of q; note that as the donor has a mass smaller than the accretor (lower plane) L_2's position is now behind M_1. Note also that both the distances and the potentials are dimensionless. The black dashes lines here are the contours with the same potential as L_1, and so in the centre of the plot denote the Roche lobes of each star.

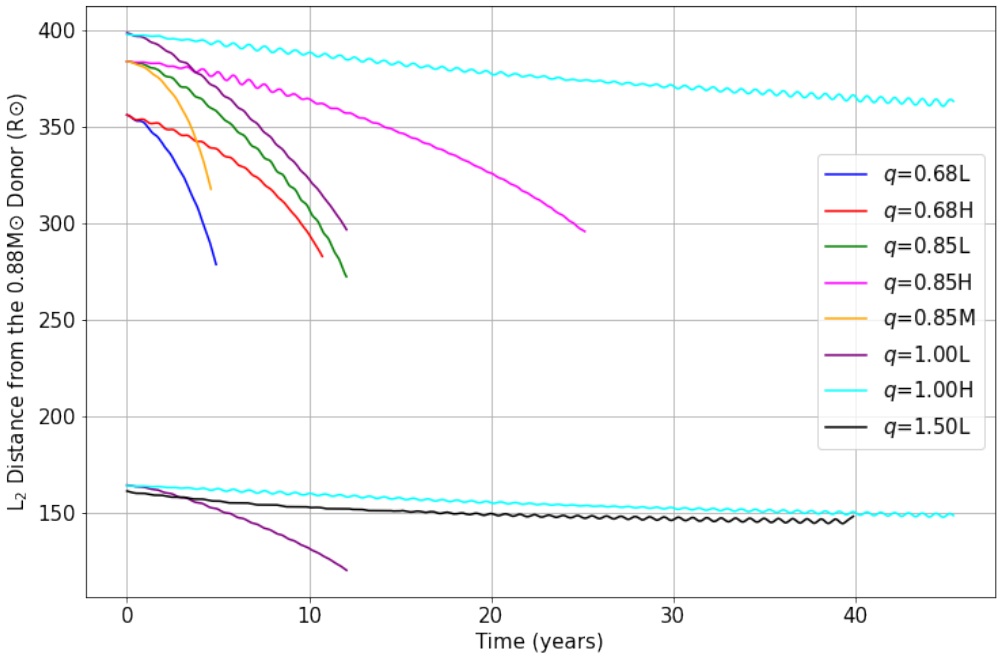

Figure 4.3: The distance between L_2 and M_1 as a function of time, obtained from the force balance method (Equation (4.4)) for each time step. Note there are two cyan and purple lines representing the $q = 1.00$ simulations, as the only difference between L_2 and L_3 in this case is what star they are on the outside of; because as mentioned previously, their potentials are equivalent.

4.2 The Mass Ejected Through L_2

SPLASH has the ability to track, colour, and plot specific particles as desired. As we can see from Figure 4.3 the distance of L_2 from the donor decreases by as much as 100 $R_\odot$ for some simulations, a not insignificant amount. Unfortunately SPLASH does not allow us to track the L_2 location as a function of time as we have done here. In order to differentiate between the particles ejected through L_2 before the time of the CE in-spiral and all other particles, we have chosen to select a *fixed* value for the distance of L_2 from either the centre of mass or the centre of the donor (SPLASH allows us to choose the origin). To make this distinction, we chose this fixed distance to be that of L_2 at the time of the CE in-spiral, selecting all particles outside of L_2 before that time to be the mass ejected before the CE in-spiral through L_2. The location of L_2 and the relevant time are summarised in Table 4.2, alongside the amount of mass ejected from L_2 as well as the mass ejected from L_2 that is unbound. Note

Sim. q(Res)	$a_{L_2,CE}$ ($R_\odot$)	t_{CE} (yr)	$M_{\geq L_2,CE}$ (/0.49 $M_\odot$)	$M_{\geq L_2,UB,CE}$ (/0.49 $M_\odot$)	$M_{\geq L_2,UB,End}$ (/0.49 $M_\odot$)	$M_{T,UB,CE}$ (/0.49 $M_\odot$)	$M_{T,UB,End}$ (/0.49 $M_\odot$)
0.68(L)	278.7	4.9	8.7%	5% 61%	8.7% 100%	6.1%	30.8%
0.68(H)	282.9	10.7	7.7%	0.2% 2.8%	7% 90%	1%	10.2%
0.85(L)	272.3	12.1	18.7%	14.5% 74.9%	17.8% 91.6%	15.7%	20.2%
0.85(M)	317.8	4.6	8.1%	6.4% 80%	8.1% 100%	7.5%	50.3%
0.85(H)	295.8	25.1	15.1%	3.4% 22.4%	3.9% 25.9%	5%	5.6%
1.00(L)	296.8	12.1	18%	14.6% 84.2%	17% 98.4%	15.7%	25.1%
1.00(H)†	363.4	45.4	5.4%	5.4% 99.5%	-	-	7%
1.50(L)†	148	39.9	9.5%	9.5% 100%	-	-	10.6%

†Did not undergo a CE, so end of simulation used instead.

Table 4.2: The first two columns are the distance of L_2 from the donor at the start of the CE in-spiral, and the time of the CE in-spiral. The following columns are percentage of envelope mass that is: outside L_2 at the start of in-spiral, outside L_2 at the start of in-spiral *and unbound* (black numbers are percentages of the total envelope, red numbers are percentages of the mass outside L_2 specifically), outside L_2 and unbound at the end of the simulation (black numbers are percentages of the total envelope, red numbers are percentages of the mass outside L_2 specifically), total mass unbound at the start of the CE, and total mass unbound at the end of the simulation. Note by the 'end' we here refer to the triangles in Figure 4.4. Note also that for the $q = 1.00$ simulation, choosing L_2 on the side of the donor did not meaningfully change the outcomes.

that the subscript of 'CE' denotes the time of the CE, which would be equivalent to our $t_{i,T}$ in Table 3.1 calculated using the method of tangent lines.

In Table 4.2 we see that for higher q values, more mass lost from the Roche lobes early on. This means it is likely there is then less mass available within the system for the CE to shrink the separation through drag forces. From this the CE, if any is to be experienced at all, is thus weaker, resulting in less in-spiral overall. The $q = 1.00$ low resolution simulation interestingly ejects about as much mass is the low resolution $q = 0.85$ simulation. This could imply there is a certain plateauing around 20% of the total mass that can leave the system before a CE ensues, though without a high resolution CE simulation for $q = 1.00$ it is difficult to tell what is simply an artifact of resolution, and whether the trend would continue in such a simulation.

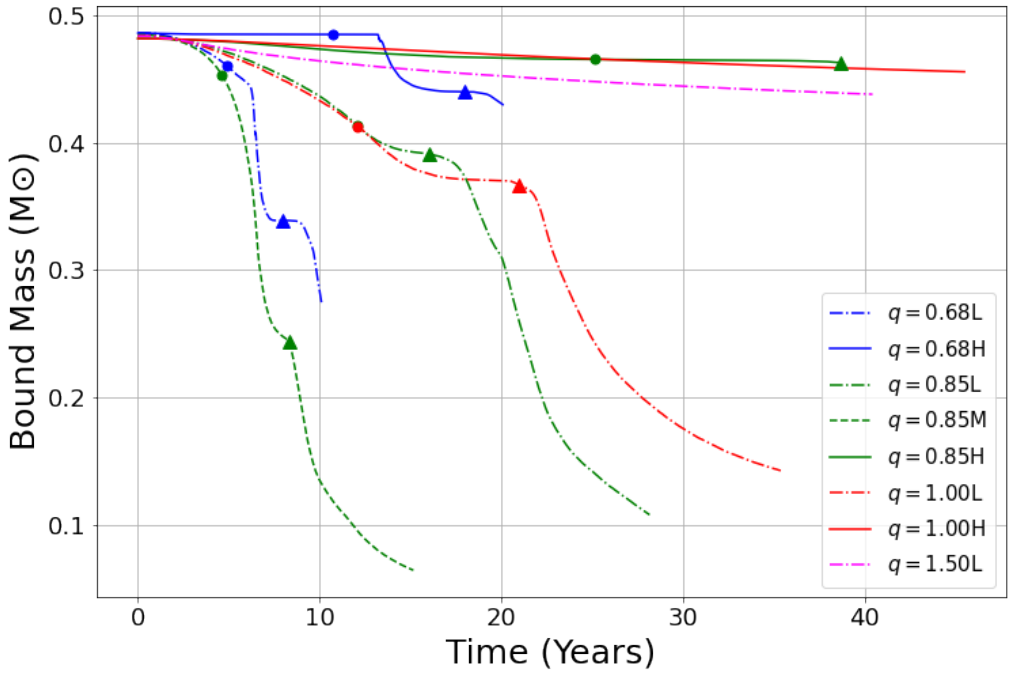

Figure 4.4: The evolution of each system's bound mass. Here the dots denote the start of the CE as defined in Chapter 3, while the triangles denote the time at which the resolution-dependent mass unbinding is estimated to start and the end of the viable simulation.

Although the high resolution $q = 1.00$ and low resolution $q = 1.50$ simulations did not undergo a CE, we include them here in Table 4.2 to capture any trends that may emerge. Despite the wide separations both simulations still exist at, indicating there will not be a CE in the near future of these systems, both have already unbound a higher percentage of their envelopes than the high resolution $q = 0.85$ simulation. This might have been expected for the low resolution $q = 1.50$ simulation, given that they tend to unbind more, but the fact that the pre-CE mass transfer phase in the high resolution $q = 1.00$ simulation has already unbound more than its lower q counterpart did entirely is interesting. It is possible that the increasing eccentricity our last two simulations are experiencing could be the culprit, however we would need to observe a CE from these systems to make a true comparison. For instance, it could be possible the early total unbinding of L_2 material we see from both teeters off as they enter a CE, leading to percentages not too far removed from their lower q counterparts. Unfortunately such an investigation is out of the scope available for this project at this time.

As expected lower resolution simulations also unbind significantly more than their higher

resolution counterparts across the board. In SPH codes, every particle has the same mass, and so with less particles overall, the loss of one counts as more than it would otherwise in the high resolution counterparts. The more accurate reason for this increased unbinding at low resolution however lies in the way the code is discretized, and subsequently the way gradients are calculated. In the same way a curved line may become smoother as more points are added along it, so too do these gradients become smoother with higher resolution.

Also expected is that at the time of the CE for higher resolution simulations, much of the mass lost through L_2 before hand remains bound - see the smaller red percentages in the 5th column. This was also found to be the case in Reichardt et al. (2019) and MacLeod et al. (2018a). Though as we have also found, by the end of the CE most of this previously bound material gets overwhelmed by the later, generally more massive and faster ejecta from the CE, resulting in a further unbinding of the material that had previously left L_2 before the CE. This means much of the material available for any fallback onto the system will likely come from the material ejected during the CE itself, and not from that ejected though L_2 before the start of the in-spiral. That is to say, the L_2 material does not remain kinematically distinct from the CE material, and given enough time, it is overwhelmed and partially accelerated by the CE material.

Figure 4.4 shows the evolution of the bound mass for each simulation, with the dots indicating the start of the CE as defined by the method of tangent lines in Chapter 3. When calculating the unbound mass for each simulation we stop after the point of the triangles. This is because the additional unbinding that occurs is heavily resolution dependent (as can be gauged by the fact that it is most prominent in the lower resolution simulations). After the point indicated by the triangles the two cores have mostly stabilised their orbit, and we do not expect additional unbinding. In fact, since the triangles are a good approximation for the end of the CE, from this point onwards they will be used as such, and define the end of the CE for this thesis.

Additional unbinding at this time is due to the marginally bound material receiving a small energetic bump that pushes it over the edge into being unbound. This additional unbinding is artificial, and not a real indication of the amount of material that is truly unbound. The exact cause of why this is occurs was explored by Reichardt et al. (2019) and Gonzalez-Bolivar et al. (2022), who concluded that the diminished density of gas around the cores, the local smoothing length of the gas particles exceeds that of the softening radius of the point mass

cores. This means the point mass cores are no longer well resolved, and the SPH gas particles acquire ballistic orbits that accelerate and transfer their kinetic energy to overlaying material, possibly unbinding it. For the purposes of this thesis we do not wish to consider any unbound angular momentum or mass after the end of the in-spiral, when the binary's orbit has once again stabilised. As we will see in Chapter 5, when calculating the fallback radius of any relevant material, the artificial unbinding of both mass and angular momentum can have a significant impact on the subsequent result.

Using SPLASH we have visualised slices of density and radial velocity at the beginning and the end of the CE in-spiral for each of our simulations, plotting all particles present, as well as only those beyond the radius of L_2 at the time of in-spiral. Figures 4.5, 4.6, and 4.7 show the slices in the orbital and perpendicular planes. Comparing the top two boxes with the lower two boxes we can visualise where L_2 is, and what the distribution of particles outside of that point looks like. Comparing the left set of boxes with the right set in turn allows us to compare the start of the CE with the end of the CE (circles and triangles, respectively in Figure 4.4).

Here we see that the material that has left L_2 is significantly less dense than the rest of the system, as implied by Table 4.2, and that this material has moved to much larger radii outside the binary, with relatively high positive radial velocity. In fact the majority of the material with a negative radial velocity belongs to that ejected during the CE. As Table 4.2 shows, much of the material ejected through L_2 prior to the CE does become unbound by the CE's conclusion.

The radial velocities depicted in Figures 4.5, 4.6, and 4.7 similarly show that there is an outwardly moving front beyond escape velocity (which we will verify shortly). Whereas the radial velocity by itself is not a conclusive measure of whether or not material will fall back, it is indicative of future behaviour, particularly after the CE's conclusion. We stress that regarding the radial velocity plots, the colour bar and its range here were chosen specifically to be reflective of just how much fallback mass there is, that is to say, there is not a large amount of material with a negative radial velocity present at late stages of the system (as we will see in Chapter 5). The magnitudes of said material's velocities are also much lower than those moving outwards with a positive radial velocity.

As we know from Table 4.2 the high resolution $q = 0.85$ simulation unbinds less material after the CE. This can roughly be seen in the relatively small amount of mass ejected from

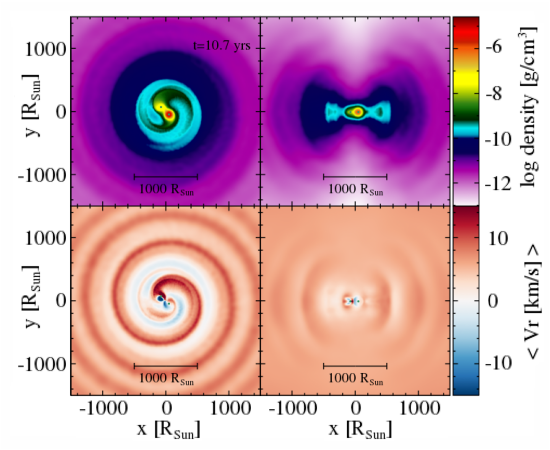

(a) CE start, all particles.

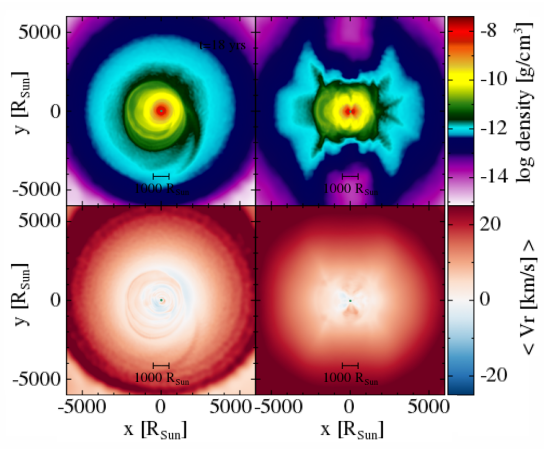

(b) CE end, all particles.

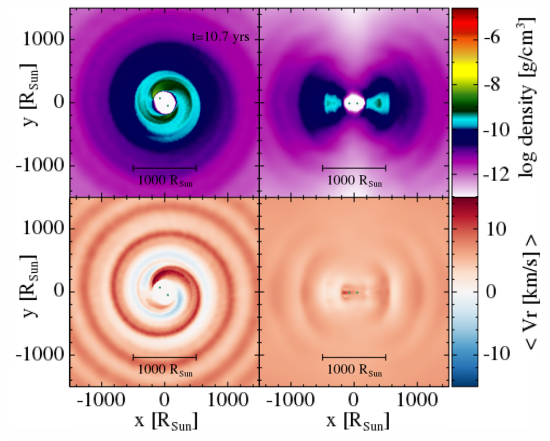

(c) CE start, L_2 particles.

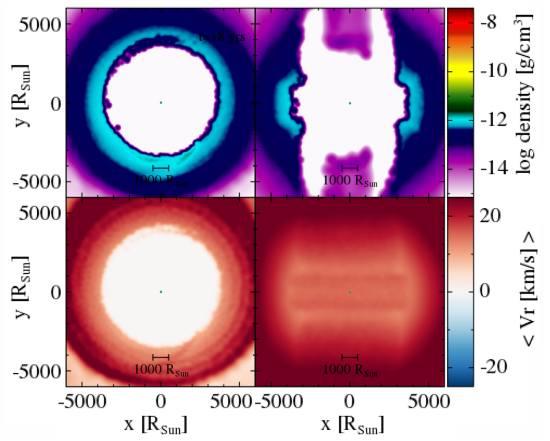

(d) CE end, L_2 particles.

Figure 4.5: Density and velocity slices for the $q = 0.68$, high resolution simulation. The top row of each box is the x-y plane density (top left) and the x-z plane density (top right), while the bottom row is the radial velocity with respect to the centre of mass in the same planes. The leftmost set of 8 panels depicts the simulation at the start of the in-spiral, and the rightmost set of 8 is at end of the CE as defined by the triangles in Figure 4.4. The top set of 8 panels displays all particles, and the bottom set of 8 panels shows only the particles outside of L_2 at the time of in-spiral.

L_2 in Figure 4.6. This same material also has lower associated velocities, and does not move to the same large radii seen in the bottom right quadrants of Figures 4.5 and 4.7.

In Figure 4.7 we show the same plot as in Figures 4.5 and 4.6, but this time for the $q = 0.85$ MESA EOS simulation. Most notably when comparing the bottom right plots of each, the L_2 material in the MESA EOS simulation has almost entirely evacuated the region of the plot - which is kept the same across each figure. It does so with much approximately

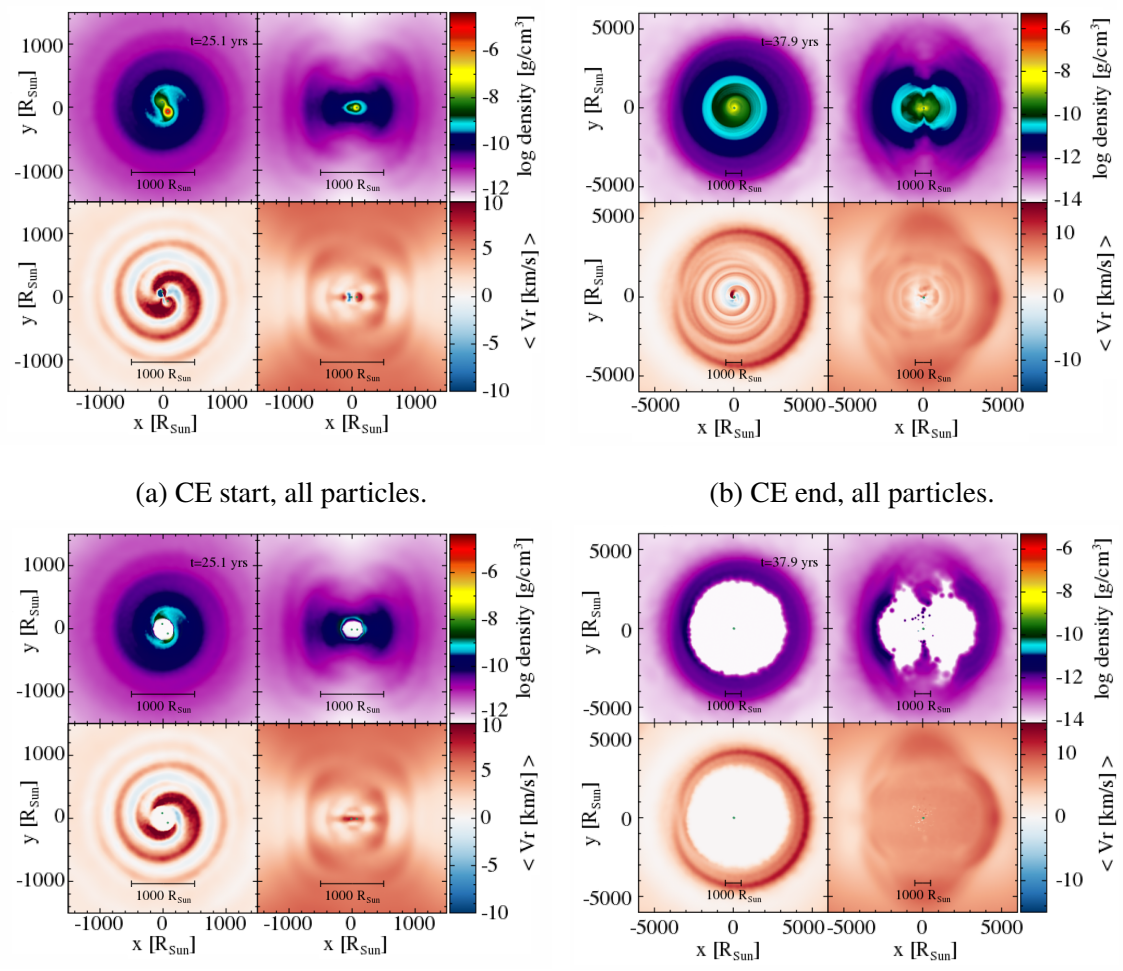

(a) CE start, all particles.

(b) CE end, all particles.

(c) CE start, L_2 particles.

(d) CE end, L_2 particles.

Figure 4.6: Similar to Figure 4.5, but for the high resolution $q = 0.85$ simulation.

double the radial velocity as the high resolution $q = 0.68$ simulation, and with a noticeable increase in the number of spiral shocks post-CE. In this MESA simulation, there is a much smaller chance that material will fall back onto the system, even when considering just the CE ejecta.

We note that in the post-CE L_2 panels (bottom right), in particular in Figures 4.5 and 4.6, is the interesting shape of the gas distribution in the x-z plane. We next determine whether this material ejected early on through L_2 is kinematically distinct from that ejected later during the in-spiral. If so, then as the in-spiral causes the bulk of the ejection (where by ejection we do not need the material to be unbound, just lifted), we might expect that this earlier ejecta would constrict and mould the CE ejection. The alternative is that the L_2 ejection does not remain kinematically distinct, and that the CE ejecta overwhelms and shapes the L_2 ejecta.

In order to investigate this we looked specifically at the velocities of each SPH particle

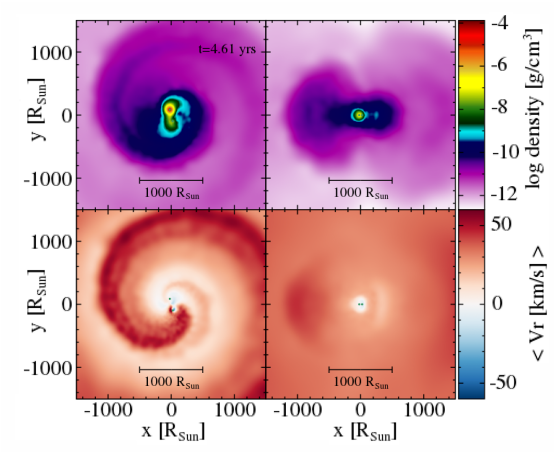

(a) CE start, all particles.

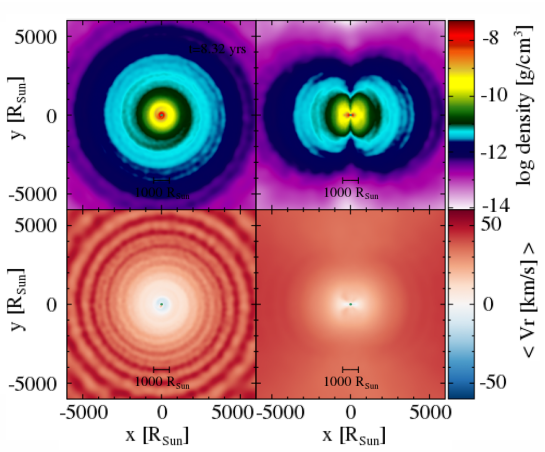

(b) CE end, all particles.

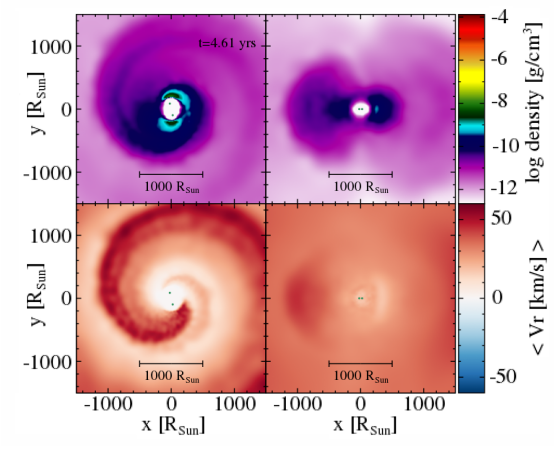

(c) CE start, L_2 particles.

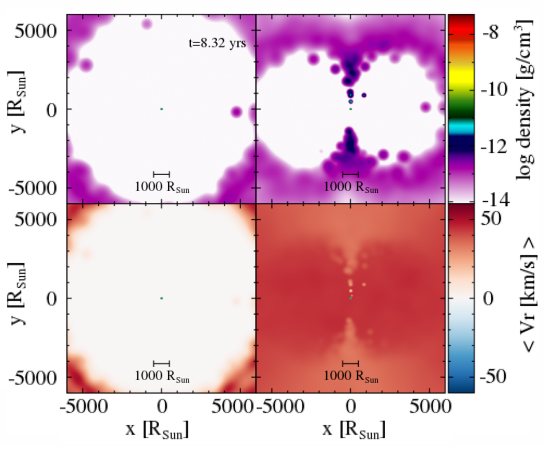

(d) CE end, L_2 particles.

Figure 4.7: Similar to Figure 4.5, but for the MESA EOS $q = 0.85$ simulation.

for these simulations as a function of distance from the centre of mass. These are plotted in Figure 4.8. The black line represents the escape velocity for the system as calculated by $v_{\rm esc} = \sqrt{\frac{2G(M_1+M_2)}{R}}$, where M_1 and M_2 are the original masses of the donor (including envelope) and the companion[1]. In these plots green dots are particles beyond L_2 at the time of the CE, and red dots are those within L_2 at the same time. Note that we have used velocity here, so as to compare directly to the system's escape velocity, as opposed to the rendered plots in Figures 4.5, 4.6, and 4.7 which used radial velocity instead.

In this way we can again confirm the findings of Table 4.2, for instance the high resolution $q = 0.85$ simulation has not unbound all of the L_2 material at the time of in-spiral, whereas

[1]In this way the black line is not the true escape velocity for each time step, but is instead the maximum possible escape velocity. Similarly calculating the lower bound by only using the masses of the point mass cores does not yield a meaningfully different result.

the MESA EOS simulation unbinds all of the L_2 material, including much of the CE ejecta. We also see that material ejected before the CE in each simulation has an approximately constant velocity, in that each particle shown in the spires of Figure 4.8 moves strictly horizontally once they have become unbound from the system. Those which are ejected first at the tip of the spire have the highest velocities. This behaviour is characteristic of homologous expansion, wherein velocity is typically proportional to radius, with the earliest ejecta moving the quickest. As time progresses in the simulations, this behaviour also does not change for the early particles seen in the left hand column of Figure 4.8. As such this material interacts very little, if at all, with any later ejecta since it simply stays so far ahead of the later CE material with their relatively smaller velocities. This is particularly true of the centre panels featuring the high resolution $q = 0.85$ simulation, where there is a much smaller interaction between the green and red particles at the time of the CE than there is for the $q = 0.68$ simulation seen in the top panels. For a more detailed look at the behaviour of these plots as a function of time, please find the movies we have created in Figure A.5.

As the movies show, material ejected just before the onset of the CE (the last green particles before the transition to red) experience an acceleration from what is ejected shortly after, during the on-set of the CE. That is to say, once the red particles of the CE begin to become unbound, they move diagonally upward in the plot, interacting with the green particles. In doing so they can greatly increase the velocity of the green particles, creating phenomena such as the more vertical, secondary spire in the $q = 0.68$ simulation. This implies that, at least at the boundary of the green and red particles, pre-CE material and CE material, are not kinematically distinct. It is worth noting that the particles are coloured according to where we have calculated L_2 to be at the time of the CE. This means there is very likely some green particles which should be red, and visa versa. We do not expect this to be a significant amount, however when talking about kinematic identity there is some room for overlap here. If we are correct in saying the L_2 material at the boundary of the CE does not retain its kinematic identity, than it is unlikely that it forms a mould that constrains the later CE ejecta, and instead is overwhelmed by it. The movies mentioned previously, particularly for the $q = 0.68$ simulation show just how considerable this overwhelming of the green L_2 material is by the red CE material.

Figure 4.8 also shows that with a MESA EOS, far more material is unbound throughout the simulation compared to that of the ideal EOS simulations. The inclusion of recombination

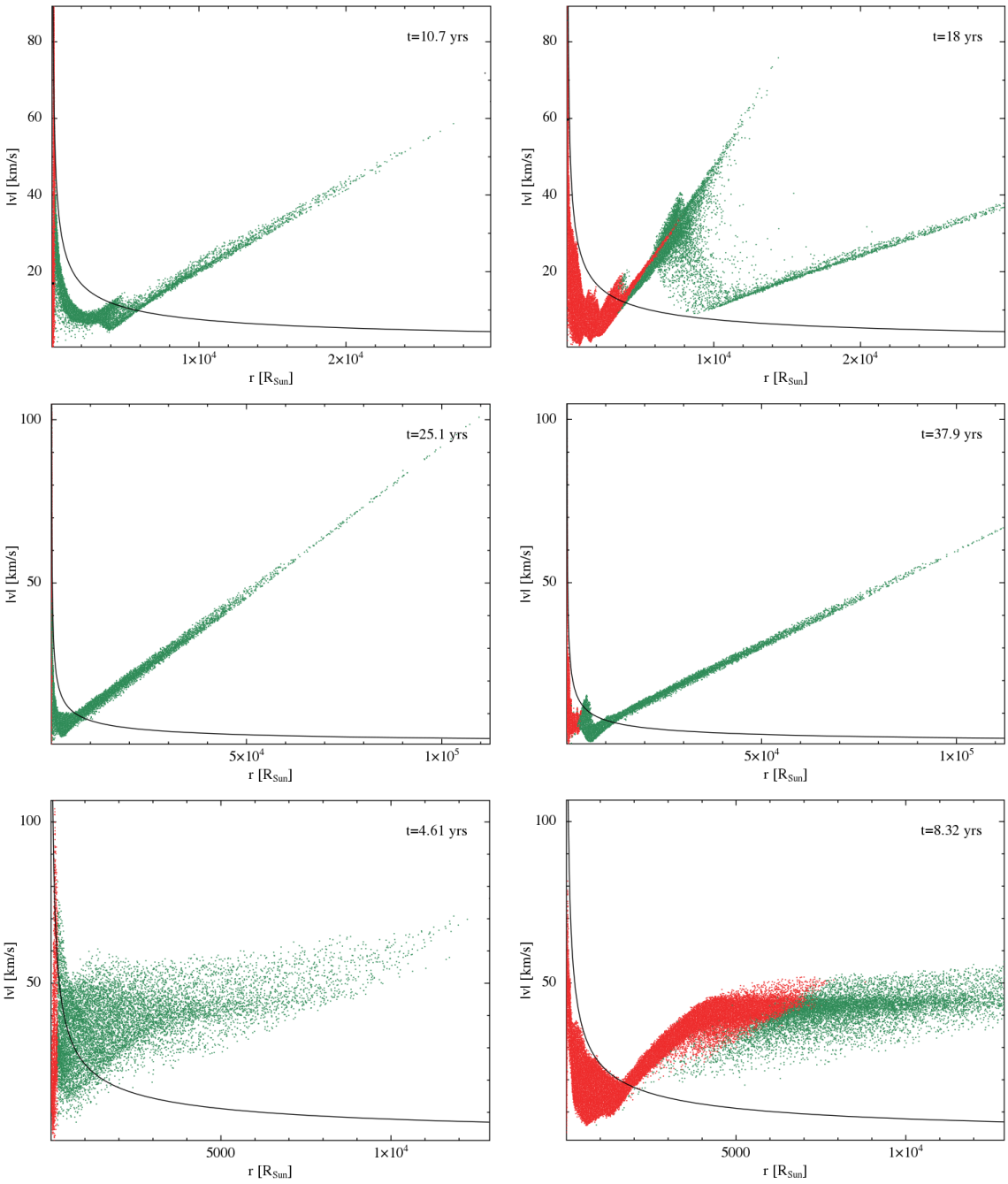

Figure 4.8: From top to bottom we plot the velocities as a function of radius from the centre of mass for q = 0.68(H), 0.85(H), 0.85(M) respectively. The left hand column is the start of the CE as defined in Chapter 3, and the right hand column is the end of the CE as defined earlier in this chapter. The green particles are those ejected through L_2 before the CE begins, and the red are those that come afterwards. The black line in each shows the escape velocity for the binary.

energy clearly has a significant impact on the amount of gas unbound from the system. The effect of recombination energy is well documented (Reichardt et al., 2020; Lau et al., 2022; Gonzalez-Bolivar et al., 2022) and the effect we see here is fully expected: as gas expands and adiabatically cools below ~10 000 K, it recombines and the delivered photons are thermalised immediately contributing their energy budget to the thermal energy of the gas and increasing the unbinding.

Comparing the high resolution simulations for $q = 0.68$ and $q = 0.85$ in Figure 4.8 shows there are also differences in the radii at which material becomes unbound for the ideal EOS. Higher q results in a prolonged period of early mass transfer, with ultimately more mass leaving the orbit of the binary, thus a weaker CE is experienced, with less mass ejected through it as a result. The radius at which material becomes unbound is approximately 4000 $R_\odot$ and 10 000 $R_\odot$ for $q = 0.68$ and $q = 0.85$ respectively. The behaviour of this ejecta is also different between these two simulations. For the higher q simulation, the CE does not significantly accelerate the L_2 material, leading to only a marginal increase in the unbinding, however the opposite is true for $q = 0.68$. In this lower q simulation the CE is a large source of unbinding, creating the top spire of material in the top right plot of Figure 4.8 as mentioned previously.

As is more clear in the movies, this secondary spire emerges due to material from the lower spire, at lower radii being accelerated upwards in the plot. The particles as seen here in between the two are generally in the process of moving upwards in the diagram to higher velocities as the bulk of the CE ejecta reach their location. Another smaller feature, noticeable mostly in the top left most panel, is the smaller linear striations in the early ejecta. We found these were caused by the orbital period, and the slight eccentricity of said orbit modulating matter ejection through L_2. By taking the difference in two particle locations along two different lines, and dividing their radial position by their velocity in fact gives a difference of roughly the orbital period of the system.

In this chapter we have shown that the pre-CE L_2 material does not retain its kinematic identity near the boundary of L_2 at the time of the CE; that is, where the green particles meet the red particles in Figure 4.8. The expulsion of material through L_2 during the early mass transfer phase prior to the CE does behave like a homologous expansion, with the velocity of each SPH particle being proportional to its radius from the centre of mass. Because of this, material that is ejected early, well before the CE onset, retains its kinematic identity

as it stays far ahead of the material that comes after it. Across all simulations, excluding the high resolution $q = 0.85$, over 90% of the mass ejected through L_2 before the onset of the CE ultimately becomes unbound by the CE's conclusion. This is likely because with a longer, more stable phase of early mass transfer, the higher resolution, higher q simulation experiences a weaker CE, and as such, accelerates and unbinds less of the pre-CE L_2 material when compared to its lower mass ratio counterpart. Another consequence of this longer phase of mass transfer seems to be that the final separations of such systems are wider than that of lower q systems too. This means lower q systems might be the most viable systems when attempting to generate final separations of less than 10 $R_\odot$, whereas higher q systems would be better candidates for wide separation binaries similar to that of so called 'Van Winkel objects' (van Winckel, 2003), which are typically post-AGB, wide separation binaries with circum-binary disks. Finally, we have also shown that high resolution simulations unbind less mass overall, however the $q = 0.68$ simulation unbound approximately only 5% more of its envelope than the $q = 0.85$ high resolution simulation. From this we can see when we consider any potential fallback onto our systems, resulting in future interactions, much of this mass will come not from the material ejected early on, but instead from the material ejected during the CE, with only minor differences depending on q value.

5

Post-CE Fall-back

In the previous chapter we investigated the mass lost early on from the binary through the outer Lagrange point L_2, examining the kinematics of such material, and where it differs to that lost during the CE. Since the final separations of our simulations are too large to reproduce close binary observations, we now turn our attention to methods to shrink the binary separation further. Kuruwita et al. (2016) previously has shown that fall-back material is capable of shrinking the orbit in their simulations, although without an additional energy source, the envelope could not be ejected implying that a series of fall-back episodes would invariably lead to a merger, contrary to the fact that we observe compact binaries. In this chapter we seek to explore further the idea that gas fall-back could lead to the right amount of shrinkage.

5.1 The Fall-back Radius

Before we look at the work the fall-back mass can do on the system to shrink the orbit, we must first assess whether or not the angular momentum of the ejecta is such that it is capable of falling back far enough to influence the orbit in the first place. We do this similarly to Tocknell et al. (2014), by considering a ballistic trajectory with conservation of energy and angular momentum as our argument. First we begin by noting that the z-component of our fall-back angular momentum can be written as:

$$J_z = mvr, \tag{5.1}$$

where m is the mass element of an infalling test mass, with velocity v, at some radius from the centre of mass, r. Then by the conservation of angular momentum we have that $J_i = J_f$. Hence we obtain the following expression:

$$mv_i r_i = mv_f r_f, \tag{5.2}$$

where we will take r_i to be the maximum radius of bound material at the end of the CE, that is, the furthest mass m that could reasonably be expected to return. Then r_f is the radius that the material could reasonably fall back to given its initial and final velocity, v_i and v_f respectively.

We can also write the energy of our infalling test mass system as:

$$E = \frac{1}{2}mv^2 - \frac{GMm}{r}, \tag{5.3}$$

where r is the radius from the centre of mass, v is the particle's velocity, G is the gravitational constant, and M is the mass of the central binary. This energy must also be conserved between the final and initial state of the system, and as such we obtain:

$$\frac{1}{2}v_i^2 - \frac{GM}{r_i} = \frac{1}{2}v_f^2 - \frac{GM}{r_f}, \tag{5.4}$$

where the variables have the same meaning as that used in Equation 5.2, and we have cancelled the m factors for the specific energy. Both r_i and v_i are measured from each of our simulations. As mentioned, the initial radius of the fall-back material is approximately that of the furthest particle that is still bound at the end of the CE in-spiral. The initial velocity we find in the same way proposed by Tocknell et al. (2014), who first found the specific angular

momentum of the infalling material by dividing the total bound angular momentum by the total bound mass, such that $\frac{J_b}{M_b} = v_i r_i$. Dividing both sides by the initial radius then yields the velocity of the bound material at said radius, which is approximately equivalent to that taken from our simulations. Now we have two equations in Equation 5.2 and Equation 5.4, with two unknowns, being r_f and v_f, our fall-back radius and velocity respectively. Rearranging Equation 5.2 for v_f yields:

$$v_f = \frac{v_i r_i}{r_f}, \tag{5.5}$$

which can then be substituted into Equation 5.4. Rearranging the resulting expression gives us a quadratic expression for the fall-back radius:

$$\left(v_i^2 - \frac{2GM}{r_i}\right) r_f^2 + 2GMr_f - v_i^2 r_i^2 = 0. \tag{5.6}$$

Note that the coefficient of the quadratic term must be negative here, as $v_i^2 < 2GM/r_i$, otherwise the initial velocity would by definition be greater than escape speed and the material would not fall-back onto the system. As we have chosen to take only bound material, it is true of our simulations that this inequality holds. Solving this quadratic equation can be done analytically, and simplifies nicely by recognising there is a difference of squares in the determinant:

$$r_f = \frac{-GMr_i \pm r_i\sqrt{G^2M^2 + v_i^4 r_i^2 - 2GMv_i^2 r_i}}{2v_i^2 r_i - 2GM}. \tag{5.7}$$

This yields the two solutions as given in Equation 5.8:

$$\begin{aligned} r_{f,1} &= r_i \text{and} \\ r_{f,2} &= \frac{v_i^2 r_i^2}{2GM - r_i v_i^2}. \end{aligned} \tag{5.8}$$

one of the roots is trivial, $r_{f,1} = r_i$, in that it implies there is no movement in the distribution of the fall-back material; thus we only consider the second root.

Here we stress that these calculations are done assuming the distribution of material, and thus the moment of inertia are equivalent between the initial and final states of the system, i.e., if the system begins as a disk or a ring, it ends as a disk or a ring. Below we carry out the same type of calculation, but for a changing morphology of fall-back material. For example

a ring configuration could end as a disk configuration. In this case it is more useful to write our z-component of angular momentum as:

$$J_z = I\omega, \tag{5.9}$$

where I is the moment of inertia, which for a ring is $I_{\text{ring}} = Mr^2$, while for a disk it is $I_{\text{disk}} = \frac{1}{2}Mr^2$. We note that the radius in these expressions is not the same: in the case of the ring the radius is the one-value radius of the thing ring, while for the disk it is the outer radius of the disk. Here ω is the angular velocity given by $\frac{v}{r}$, where r is the distance from the centre of mass, v is the velocity at said radius, and M is the mass of the distribution of fall-back material. First we investigate the case in which the distribution of mass *begins as a disk and falls back into a ring*. Again we assume conservation of angular momentum such that $J_i = J_f$, giving the expression:

$$\frac{1}{2}Mr_i^2\omega_i = Mr_f^2\omega_f. \tag{5.10}$$

We can simplify this expression, and rearrange to solve it for v_f as we did previously. This gives $v_f = \frac{r_i v_i}{2r_f}$. In the same manner as before we can substitute this new expression into Equation 5.4 to obtain another quadratic in r_f:

$$\left(v_i^2 - \frac{2GM}{r_i}\right) r_f^2 + 2GMr_f - \frac{1}{4}v_i^2 r_i^2 = 0. \tag{5.11}$$

Notice the only term that has changed by considering a change in geometry from a disk to a ring is the third term, now featuring a factor of $\frac{1}{4}$. This small change alters the equation enough that there are no longer two roots that can be simplified and expressed as easily as in Equation 5.8. Instead to find our fall-back radii for the ring, we must solve:

$$r_f = \frac{-2GMr_i \pm r_i\sqrt{4G^2M^2 + vi^4 r_i^2 - 2GMv_i^2 r_i}}{2v_i^2 r_i - 4GM}. \tag{5.12}$$

For the case instead where the distribution *starts as a ring and ends as a disk*, we find a similar expression, except that the third term is now multiplied by a factor of 4, instead of $\frac{1}{4}$:

$$\left(v_i^2 - \frac{2GM}{r_i}\right) r_f^2 + 2GMr_f - 4v_i^2 r_i^2 = 0 \tag{5.13}$$

. This alters the equation such that the same simplifications used previously in Equation 5.8 also do not work here and we must again use the quadratic formula to numerically solve:

$$r_{\rm f} = \frac{-GMr_{\rm i} \pm r_{\rm i}\sqrt{G^2M^2 + 4v{\rm i}^4 r_{\rm i}^2 - 8GMv_{\rm i}^2 r_{\rm i}}}{v_{\rm i}^2 r_{\rm i} - 2GM}. \tag{5.14}$$

However, since the coefficients of $r_{\rm f}$ have not changed between Equations 5.6, 5.11, and 5.13, despite the evolution of the morphology, we need only compare the constant term of the quadratic in each of these three equations. We find that the effect of geometry on the fall-back radii is that in the disk-to-ring case, where the constant term is divided by 4, the fall-back radii also shrink by a factor of approximately 4. In the ring-to-disk case where the constant term is multiplied by 4, we find that the fall-back radii thus increased by approximately a factor of 4. In each of these cases we have chosen the smaller of the two roots for our fall-back radii, as our goal is to consider the scenario in which a further interaction is possible.

Regarding the larger of the two roots, we found that there only happens to be an insignificant change in this solution, i.e, they do not experience the division or multiplication by 4 that the other roots do, and instead seem to imply little to no bulk movement, akin to the trivial solution in Equation 5.8.

To compare more formally these three different scenarios we present in Table 5.1 the post-CE separations for each simulation, alongside the fall-back radii given by each assumption about the shape of the distribution. It is important to note that here our final separation values $a_{\rm f}$ differ from that seen in Table 3.1. The previous table noted the separation as given by the method outlined in Reichardt et al. (2019), whereas here we have chosen the final separation to be that coinciding with the moment before the artificial unbinding takes place (the triangles in Figure 4.4).

Note that when considering the size of these distributions, we consider the radius, in the case of a disk, to be the outermost radius, as we began with an $r_{\rm i}$ (and accompanying $v_{\rm i}$) that was chosen to be at the outer edge of the bound material. In the case of the ring we consider its radius to again be the outer edge, while assuming it is generally narrow in width and concentrated largely around this radius. We also stress here that when we consider the fall-back disk, we acknowledge this 'disk' actually has a hole in it that is of the order of the binary's orbit. We have assumed this can be approximated as a disk because the outer radius of the material falling back is significantly larger than the radius of the hole in the middle around the binary.

It is important to remember that the parameter $a_{\rm f}$ in Table 5.1 is *not* the radius of the binary's orbit around the centre of mass. It is the separation between the two stars, whereas

Sim. q(Res)	$a_{\rm f}$ ($R_\odot$)	$a_{1,\rm f}$ ($R_\odot$)	$a_{2,\rm f}$ ($R_\odot$)	$r_{\rm i=f}$ ($R_\odot$)	$r_{\rm d\to r}$ ($R_\odot$)	$r_{\rm r\to d}$ ($R_\odot$)
0.68(L)	24	11	13	21	5	85
0.68(H)	19	8	11	34	9	141
0.85(L)	40	20	20	36	9	153
0.85(M)	38	21	17	0	0	0
0.85(H)	28	13	15	49	12	198
1.00(L)	60	32	28	35	9	144

Table 5.1: Fall-back radii of material depending on the evolution of the distribution. Here $a_{\rm f}$ is the separation of the two stars at the end of the CE, and $a_{1,\rm f}$, and $a_{2,\rm f}$ are the distances from the centre of mass of the donor and accretor respectively. The final three columns summarise the expected fall-back radii depending on the evolution of the material, that is, no change in the moment of inertia (Equation 5.6), a change from a disk to a ring (Equation 5.11), and finally a change from a ring into a disk (Equation 5.13).

the fall-back radii calculated in the same table are the distances from the centre of mass. Therefore a value of $R < a_{\rm f}$ does not necessarily mean the binary will interact with the material if R is close to $a_{\rm f}$. As such we have included the additional columns to denote the distance of each star from the centre of mass to make the possibility of interaction more obvious.

Regardless of how the fall-back material does or does not change its distribution, for the low resolution simulations the fall-back radii are somewhat smaller. This is because lower resolution simulations routinely unbind more mass and angular momentum, leaving the material that is still bound with a lower total angular momentum budget. Gas unbinding also occurs at lower radii for lower resolution simulations, compared to their higher resolution counterparts. The MESA EOS simulation is the most extreme example. By unbinding significantly more of the envelope at a much lower radius, whatever bound gas is left has a significantly lower angular momentum: almost two orders of magnitude less than the other simulations. What little material is still bound by the end of the CE, then exists much closer to the binary, and with much less angular momentum, making a total fall-back of material onto the binary comparatively very easy, as seen by the negligibly small fall-back radii in Table 5.1.

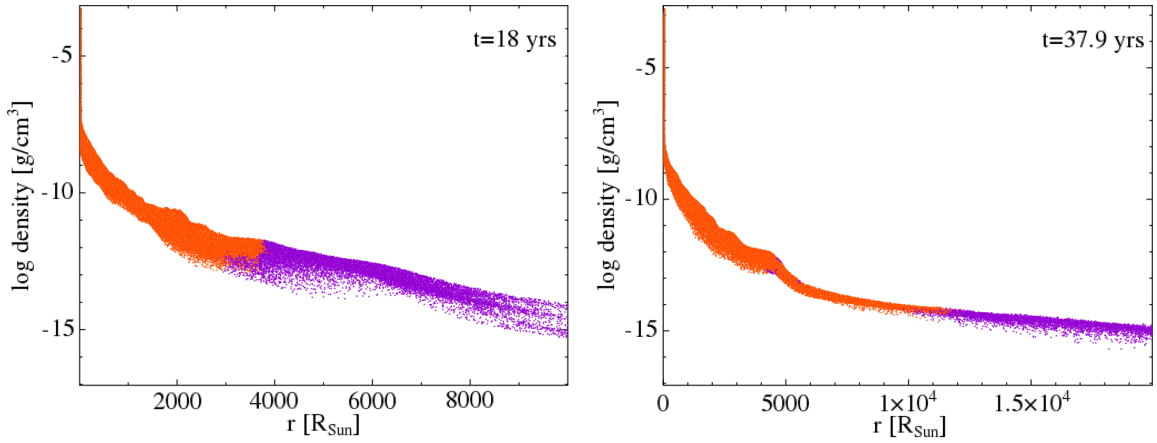

Figure 5.1: Particle density vs. distance from the centre of mass for simulations 0.68(H) (left panel) and 0.85(H) (right panel) taken at the end of the CE, at the same time as the end of the CE denoted by the triangles in Figure 4.4. Purple particles have velocities above local escape speed, while orange particles are below escape speed. Clearly we see no distinct ring features at this time, and thus our starting distribution for material begins most well approximated by a disk.

We find that only a lack of change in the distribution or a change between a disk and a ring could lead to significant fall-back of mass onto the orbiting binary. We argue these two configurations could be realistic for the fall-back distribution. The former makes no assumption of a change in geometry. The latter seems plausible as demonstrated in Figure 5.1: the distribution of bound material around the binary has little to no ring-like features, and shows that while the distribution is not uniform, it is much more akin to that of a disk. As such this scenario of a starting ring changing to a disk is much less physical.

It is also important to note that the radii listed in Table 5.1 are for the farthest bound material (for the case of a disk, while for a ring they are the only radius). This reassures us that when these radii are similar to the distance of the farthest companion to the centre of mass, all the fall-back gas can likely interact with the binary.

5.2 The Fall-back Mass

If the envelope is not ejected during the CE, the system will eventually end in a merger (Kuruwita et al., 2016). Thus in order for a binary to survive the CE interaction, at some point, whether it be during the first CE or any subsequent interactions, the entire envelope

must be ejected[1]. Given that we have a merger with a sufficient amount of mass remaining, and a surviving binary with none, there must then exist a range of "left-over" envelope masses for which there is enough fall-back envelope mass in the system to shrink the orbit of the binary, but not merge the two cores. As we have demonstrated previously, it is possible for the mass in the post-CE environment to fall back to such a radius that a further interaction is likely. This fall-back mass will act to shrink the orbit by doing work on on the binary through momentum exchange, similar to that which caused the in-spiral during the first CE to begin with.

Here we will perform a first order approximation of the work done on the binary by this fall-back material to assess the orbital shrinkage as a function of the amount of fall-back material. We assume that 100% of the fall-back mass will be swept by the companion over the span of a single orbit, and that the ring this material creates is moving with a negligible velocity compared to that of the orbit. We write the companion's velocity with respect to the primary as:

$$v = \sqrt{\frac{G\mu}{a}}, \tag{5.15}$$

where G is the gravitational constant, and a is the binary separation, and μ is the reduced mass of the binary. From Kepler's third law we can also write the period, T, of the system as:

$$T = 2\pi\sqrt{\frac{a^3}{GM}}, \tag{5.16}$$

where $M = M_1 + M_2$. Thus we obtain the equation for the work done on the companion over a single orbit by an amount of fall-back mass, M_f:

$$W = 2\pi a \frac{M_\mathrm{f} v}{T}. \tag{5.17}$$

Here we have assumed that the momentum of a fall-back ring, moving with the same orbital velocity with respect to the companion, is fully accreted by said companion over an orbital period, thus creating a force that does work over one orbital path. Note that we have also assumed this force is constant for simplicity.

In performing this calculation, we have assumed the most ideal case possible for how much work an amount of fall-back material can reasonably do on a binary to shrink its orbit. In order to determine whether this work is sufficient to shrink the orbit to observed values,

[1]By entire envelope we mean the amount of envelope mass that can remain on the star and still induce a decrease in radius, depends on the core mass but is of the order of 10^{-2} $\mathrm{M}_\odot$.

we compare the work done to the change in orbital energy it would cause, given previously by Equation 1.9. Here we modify this equation slightly to include the fall-back mass that has accreted onto the companion by the end of the orbital reduction:

$$\Delta E_{\rm orb} = G\frac{M_{1,\rm c}M_2}{2a_{\rm i}} - G\frac{M_{1,\rm c}(M_2+M_{\rm f})}{2a_{\rm f}}, \tag{5.18}$$

where $M_{\rm f}$ is again the fall-back mass the companion accretes, and $M_{1,\rm c}$ is the core mass of the donor. M_2 is the mass of the companion, and $a_{\rm i}$ and $a_{\rm f}$ are the initial and final separations before and after the orbital reduction, respectively.

We then study the amount of possible orbital reduction as a function of $M_{\rm f}$, the amount of fall-back mass, and $a_{\rm i}$, the separation of the binary at the end of the CE. In order to estimate the amount of mass that will fall-back onto our binary systems, we consider two different methods. The first, which should set an approximate lower limit, is to consider only the mass that has a negative radial velocity at the end of the CE. The other method, which gives an upper limit for fall-back mass, is to assume there is no further unbinding of material after the CE (recall the point before any artificial unbinding occurs post-CE is how we have defined the CE end), and thus, whatever is bound at that point will stay bound, regardless of the motion of the material, and must therefore fall back according to our previous calculations of fall-back radius.

In Figure 5.2 we examine the properties of the mass that has a negative radial velocity. The top plot in each simulation panel, at the end of the CE (magenta triangle), gives us an estimate of how much mass we can expect to return to the system by assuming that all the gas with negative radial velocity will fall back. The middle plot then gives us an estimate of the average velocity of this mass, while the bottom plot gives the angular momentum.

Figure 5.2 shows that with higher q, we generally have less mass with a negative radial velocity. For instance the simulation with $q = 0.85$ (H) has about half the mass with a negative radial velocity than the $q = 0.68$ (H) simulation. This can also be seen when comparing the top right boxes in Figures 4.5 and 4.6. In those plots we can see this might be due to stronger spiral shocks created by the binary with a larger companion, reducing the ability for the fall-back material (as defined in this case) to accumulate. Ejected material also leaves the binary with greater velocities in higher q simulations, as previously shown in Figure 4.8. Similarly this is also generally true of lower resolution simulations. Interestingly the high resolution $q = 0.68$ simulation is the only plot featured here to experience a large negative

Sim. q(Res.)	$a_{\rm i}$ ($R_\odot$)	$M_{\rm rv}$ /0.49($M_\odot$)	$M_{\rm b}$ /0.49($M_\odot$)
0.68(L)	24.2	0.05	0.34
0.68(H)	19.4	0.13	0.44
0.85(L)	40.4	0.07	0.39
0.85(M)	38.3	0.02	0.24
0.85(H)	27.7	0.07	0.46
1.00(L)	60.3	0.03	0.37

Table 5.2: Summary of the fall-back masses for consideration in the calculation of orbital shrinkage. Here we have denoted the final separation of the binary as $a_{\rm i}$, as it will now be used as the initial separation before any further shrinkage. $M_{\rm rv}$ is the mass counted with negative radial velocity at the end of the CE, while $M_{\rm b}$ is the mass of the bound envelope by the end of the CE.

spike in radial velocity around the time of the CE. This in turn might be the reason why this simulation in particular has been able to hold onto more mass with negative radial velocities than any other. The lower resolution simulations, including the MESA EOS simulation also exhibit a large drop off in fall-back mass after the end of the CE as marked by the triangles. This is again due to the artificial unbinding that occurs at late stages of the simulation as mentioned previously. This drop off, however, is not instant, as many of these simulations still experience a marginal increase in the amount of fall-back mass before the drop off, which seems to occur most prominently in the higher q, lower resolution simulations, namely $q = 0.85$, and $q = 1.00$. We also find these latter two simulations experience a spike in fall-back mass and angular momentum around the time the in-spiral timescale is at its fastest (this is most prominent in the $q = 1.00$ simulation), which we consider to be a resolution dependent characteristic.

We have summarised the two methods used here to calculated the amount of fall-back mass in Table 5.2. Between the two there is up to an order of magnitude difference. The final separations of the simulations, called $a_{\rm i}$ for the benefit of the fall-back calculation, represent the initial separations from which the orbital shrinkage will begin. To visualise the comparison between work done on the companion, and the change in orbital energy as the orbital separation decreases, we will consider a range of fall-back masses up to $0.49 M_\odot$,

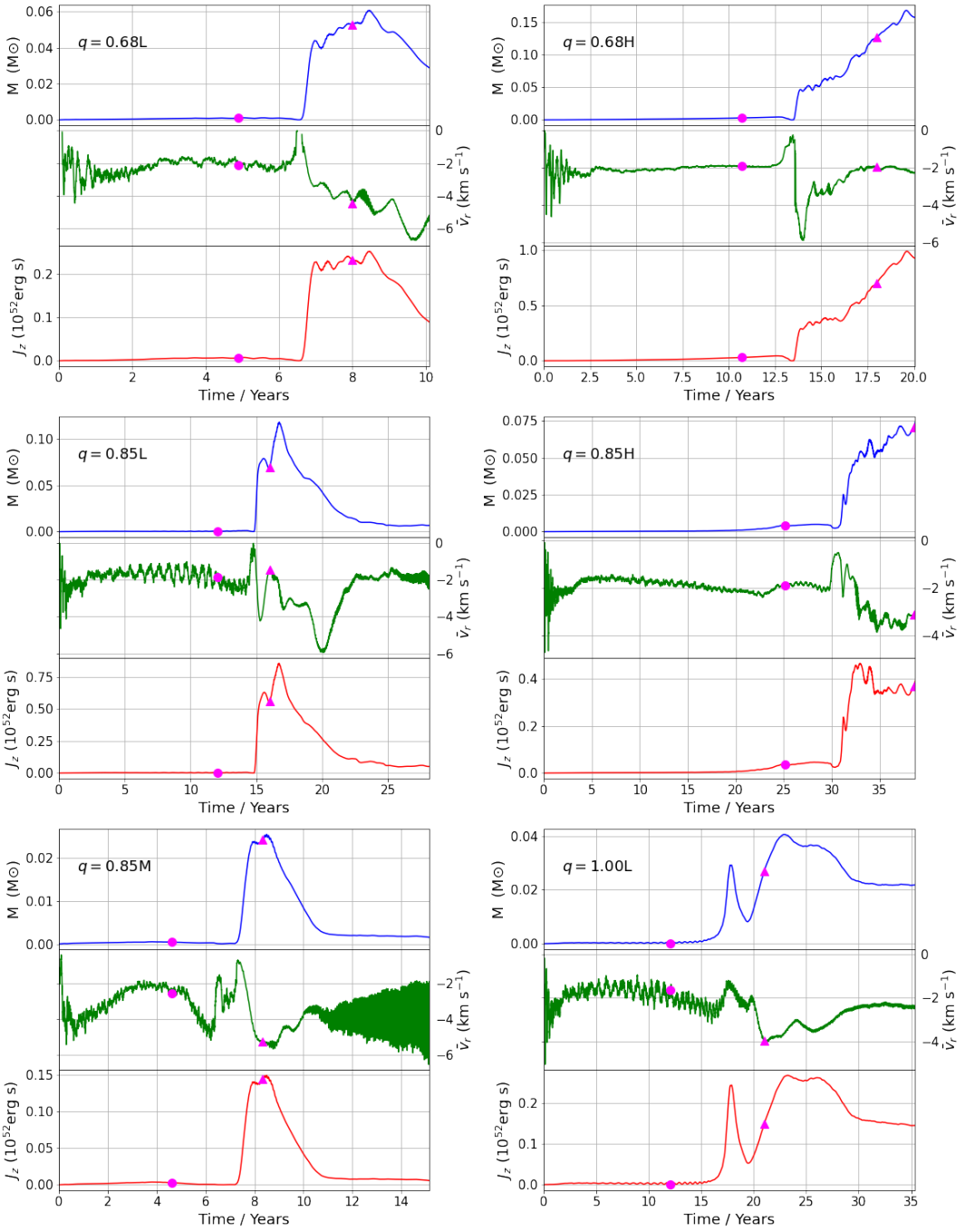

Figure 5.2: Properties of envelope gas with negative radial velocity, assumed to fall back for the simulations that experienced a CE. For each simulation, the top panel shows the mass with negative radial velocity, the middle panel shows the average radial velocity of that gas, and the bottom panel displays the angular momentum of the same gas. The magenta circles and triangles correspond to the beginning and end of the CE, the same points used in Figure 4.4.

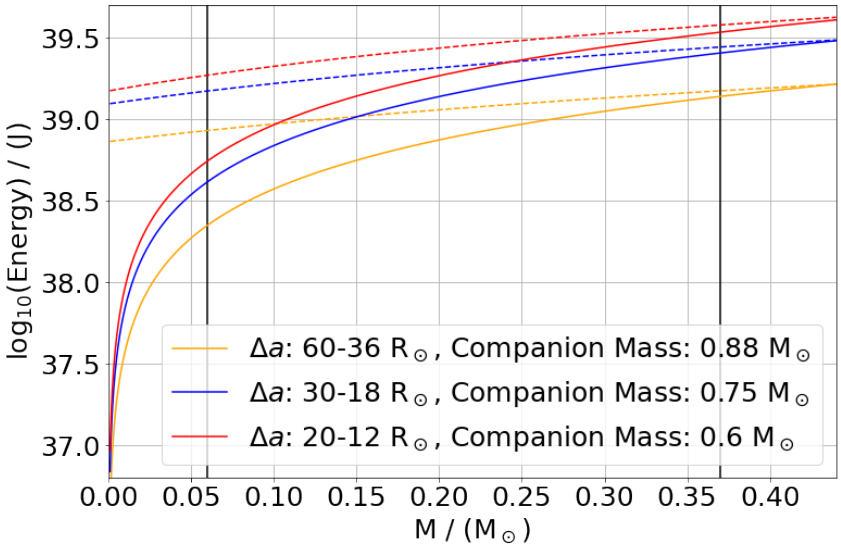

Figure 5.3: Change in orbital energy (dashed lines) between the indicated separations (Δa), and work done on the companion by the fall-back mass (solid lines), as a function of fall-back mass from 0.01 to 0.49 $M_\odot$ (where the high end of the range is the total mass of the donor's envelope and thus the maximum possible amount of fall-back available). The left most black line represents the average fall-back mass as given by material with negative radial velocity, whereas the right most black line represents the average amount of fall-back mass as given by what remains bound at the end of the CE.

the total available mass of the envelope. We plot this comparison for a range of separations, for different amounts of separation decrease, and for different companion masses generally derived from Table 5.2 in Figure 5.3.

This plot uses the approximate final (here initial) separations for each value of q in Table 5.2, along with the appropriate companion mass. The shrinkages are chosen such that the change in orbital energy and the work done on the companion meet only when we have 100% of the envelope returning to the system as fall-back material. As we have already shown, there is a range of unbinding across our simulations, so this assumption of a total fall-back is not physical. In fact, as we have already stated, a total envelope fallback must result in the merging of our system. In assuming this total envelope fall-back however, we aim to simplify the process of comparing our different ranges of orbital reduction. The aim here is not strictly to find how much the orbital will shrink, but instead to illustrate that with a greater amount of fall-back mass, the amount of work that can be done to shrink the orbit is

also greater; a conclusion which was also demonstrated previously in the work of Kuruwita et al. (2016). We also find that in our simulations, masses of greater than approximately 0.1 $M_\odot$ are required as a minimum to start making a noticeable difference in bringing these two energies close together. As we see from the two black lines in Figure 5.3, if we are to conclude that only material with a negative radial velocity is to fall-back, orbital reduction is much less likely than if we consider the alternative that fall-back mass is whatever remains bound by the conclusion of the CE.

The limitations of the calculations we have put forth should be obvious here, as our equations do not reproduce the expected merger with the fall-back of the entire envelope. This comes from the slight mismatch between comparing the change in orbital energy to the work done by the fall-back mass as a source for said change. As we have noted in the literature, the alpha formalism (Equation 1.10) compares this same change in orbital energy with the binding energy of the envelope itself. What we have issue with here is reconciling the differences in energy lost to unbinding with the ejection of particles, versus energy lost to collisions, with the accretion of particles. We thus move forward carefully, with the knowledge of our limitations in reproducing reality, as our calculations for work do not intrinsically contain the condition that a merger should occur with a sufficient M_f, and consider only the work done by a given amount of mass in an idealised scenario.

In each of the three cases shown in Figure 5.3 the ratio of the final separation to initial separation is a constant (3/5). This implies the smallest possible separation obtainable through fall back of material for these simulations would be approximately 60% of whatever the original post-CE orbital separation was. We can investigate this phenomenon in greater detail by again equating the work in Equation 5.17 to the change in orbital energy in Equation 5.2, which yields:

$$\frac{a_\mathrm{f}}{a_\mathrm{i}} = \frac{M_1(M_2 + M_\mathrm{f})}{2M_\mathrm{f}\sqrt{M_1 M_2} + M_1 M_2}. \tag{5.19}$$

Next we assume the same conditions as in Figure 5.3, i.e. that $M_1 = 0.39\ \mathrm{M}_\odot$ (the core mass), and $M_\mathrm{f} = 0.49\ \mathrm{M}_\odot$ (total envelope fall-back). We plot this ratio of separations as a function of the companion mass in Figure 5.4. In doing so we find that if the companion to our donor is of lower mass, the final separations post-shrinkage grow to approximately 70% of the initial separation, whereas with larger companion masses, such as those in our simulations we find smaller separations, of less than or equal to 60% of the initial separation.

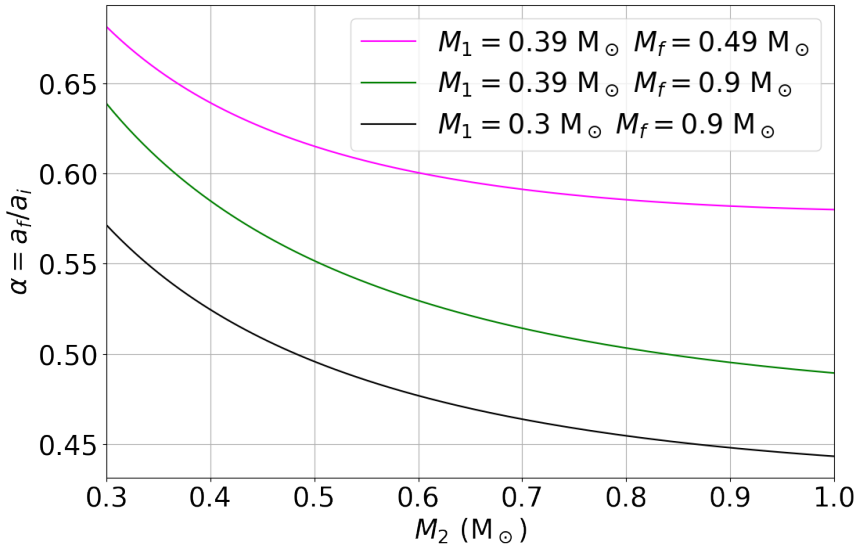

Figure 5.4: The ratio of final separation to the initial separation of the system after the CE as a function of companion mass. As such the magenta line shows how much smaller than the initial separation the post-shrinkage separation can be for the parameters in our simulation. The green line uses the same parameters, but with an increased envelope mass, to investigate how the shrinkage would change with more fall-back mass. Similarly the black line has the same increased envelope mass with a decreased donor core. We assume 100% envelope fall-back, and set the work done on the companion equal to the change in orbital energy between the two separations.

The green line in Figure 5.4 represents an arbitrary increase in only the envelope mass of the primary. If we take the companion mass to be approximately 0.85 $M_\odot$, which would allow for a shrinkage of 50% (i.e, to go from 10 $R_\odot$ to 5 $R_\odot$), then this hypothetical system would have a mass ratio of $q = 0.66$. If we do the same for the black line, choosing now the companion to be 0.48 $M_\odot$for the same factor in orbital reduction, then the resulting system would have a mass ratio of $q = 0.4$. Again we stress that in reality, with sufficient envelope fallback, the system must conclude in a merger, however what this shows is that when it comes to post-CE orbital shrinkage, the amount of available envelope material is crucial, and that the largest shrinkages in these circumstances are possible with lower q systems.

Similar conclusions to this were also made previously by Iaconi et al. (2018), who used the same primary (a 0.88 $M_\odot$ red giant) as our simulations, with a wider range of companion masses (0.1 $M_\odot$ to 0.9 $M_\odot$). Importantly they also kept the 0.39 $M_\odot$primary core constant

when they performed the same simulations with an increased envelope mass, creating a primary that in total was 2.0 $M_{\odot}$. They found final separations of these systems with larger primaries were well under 10 $R_{\odot}$, and with companion masses of up to 0.6 $M_{\odot}$ could potentially end in mergers. This represents a scenario in which the envelope is so massive to the point it cannot be lifted enough to allow for post-CE shrinkage, this more bound envelope will thus have a much greater chance of causing a merger due to inciting a stronger initial CE interaction.

If our goal is to reproduce observed binary separations of the order 5 $R_{\odot}$, then it seems from Table 5.2 and Figure 5.3 that this is perhaps only possible with lower q systems. Our investigation into the matter with Figure 5.4 seems to confirm that these low q systems are best suited for producing close binary observations. Lower q systems already create lower final separations with more ease than their higher q counterparts, and similarly also produce more fall-back mass by both measures (mass with a negative radial velocity, and total bound mass) at higher resolution. Hence we are best set to produce these low final separations in SPH simulations by increasing the resolution: thereby decreasing the binary separation; decreasing q: so as to further shrink the separation, and finally, increasing the mass of the donor's envelope (up to a point, as demonstrated by Iaconi et al. (2018)): such that we may maximise available fall-back to perform the work required. With these parameters in check it may then be possible to resolve the issue of reproducing small final separations.

6

Summary

We have sought to investigate the relationship between early mass transfer during RLOF, and how this affects the subsequent CE interaction. We have created 8 simulations with the SPH code PHANTOM (Price et al., 2018) using both lower and higher resolution, along with mass ratios of $q \equiv \frac{M_2}{M_1} = 0.68, 0.85, 1.00$, and 1.50. The primary donor star in our simulations is a 0.88 $M_\odot$, 90 $R_\odot$ red giant, used previously by Passy et al. (2012), Iaconi et al. (2017a); Iaconi & De Marco (2019), and more recently by Reichardt et al. (2019, 2020). The companion is a point mass particle whose mass we have varied across simulations to construct the different mass ratios. We have also included a single tabulated MESA EOS simulation with $q = 0.85$, to compare to the rest of the simulations with an ideal EOS. We have done this to study the characteristics of this early mass transfer across various systems, while also observing the effects of resolution and EOS.

6.1 Conclusions

The reason for studying the change in the strength of the CE due to variations in early mass transfer, is that we would like to explain how we are able to observe post-CE binary separations that are either extremely small, or, surprisingly, quite large: observations show that binaries can survive the CE with separations on the order of 5-10 $R_\odot$, as well as separations as large as 100 $R_\odot$. The latter values are the lower limit of the separation of post-AGB binaries (van Winckel, 2003), which, have a host of characteristics all of which suggest that these systems have in fact gone through some kind of weaker CE interaction, for instance the radii of the AGB star progenitors are large enough (200-600 $R_\odot$) that a separation of 100 $R_\odot$ necessitates some kind of interaction. By studying how early mass transfer changes with mass ratio, and how this affects the resulting CE, we hope to demonstrate how the early stages of the interaction can be crucial to producing a full range of final separations, both large and small. We also are interested in determining how the stages immediately following the CE in-spiral may additionally affect the final separation.

In Chapter 3 we started by defining the start of the CE in-spiral using a new method: a geometric criterion, based on the average slope of the separation versus time curve between the start of the simulation and the point of maximum in-spiral. This method generated suitable points for all of our simulations that experienced a CE, and is comparable to the method used by Reichardt et al. (2019), wherein a fraction of the minimum in-spiral timescale is chosen to define the start and end of the in-spiral. The method used by Reichardt et al. (2019) has difficulty finding a good point of initial in-spiral for simulations with gentle in-spiral slopes and more unique curves, and as such we opted to try an alternative that succeeded in these cases. We found, however, that our method, while suitable for the work in this thesis, might fail for simulations that experience a much longer phase of early mass transfer, by giving a start of the in-spiral point that appears to be too early.

We have also shown that the equation for mass transfer, used previously in MacLeod et al. (2018a) generally does an excellent job at predicting the mass transferring behaviour of our simulations, showing our analytical expressions and numerical approximations are in agreement. This equation is in fact much better than the one used by Reichardt et al. (2019). Most importantly we have shown that as the mass ratio, q, increases to unity, the rate of mass transfer drops by approximately an order of magnitude, but with a concomitant increase in the duration of the pre-CE mass transfer phase. We note that although the rate of transfer

has dropped and the time of transfer has increased, the two changes do not compensate each other. The higher q simulations transfer more total mass than their lower q counterparts by the beginning of the CE. This indicates a trend towards more stable rate of mass transfer for higher q, leading to a weaker CE interaction, as the companion is able to remove more of the envelope before the CE and does not plunge as deeply into the donor. This results in a larger final separation. The stability of this mass transfer also greatly increases with higher resolution for each simulation. For both high resolution and high q, namely in the $q = 1.00$ simulation, we did not observe a CE occur at all, though this is also true of our lower resolution $q = 1.50$ simulation, indicating q is a more important parameter than resolution when discussing the stability of pre-CE mass transfer.

The simulation carried out with a MESA EOS (at low resolution) displays a much shortened pre-CE phase. This may be due to the star being more unstable and somewhat expanding at the start of the simulation, something that would tend to hasten the interaction.

In Chapter 4 we outlined 3 different methods for locating the outer Lagrange point, L_2, and found that they provided consistent results. With a reliable way to locate L_2, we tracked SPH particles that moved beyond the radius of L_2 at the time of the CE in-spiral, and of those we counted how many were unbound. We found that higher q binaries have more of their envelope mass beyond L_2 before the start of the CE due to their longer period of pre-CE mass transfer. Of the material pushed beyond L_2, higher q simulations also unbound significantly more, due to the greater velocities with which mass is lost from the system. Resolution is also crucial in examining this early mass loss, as lower resolution simulations have substantially higher amounts of mass lost, as well as mass unbound prior to the CE, unbinding effectively all of the gas that moves past L_2. From this we can conclude that the duration of the pre-CE mass transfer phase is not converged with respect to resolution, and we expect it to be longer in reality than we have shown in this thesis. Additionally, while we know that the longer the pre-CE phase is the smaller the mass transfer is, the total amount of pre-CE mass transfer actually increases. Regarding the effect of mass ratio specifically, with a higher amount of mass lost and unbound from the system, higher q simulations have a weaker CE interaction due to more of the envelope having already been lifted from the system. This may explain why these mass ratios routinely create larger final separations than their lower q counterparts.

We have defined the end of the simulation (and of the CE interaction) to be approximately the point before any resolution-dependent unbinding occurs, something that tends to happen

in all lower resolution simulations. Resolution-dependent unbinding was first described by Reichardt et al. (2019) who showed that when the density surrounding the cores decreases below a threshold, the SPH particles fail to resolve the core and fall down the core's potential acquiring speeds that are then transferred to overlaying layers of loosely bound particles, leading to their unbinding. We cannot comment on anything that happens after this point. Higher resolution simulations may suffer such an unbinding episode also, but would do so later on. In our case, the high resolution simulations were not run long enough to show such "artificial" unbinding.

In Chapter 5 we investigated ways to decrease the separation beyond that achieved at the end of the in-spiral. This was to explain a number of low q observations seen with binary separations of the order of 5 $R_\odot$ (e.g., Iaconi & De Marco, 2019). There we look at the potential for bound material to fall back and re-enter the orbit of the binary and do work on the companion to shrink the separation to ranges smaller than those achieved by the initial CE interaction. For the post-CE distributions of material and their associated angular momentum, we have shown within first order approximation that this mass is very capable of falling far enough back onto the system to cause a secondary interaction. We also calculated the type of fall-back masses expected in different simulations using two different assumptions at the time of the CE's conclusion: all bound mass falls back, or only mass with negative radial velocity falls back (Recall the end of the CE here is before any resolution-dependent unbinding has occurred).

By assuming a range of fallback masses as described above, we show analytically that it is incredibly difficult to do enough work on the orbit to bring the separation down to 5 $R_\odot$, although some in-spiral can be expected. Our analytical approximation seems to fail for fall-back masses approaching the envelope mass, but for now it may be valid in concluding that, if only of the order of $\sim$0.1 $M_\odot$ return then this would not be sufficient to enact sufficient in-spiral to match the observations with the smallest separations. We found that, similar to the findings of Kuruwita et al. (2016), with greater amounts of fall-back mass, more orbital shrinkage is possible. Since our lower q systems generally produce the greatest amount of fall-back mass, and given that these systems already create smaller post-CE final separations, we conclude that the close orbiting observed binaries are best reproduced by lower q systems. This said, the studies of Iaconi & De Marco (2019) showed that there is a group of observed systems with low separations independent of the mass of the companion, as if higher mass

companions were less efficient in unbinding the envelope. Clearly more work is needed in this arena.

We also find that the wider separations of CE binaries are likely those deriving from higher q systems, as the highest final separation created by our simulations is 60 $R_\odot$, 3 times larger than our smallest separation. Our higher resolution $q = 1.00$ simulation has yet to enter a CE, so while at this point we can only speculate as to the long term behaviour of this system, it is also possible that with an exceedingly stable mass transfer phase, this simulation will create a final separation that is larger still. While the separations we have created here are still too small to explain the post-AGB binaries with separations of the order of 100 $R_\odot$, our $q = 1.50$ simulation shows a distinct movement away from the CE in-spiral, confirming that these larger values of q will certainly in-spiral less, and are thus much better candidates to explain the wider binaries.

It is difficult at this time to comment on the formation of circum-binary disks around these systems. We tested the hypothesis that a disk forms from material ejected though L_2 and L_3, which then remains as a kinematically distinct structure through the subsequent CE ejection. However, this hypothesis does not seem to be correct. We cannot comment on whether higher a simulations can form a disk in this way, because we could not follow the interaction further. A further investigation into the two simulations that have yet to experience a CE would be extremely useful regarding the nature and aftermath of whatever interaction the stars share. It is therefore possible that circum-binary disks may only form via fall-back of material if some material does not return to the orbit but remains instead in orbit farther away.

6.2 Future Work

The implication of mass ratios close and above unity on the nature of the binary interactions remain at this time unclear. For binaries with mass ratio well above unity, the current companion is the original primary in the system (the more massive of the two stars at birth). Hence the companion would have to be more evolved, such as a white dwarf or neutron star. We have observed that at low resolution $q = 1.00$ clearly goes through a CE, however, the in-spiral phase is noticeably softer. On the other hand, still at low resolution, $q = 1.50$ has not entered a CE, *and* the separation has even begun plateauing, indicating it is possible that it will not experience a rapid in-spiral phase at all. There is also a growing eccentricity in

the orbit in this case, as is also true of the high resolution $q = 1.00$ simulation, which also has not entered a CE yet. The exact reason for this eccentricity is unclear, and as part of this future work, would be an issue to investigate. The two different behaviours between $q = 1.00$ and $q = 1.50$ when considering the willingness of the system to enter the in-spiral, imply that there might be some intermediate value of q for which the separation decreases to, say, 100 $R_\odot$without the need for a full CE, in which case what kind of interaction would this be? Further to this, we require additional time to run the high resolution $q = 1.00$ simulation, as the long term behaviour is still not completely clear. It is possible this system will enter a CE, and that the early phase of RLOF is simply exceedingly stable and much longer than the simulated time.

Tangentially to this we would also deem the investigation of tabulated EOS' to be critical, as we have already shown early mass transfer can be very sensitive to the EOS. Investigating the MESA EOS for one simulation has already revealed much regarding the increased instability of the mass transfer phase, as well as the larger amounts of unbinding and its reduction of available fall-back mass. We ultimately need to run high resolution simulations with this EOS, as well as differing values of q. While there are still some questions as to the ability of recombination energy to do work in the context of an expanding CE, it is today agreed that recombination energy needs to be taken into account (e.g., Gonzalez-Bolivar et al., 2022).

Finally it is clear that with the presence of resolution-dependent unbinding which sets in at low density near the cores and affects low resolution simulations, we need higher resolution. This leads to long simulation times and the inability to study longer term behaviour, such as fall-back. As such we require a new strategy to investigate the late stage evolution of these systems. It is possible to recreate a similar environment without the need to also simulate the close orbiting binary and the residual relatively high density near the core, that cause the global simulation time-step to be small (individual time-stepping is also possible in PHANTOM, but leads to worse energy conservation). Early testing shows that we can temporarily cut out the central part of the simulation and substitute it with a potential. This reduces the time-step and leads to decreased computation times. This would allow us to probe the post-CE environment numerically.

A

Appendix

Here we provide additional plots for some of our simulations. This is not an exhaustive list of each simulation's associated plots, and features only those serving as comparison to the main simulations.

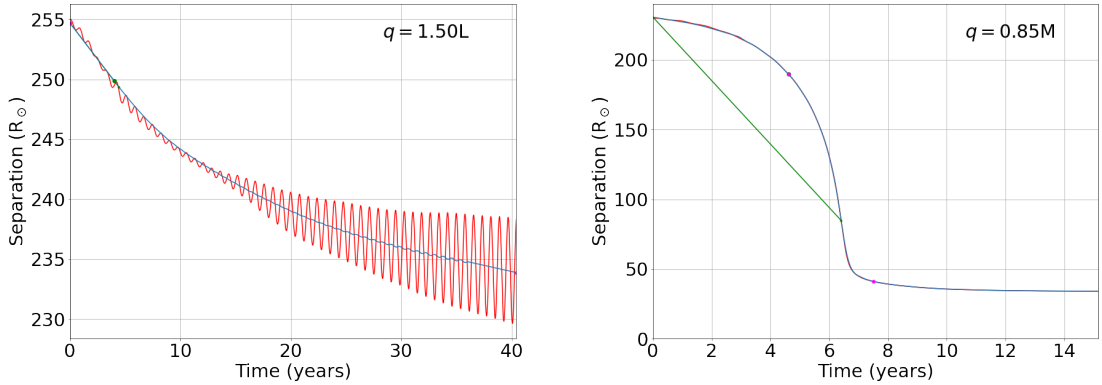

Figure A.1: The evolution of separation for the $q = 1.50$ low resolution simulation, and the MESA EOS $q = 0.85$ simulation. Similarly to the high resolution $q = 1.00$ simulation in Figure 3.1, even at low resolution the highest q simulation here has also not undergone an in-spiral phase. By smoothing the red curve to obtain the blue line, we see that the separation is leveling off with time, and it is possible at such a high q value the system will never become close enough to fully interact in a CE.

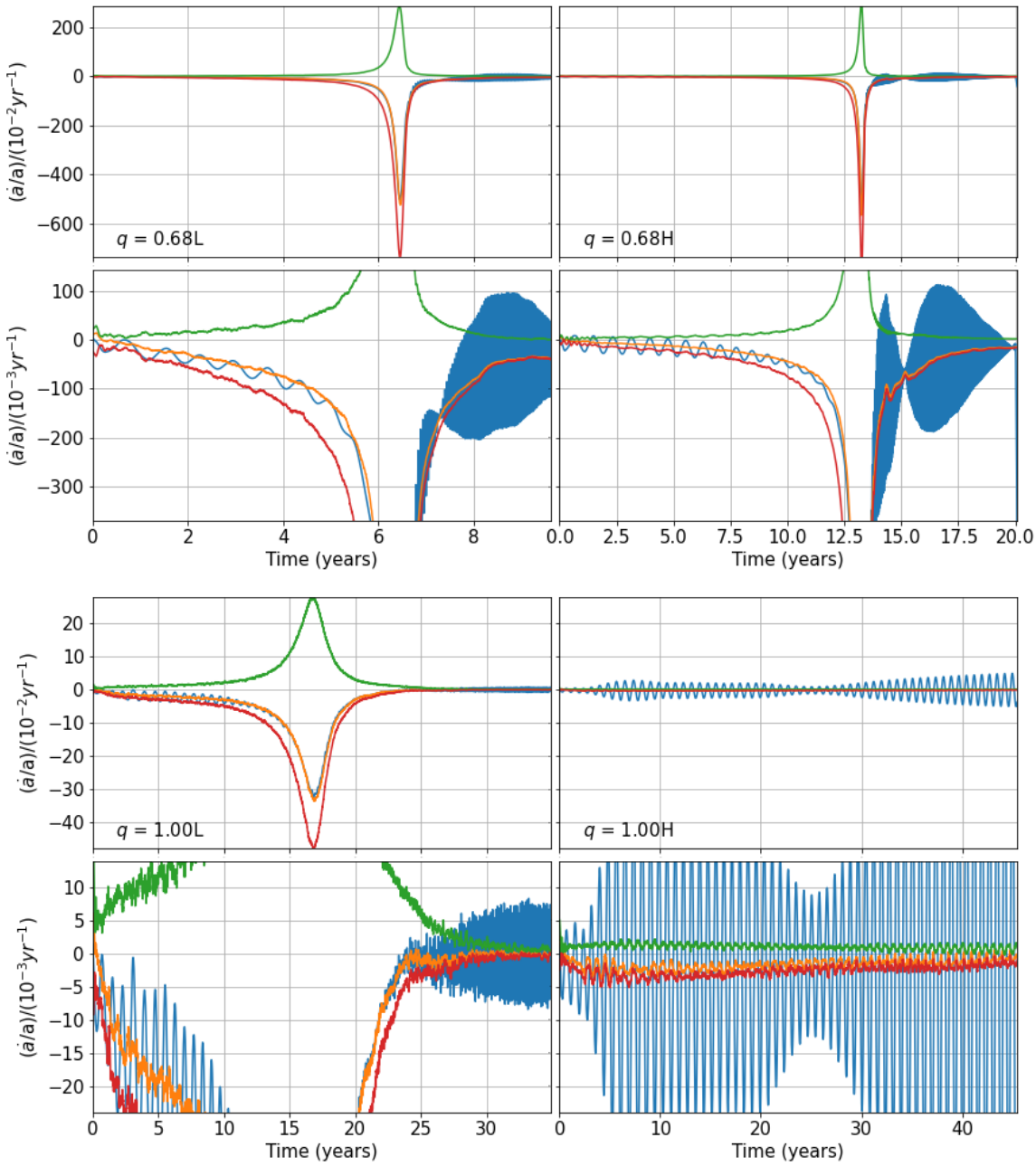

Figure A.2: Similar plots to those of Fig. 3.5, but for the $q = 0.68$ simulation (top) and the $q = 1.00$ simulation (bottom). The top plots here were also previously presented by Reichardt et al. (2019). The behaviour at low resolution is similar across q values for each simulation, however the $q = 1.00$ high resolution simulation again exhibits a much more stable decay of separation. The blue lines indicate orbital eccentricity, which for the high resolution $q = 1.00$ case, is growing, as seen in Figure 3.1.

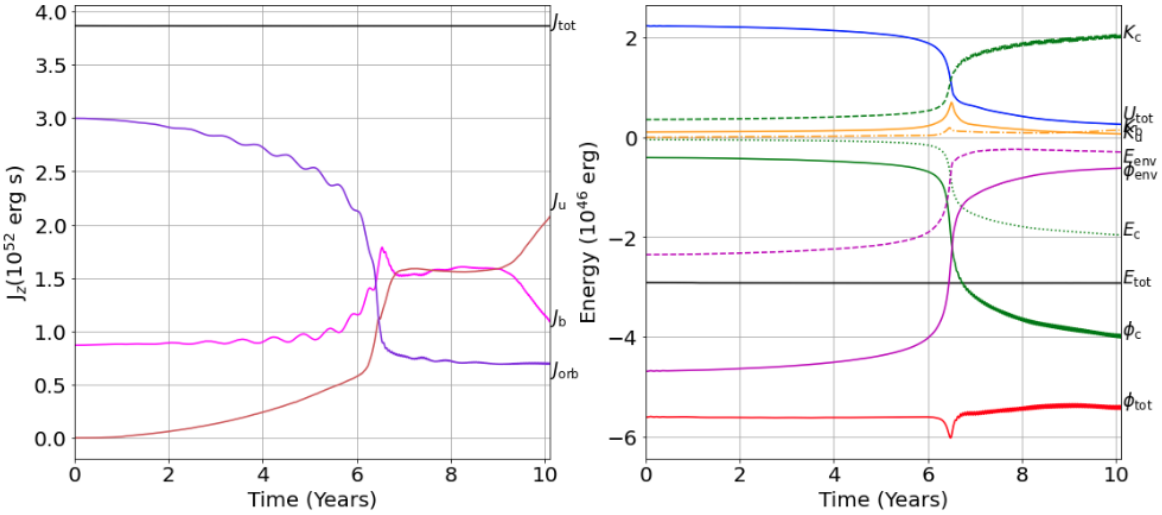

Figure A.3: The counterpart to Figure 3.6 for the $q = 0.68$ high resolution simulation.

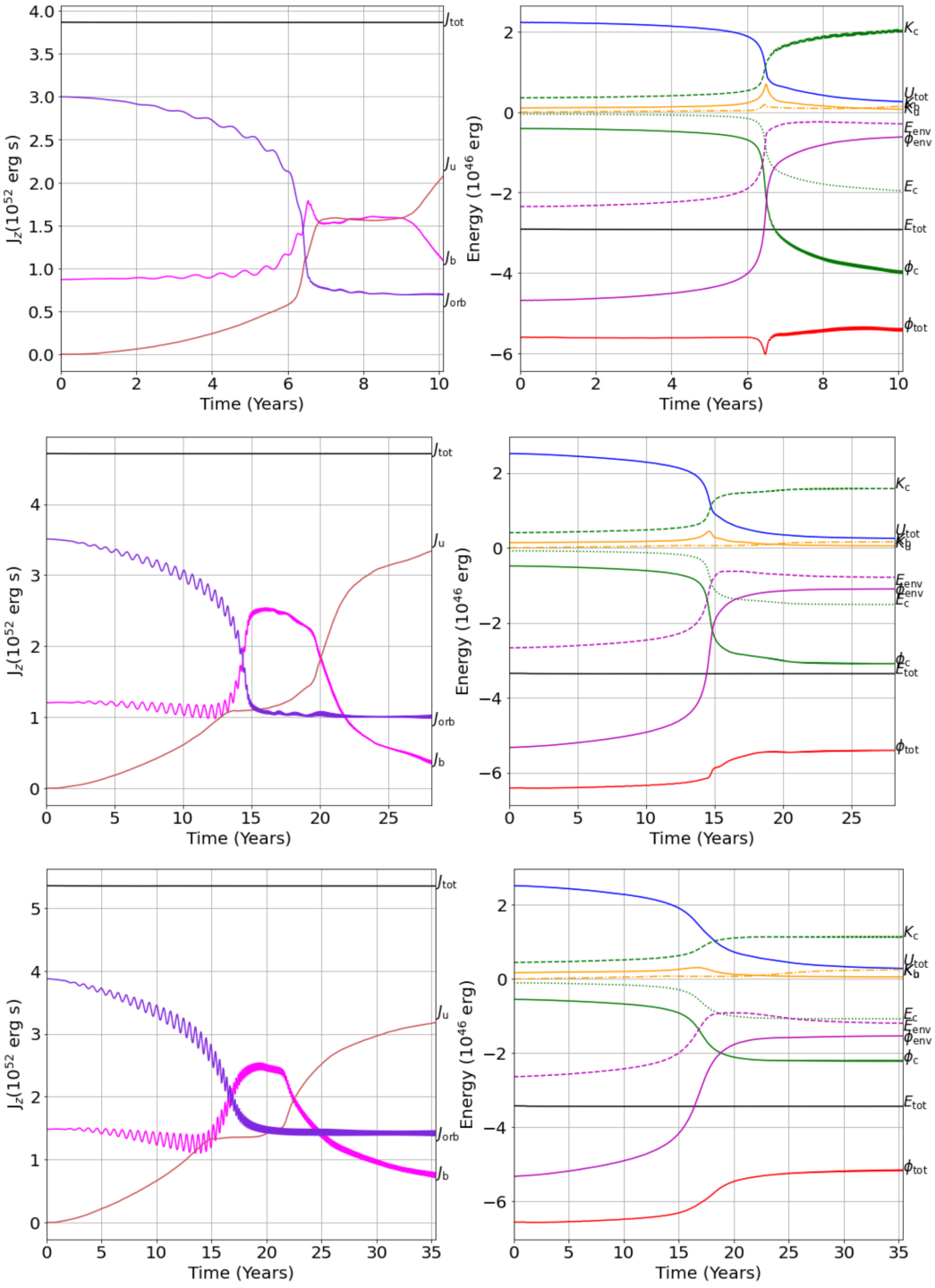

Figure A.4: Here we plot the same as Figures 3.6, and A.3, but for the $q = 0.68, 0.85,$ and 1.00 low resolutions, top to bottom respectively. Notice that the secondary phase of angular momentum unbinding present in the left plots of each. Much like the additional mass unbinding in Figure 4.4, this too is artificial. The calculations used in this thesis consider the point at which after the orbital separation has stabilised, but before this artificial unbinding occurs.

Figure A.5: This QR-code leads to a google drive folder within which are the movies for the evolution of velocity as a function of radius. In these we have included both lower and upper bounds of escape velocity mentioned in Chapter 4. Additionally, we have created movies for each simulation, and not just those mentioned in the thesis text. Note that the high resolution $q = 1.00$, and low resolution $q = 1.50$ simulations do not used the coloured particles to denote L_2 and CE material, as not CE is present. As such the particles are simply left black in these cases. The high resolution $q = 1.00$ simulation's behaviour in these movies is interesting, as it seems to unbind more mass from the beginning almost instantly, but without observing this simulation undergo a CE, it is difficult to say whether or not this is just an exaggerated example of what also occurs in the $q = 0.85$ high resolution simulation.

References

Cossins P. J., 2010, PhD thesis, -

Dan M., Rosswog S., Guillochon J., Ramirez-Ruiz E., 2011, ApJ, 737, 89

Darwin G. H., 1879, Proceedings of the Royal Society of London Series I, 29, 168

De Marco O., Passy J.-C., Moe M., Herwig F., Mac Low M.-M., Paxton B., 2011, MNRAS, 411, 2277

Deacon N. R., Kraus A. L., 2020, MNRAS, 496, 5176

Duchêne G., Kraus A., 2013, ARA&A, 51, 269

Eggleton P. P., 1983, ApJ, 268, 368

Frank J., King A., Raine D. J., 2002, Accretion Power in Astrophysics: Third Edition

Gonzalez-Bolivar M., De Marco O., Lau M. Y. M., Hirai R., Price D. J., 2022, arXiv e-prints, p. arXiv:2205.09749

Han Z., Podsiadlowski P., 2004, MNRAS, 350, 1301

Hjellming M. S., Webbink R. F., 1987, ApJ, 318, 794

Hut P., 1980, A&A, 92, 167

Iaconi R., De Marco O., 2019, MNRAS, 490, 2550

Iaconi R., Reichardt T., Staff J., De Marco O., Passy J.-C., Price D., Wurster J., Herwig F., 2017a, MNRAS, 464, 4028

Iaconi R., Reichardt T., Staff J., De Marco O., Passy J.-C., Price D., Wurster J., Herwig F., 2017b, MNRAS, 464, 4028

Iaconi R., De Marco O., Passy J.-C., Staff J., 2018, MNRAS, 477, 2349

Iben Icko J., Livio M., 1993, PASP, 105, 1373

Ivanova N., Nandez J. L. A., 2016, MNRAS, 462, 362

Ivanova N., et al., 2013, A&ARv, 21, 59

Kuruwita R. L., Staff J., De Marco O., 2016, MNRAS, 461, 486

Lattanzio J. C., Monaghan J. J., Pongracic H., Schwarz M. P., 1986, SIAM Journal on Scientific and Statistical Computing, 7, 591

Lau M. Y. M., Hirai R., González-Bolívar M., Price D. J., De Marco O., Mandel I., 2022, MNRAS, 512, 5462

Leahy D., Leahy J., 2015, Computational Astrophysics and Cosmology, 2

MacLeod M., Loeb A., 2020, ApJ, 893, 106

MacLeod M., Macias P., Ramirez-Ruiz E., Grindlay J., Batta A., Montes G., 2017, ApJ, 835, 282

MacLeod M., Ostriker E. C., Stone J. M., 2018a, ApJ, 863, 5

MacLeod M., Ostriker E. C., Stone J. M., 2018b, ApJ, 868, 136

Meyer F., Meyer-Hofmeister E., 1979, A&A, 78, 167

Misra D., Fragos T., Tauris T. M., Zapartas E., Aguilera-Dena D. R., 2020, A&A, 642, A174

Nandez J. L. A., Ivanova N., 2016, MNRAS, 460, 3992

Oomen G.-M., Van Winckel H., Pols O., Nelemans G., Escorza A., Manick R., Kamath D., Waelkens C., 2018, A&A, 620, A85

Ostriker E. C., 1999, ApJ, 513, 252

Paczynski B., 1976, in Eggleton P., Mitton S., Whelan J., eds, Vol. 73, Structure and Evolution of Close Binary Systems. p. 75

Paczyński B., Sienkiewicz R., 1972, Acta Astron., 22, 73

Passy J.-C., et al., 2012, ApJ, 744, 52

Pejcha O., Metzger B. D., Tomida K., 2016, MNRAS, 461, 2527

Price D. J., 2007, Publ. Astron. Soc. Australia, 24, 159

Price D. J., 2012a, Journal of Computational Physics, 231, 759

Price D. J., 2012b, in Capuzzo-Dolcetta R., Limongi M., Tornambè A., eds, Astronomical Society of the Pacific Conference Series Vol. 453, Advances in Computational Astrophysics: Methods, Tools, and Outcome. p. 249 (arXiv:1111.1259)

Price D. J., et al., 2018, Publ. Astron. Soc. Australia, 35, e031

Reichardt T. A., De Marco O., Iaconi R., Tout C. A., Price D. J., 2019, MNRAS, 484, 631

Reichardt T. A., De Marco O., Iaconi R., Chamandy L., Price D. J., 2020, MNRAS, 494, 5333

Schmidt B. P., High-Z Sn Search Team 1998, in Paul J., Montmerle T., Aubourg E., eds, 19th Texas Symposium on Relativistic Astrophysics and Cosmology. p. 145

Schwarz R., Bazsó Á., Érdi B., Funk B., 2012, MNRAS, 427, 397

Springel V., 2010, MNRAS, 401, 791

Tocknell J., De Marco O., Wardle M., 2014, MNRAS, 439, 2014

Tout C. A., Hall D. S., 1991, MNRAS, 253, 9

Tylenda R., Kamiński T., Schmidt M., Kurtev R., Tomov T., 2011, A&A, 532, A138

Webbink R. F., 1984, ApJ, 277, 355

van Winckel H., 2003, in Corradi R. L. M., Mikolajewska J., Mahoney T. J., eds, Astronomical Society of the Pacific Conference Series Vol. 303, Symbiotic Stars Probing Stellar Evolution. p. 294

van Winckel H., et al., 2009, A&A, 505, 1221